

CHAPTER 6

SCRAPE-OFF LAYER TRANSPORT ON JET

W. FUNDAMENSKI* *Euratom/UKAEA Fusion Association
Culham Science Centre, Abingdon OX14 3DB, United Kingdom*

Received June 25, 2007

Accepted for Publication October 5, 2007

The tokamak plasma boundary, which is typically identified with the area of open field lines known as the scrape-off layer (SOL), determines the degree of plasma-wall interaction. SOL physics, much of which is concerned with the exhaust (removal) of particles and energy from the plasma, has been one of the major topics investigated on JET during the past two decades. In this chapter, SOL transport/exhaust studies on JET are reviewed. The discussion proceeds chronologically, beginning with the limiter SOL and treating in turn the successive divertors (Mk0, MkI, MkIIA, and MkIIGB) with which JET was equipped in subsequent years. When appropriate, old results are reinterpreted in the light of recent improvements in our understanding of edge/SOL turbulence and edge-localized modes (ELMs). Although

emphasis is placed on deuterium transport in the SOL, impurity transport is briefly considered. In particular, the effect of divertor closure, of L-mode versus H-mode, and of inter-ELM versus ELM erosion on plasma purity (Z_{eff}), radiation (f_{rad}), and confinement (τ_E) is briefly discussed. The chapter concludes with a summary of empirical scaling expressions for SOL profile widths (radial e-folding lengths) in both limiter and divertor configurations.

KEYWORDS: *scrape-off layer, edge plasma, plasma-surface interaction*

Note: Some figures in this paper are in color only in the electronic version.

Contents—Chapter 6

- I. INTRODUCTION
- II. BASIC CONCEPTS OF SOL PHYSICS
 - II.A. Perpendicular (Radial) Transport
 - II.B. Diamagnetic Transport
 - II.C. Parallel Transport
 - II.D. Plasma Turbulence in the SOL
 - II.E. Effects of the H-Mode and ELMs on the SOL
- III. LIMITER SOL
 - III.A. Carbon Limiters
 - III.A.1. Ohmically Heated Discharges
 - III.A.2. NBI-Heated Discharges
 - III.A.3. ICRH Discharges
 - III.B. Beryllium Limiters
 - III.C. SOL Turbulence and the H-Mode in Limiter Plasmas
- IV. DIVERTOR SOL
 - IV.A. Mk0 (1986 to 1992)
 - IV.B. MkI (1994 to 1995)
 - IV.C. MkIIA (1996 to 1998)
 - IV.D. MkIIGB (1994 to 2004)
 - IV.E. Effect of Divertor SOL on Plasma Purity, Radiation, and Confinement: MkI to MkIIGB
- V. CONCLUSIONS
- REFERENCES

*E-mail: wojtek.fundamenski@jet.uk

I. INTRODUCTION

In confined plasmas, the term *scrape-off layer* (SOL) refers to the region of open field lines between the last closed flux surface (LCFS), or the magnetic separatrix (sep), and the vessel wall. It was famously labeled as the domain of kitchen physics,¹ in which the interaction of ions and electrons with molecules, atoms, sheaths, and solid surfaces can dominate the overall plasma behavior. For many fusion *physicists*, accustomed to a fully ionized, collisionless, hydrogenic plasma occupying a succession of nested toroidal flux surfaces and obeying the single-fluid ideal-magnetohydrodynamic (MHD) equations, the SOL, where the stellar world of hot plasmas meets the earthly world of cold solids, i.e., the real world of our everyday experience, represents novel and often unfamiliar territory. For the same reasons, the SOL is of particular interest to the fusion *engineer*, whose primary interest lies in the design and exploitation of a fusion reactor, and who struggles with such problems as

1. the exhaust of fusion power without undue damage to the vessel walls

2. the removal of fusion ash (helium) and other impurities from the core plasma
3. recovery of fusion fuel and prevention of tritium retention (codeposition) in plasma-facing components
4. control of material erosion and migration within the vacuum vessel.

These issues are clearly of critical importance for the planned ITER experiment.

Throughout its long history, JET has made pivotal contributions to the understanding of SOL physics and has provided invaluable information to tackle the stated fusion technology issues.¹⁻¹⁶⁰ In what follows, these contributions will be briefly reviewed, focusing on those with highest importance to ITER. After a modern introduction to the basic concepts of SOL transport theory, which are introduced principally using JET results, in Sec. II, JET SOL transport studies in limiter and divertor configurations are examined in Secs. III and IV, respectively; the latter is divided into two subsections, dealing separately with ohmic and L-mode, and ELMy H-mode SOLs, which are further divided into subsections dealing with carbon and beryllium limiters; ohmic, neutral beam injection (NBI), and ion cyclotron resonance heating (ICRH); and successive divertors (Mk0, MkI, MkIIA, and MkIIGB) operating on JET. The chapter concludes with a brief summary of the empirical scaling expressions for SOL profile widths.

II. BASIC CONCEPTS OF SOL PHYSICS

As the name suggests, the last closed flux surface represents the transition between the region of closed and open magnetic field lines. This surface can be created either by inserting a solid object, known as the limiter, into the plasma,^a or by shaping the poloidal magnetic field with external current-carrying coils to create a poloidal field null, or *X* point, and a magnetic separatrix, and thus to divert the SOL plasma into a specifically designed structure, known as the divertor.^b The two methods, shown for JET in Fig. 1 (also see Figs. 1 and 18 in Ref. 2) produce distinct SOL geometries: the limiter SOL generally resembles the closed flux surfaces, whereas the divertor SOL expands poloidally in the vicinity of the *X* point, such that its footprint on the solid targets is typically a factor of 3 to 5 times broader than its width at the outer midplane. This broadening, commonly referred to as poloidal flux expansion, is illustrated in Fig. 1 for

^aHistorically, this is the earlier technique. There are four types of limiters: poloidal, toroidal (belt), vertical (rail), and discrete (mushroom).

^bThis is a comparatively recent innovation; there are two types of divertors, toroidal and poloidal, with the latter being by far the most common.

three JET divertor designs, MkI, MkIIA, and MkIIGB (gas box). Another consequence of the poloidal field null is the near-linear decrease of the field line angle between the field line and divertor target, θ_{\perp} , in the vicinity of the *X* point and the associated increase in the radial gradient of the safety factor q , i.e., of the magnetic shear $s = rdq/dr$. Assuming that upstream profiles of thermodynamic variables decay exponentially with radius, one finds that as the distance between the *X* point and the target is gradually reduced, the particle and heat fluxes normal to the tile surface are reduced at the strike point location and tend to peak away from the LCFS, as shown in Fig. 2.

Aside from poloidal flux expansion, the main difference between the limiter and divertor SOLs lies in the distribution of particle (plasma) sources. The limiter method leads to a relatively simple SOL (fueled by radial particle transport from the core region), whereas the divertor method, in which the SOL is generally more complex, both geometrically and physically, is dominated by plasma recycling in the divertor volume. In both cases, the source of energy can be firmly located inside the LCFS, where it is deposited by plasma heating or generated by fusion reactions. Some of this thermal energy may be radiated in the edge plasma, including the SOL, with the remainder conveyed by parallel transport to the limiter or divertor tiles, where it is removed, e.g., by heat exchange with an active cooling loop. The sources and sinks of energy are thus well separated, with the SOL acting as the medium for energy flow and power exhaust. In contrast, the sources and sinks of particles in the SOL cannot be easily separated due to the recombination of ions and electrons at the limiter/divertor tiles. The recombined plasma species leave the surface as molecules, dissociate into atoms, and then ionize at some distance from the solid surface. This distance, known as the neutral transport mean-free-path, λ_0 , is determined by the relative strength of the ion-neutral charge-exchange and atomic ionization processes⁵:

$$\lambda_0 = (\sigma_0 n_e)^{-1}$$

and

$$\sigma_0^2 = \frac{\langle \sigma_{iz} v \rangle (\langle \sigma_{iz} v \rangle + \langle \sigma_{CX} v \rangle)}{T_i / m_i}, \quad (1)$$

where σ_0 is the average neutral transport cross section.

In the limiter SOL, most of the neutrals penetrate the LCFS, ionize in the edge plasma, and distribute (as ions) roughly uniformly on each closed flux surface. They return to the SOL via an ambipolar (charge-conserving) radial plasma advection/diffusion^c driven

^c*Advection* refers to transport of mass due to fluid flow, whereas *diffusion* refers to transport of mass due to interparticle collisions. The related terms for transport of heat are *convection* and *conduction*.

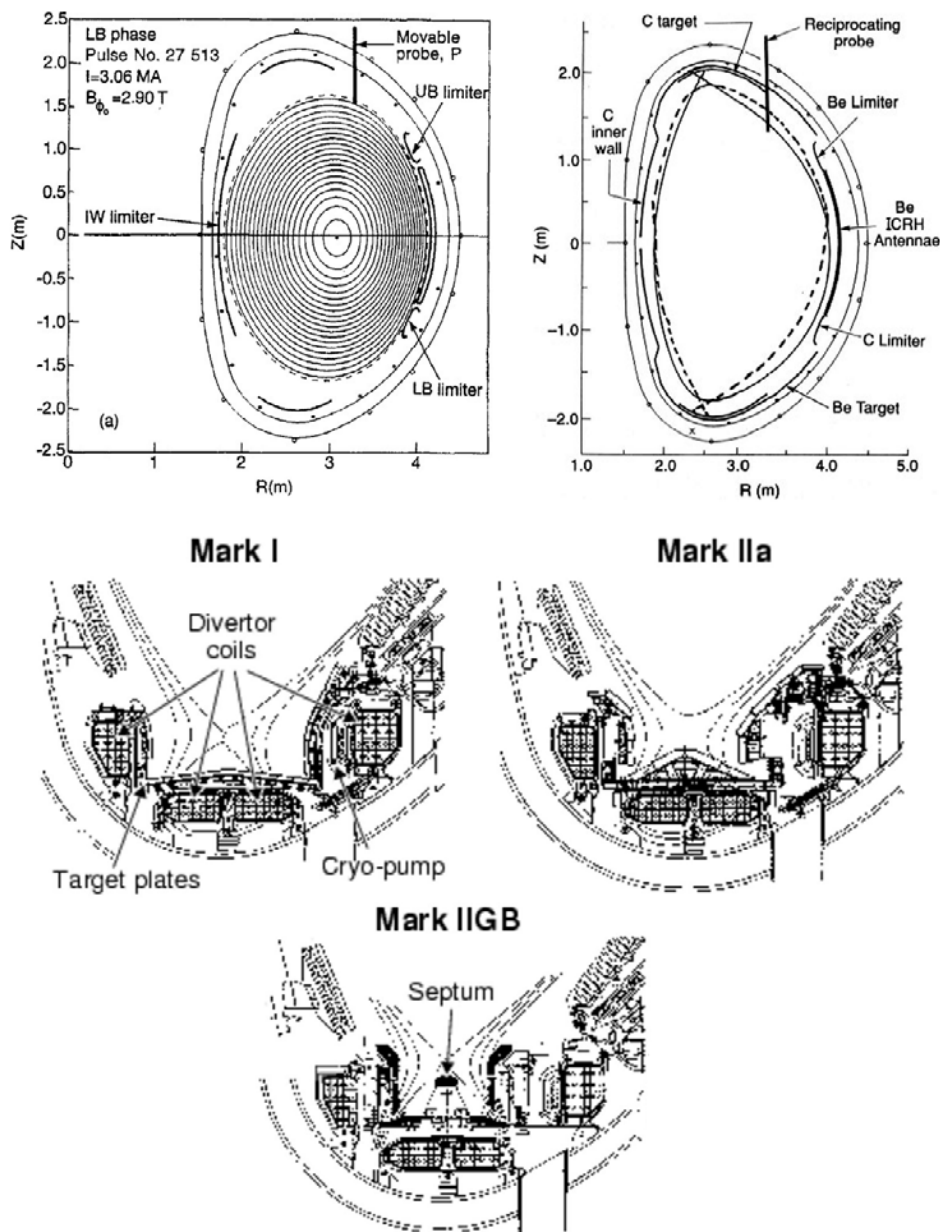


Fig. 1. MHD equilibria for JET limiter (top left) and various divertor configurations: Mk0 (top right), MkI (middle left), MkIIA (middle right), and MkIIGB (bottom). In limiter equilibria, the LCFS is formed on either the lower or upper toroidal (belt) limiters or, occasionally, on the inner wall. The earliest (Mk0) divertor configuration involved forming the X point in the vicinity of the upper or lower dump plates, shown in the middle left frame, and using these as divertor targets. The three subsequent divertors represent increasing geometrical closure: Mk0 \rightarrow MkI \rightarrow MkIIA \rightarrow MkIIGB. Reproduced with permission from Refs. 3, 57, and 58.

by thermodynamic and magnetic gradients and flow toward the limiter tiles along the magnetic field lines; the resulting flow increases linearly from the stagnation point located roughly halfway between the bounding limiter plates to sonic or supersonic velocities in front of the limiters as required by the Bohm criterion (see Sec. II.C). The closed cycle, involving a recirculation of plasma

species and their recombination at some plasma-solid interface, is commonly known as plasma recycling.^d

^dIt is worth noting that the limiter SOL, because of its proximity to the LCFS and the associated high electron temperature and low electron collisionality, $\nu_e^* < 10$, is normally found in the sheath-limited regime (see Sec. II.C).

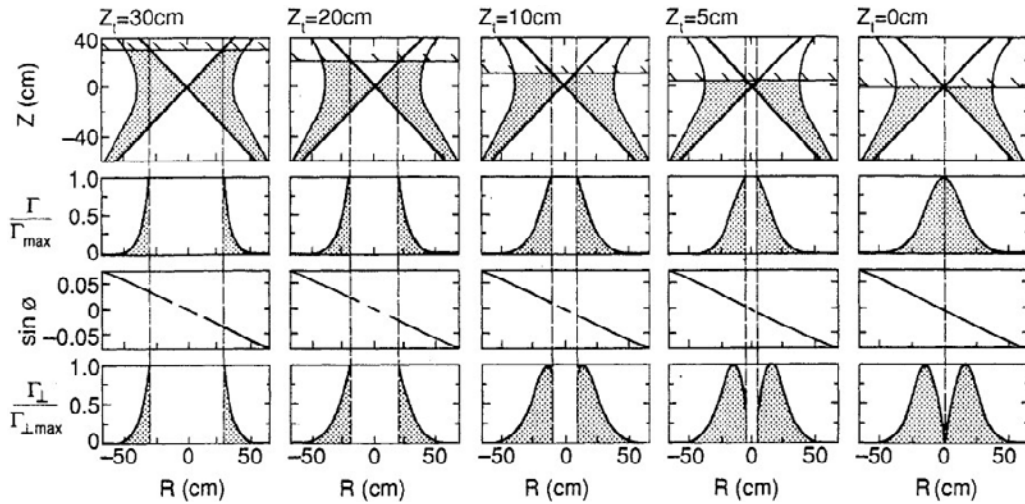


Fig. 2. A scan in the distance between the X point and the divertor target (top), typical of the horizontal target configurations such as those used in Mk0, MkI, and MkIIA divertors, showing the resulting plasma flux profiles, both along the field lines (second from top) and normal to the divertor target (bottom); the angle between the field line and divertor target scales linearly with the X-point distance to the target (second from bottom). Reproduced with permission from Ref. 4.

In the divertor configuration, where the poloidal distance between the divertor tiles and the X point is typically larger than λ_0 , plasma recycling is localized to the divertor volume and, as a result, influences the plasma flow only in the vicinity of the divertor tiles (the recycling region). As the upstream density n_u increases, the large particle source in the divertor augments the parallel plasma flow to the targets, Γ_t , an effect known as flow amplification; this flow increases as the square of the upstream density, $\Gamma_t \propto n_u^2$, whereas the target density increases as its cube, $n_t \propto n_u^3$.^e In the recycling region, the strong convective flow of energy reduces the parallel temperature gradients, whereas line radiation associated with excitation of neutral hydrogen effectively cools the divertor plasma, Fig. 3. At sufficiently low temperatures (typically below 5 eV), the loss of parallel plasma momentum due to charge exchange with background neutrals reduces the plasma flux to the divertor tiles, even as the upstream density is increased, an effect known as plasma flux rollover, as seen in the example from JET, Fig. 4. It corresponds to plasma detachment from the divertor plates and the detached regime of SOL transport, $\Gamma_t \propto n_u^{-\alpha}$ and $n_t \propto n_u^{-\beta}$, where $\alpha, \beta > 0$ (see Sec. II.C). At still lower temperatures (typically below 1 eV) and sufficiently high densities, plasma detachment is further enhanced by volumetric recombination, which can extinguish the plasma flame entirely, preventing any plasma-surface contact.

The effectiveness with which the divertor structure traps neutral particles, an essential requirement for ef-

fective pumping of both hydrogenic and impurity species, is quantified in terms of the fraction of neutrals that ionize outside the divertor volume and is commonly referred to as divertor closure.^f Thus, divertor closure is a complicated function of both divertor target geometry, magnetic geometry, and divertor plasma parameters. However, it can be roughly approximated as the geometrical closure, i.e., the angle subtended by the separatrix and the divertor targets, with the strike point as the pivot location. For more than a decade, JET has operated with three divertors of increasing closure: Mk0 \rightarrow MkI \rightarrow MkIIA \rightarrow MkIIGB (Fig. 1). Not surprisingly, sub-divertor neutral pressures and neutral compression (ratio of divertor to main chamber pressures) increase with divertor closure (Fig. 5). As the divertor plasma detaches, the ionization front moves away from the target, effectively reducing the closure of the divertor structure and thus degrading its ability to trap neutral particles. This effect is manifest in the rollover of neutral compression in a density scan, as seen in Fig. 5.

Despite the toroidal symmetry^g inherent in the tokamak concept and its primary consequence, namely, the existence of nested toroidal flux surfaces, one should not lose sight of the three-dimensional nature of magnetized plasma transport. This is particularly true in the region of

^fA closed divertor traps a larger fraction of neutrals than an open divertor.

^gWe forget for the moment about the toroidal field asymmetry due to a finite number of coils, localized heating by rf antennas and neutral beams, localized cooling by gas and pellets injection, and localized recycling from poloidal limiters and other nonuniformities in the vessel wall.

^eThat is, SOL transport follows the conduction-limited regime (see Sec. II.C).

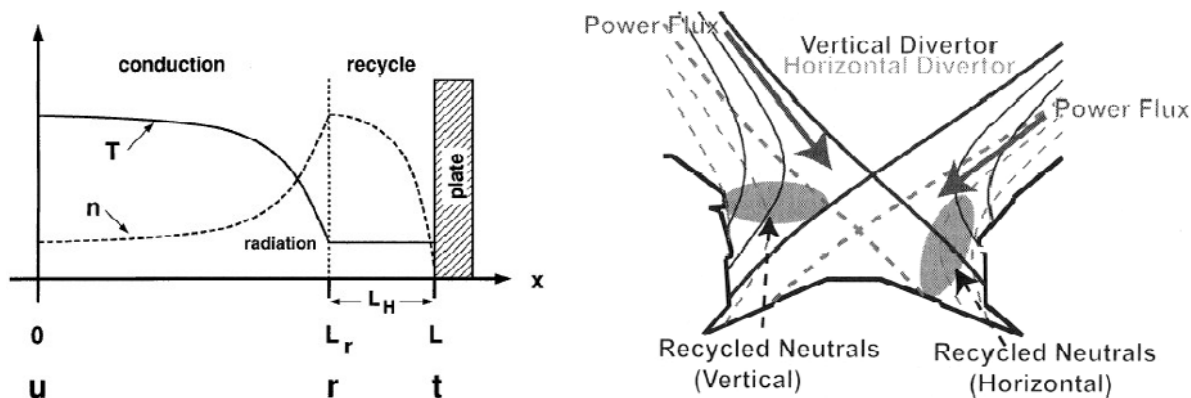


Fig. 3. Left: Schematic representation of density n and temperature T profiles along the SOL magnetic field lines x , illustrating both the conduction and convection (recycling) dominated regions; here u denotes the upstream location halfway between two solid targets, t denotes the target, and r the beginning of the recycling region, $L - L_r \approx \lambda_0$, where λ_0 is the neutral transport mean-free-path (note that this region has been greatly expanded for the sake of clarity). Right: Schematic representation of the recycling pattern in the MkIIA divertor, comparing the effect of operating with strike points on the vertical targets (solid lines) and horizontal targets (dashed lines). In both cases, the average velocity of the recycled neutrals is normal to the solid surface, but in the former case they enter, they travel toward the near-SOL, and in the latter case toward the far-SOL regions. The first case is favorable, since it increases divertor closure and cools the hot, near-SOL plasma; the second is unfavorable, since it allows neutrals to escape and thus fuel the upstream SOL region. In addition, the ionization cloud is more radially extended with a horizontal target, resulting in a broader upstream density profile. Reproduced with permission from Refs. 3 and 6.

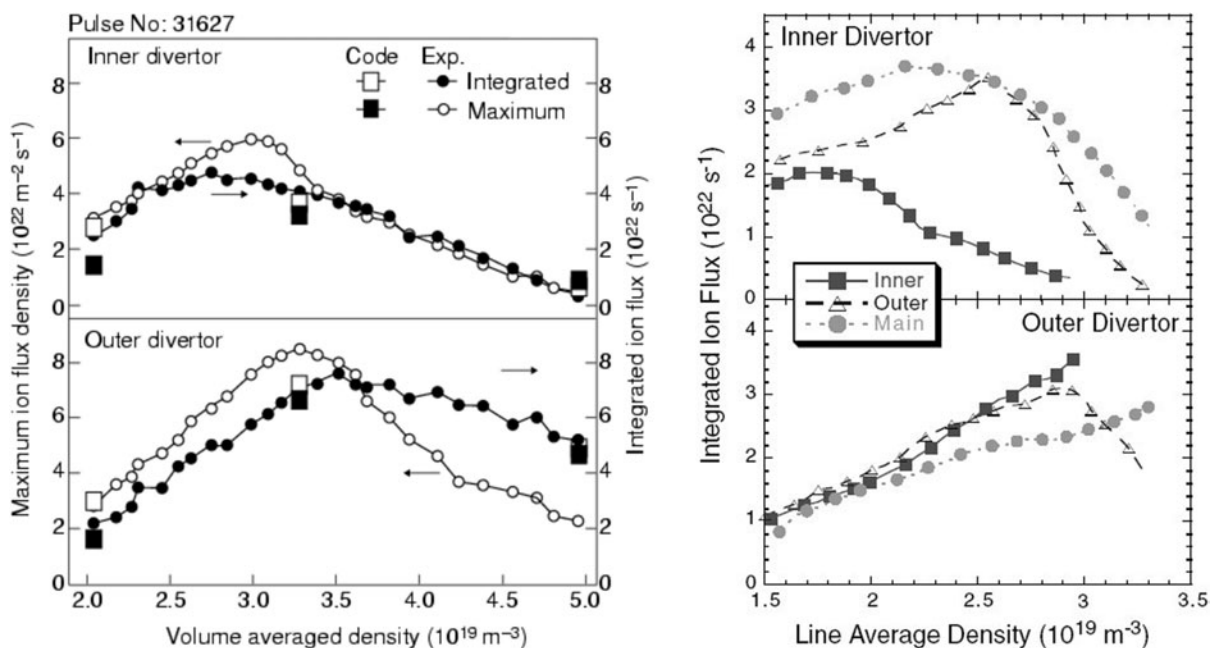


Fig. 4. Illustration of rollover in ion fluxes to JET divertor inner and outer targets during a density ramp, indicating divertor plasma detachment: MkI ohmic discharge (left) and MkIIGB L-mode discharge (right). The MkI case shows both integrated and peak ions fluxes, as well as EDGE2D/NIMBUS modeling predictions, which are in fair agreement with the observed trends. The MkIIGB case compares the results of three gas puffing locations (inner divertor, outer divertor, and main chamber), showing that localized gas puffing assists in plasma detachment. Reproduced with permission from Refs. 3 and 7.

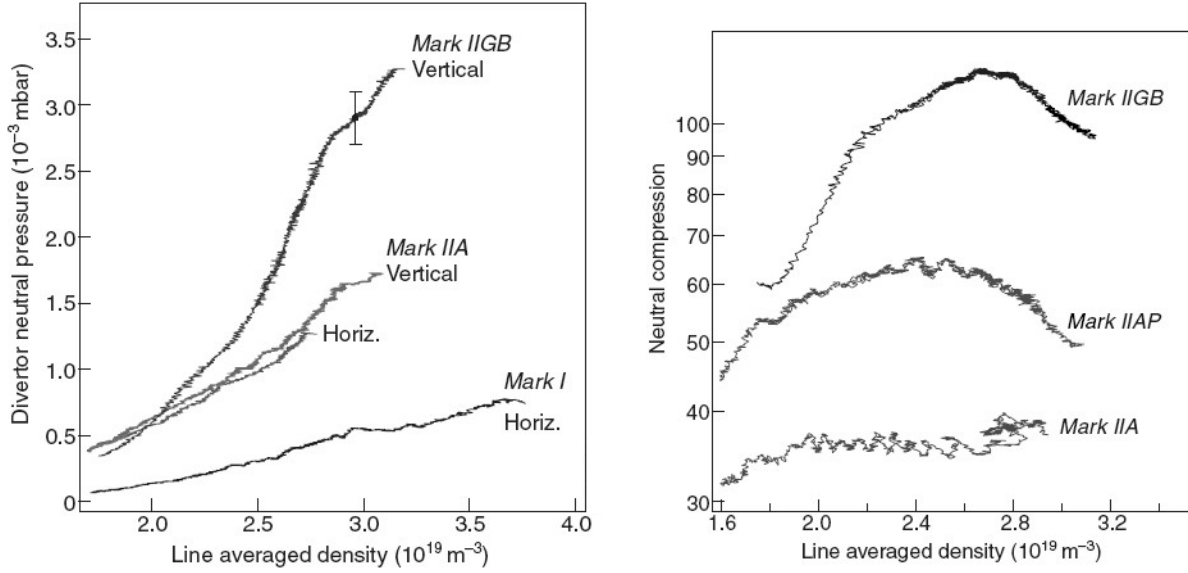


Fig. 5. Neutral pressure at the divertor cryopump for similar JET L-mode discharges in different divertor geometries is found to increase with both the line-average (core plasma) density and divertor closure, MkI \rightarrow MkIIA \rightarrow MkIIGB (left); note that changing the strike point location from horizontal to vertical targets in the MkIIA divertor does not affect the neutral pressure but increases the density limit by $\sim 10\%$. Neutral compression (ratio of divertor to main chamber pressures) increases with divertor closure (right). The rollover in neutral compression indicates divertor plasma detachment, which degrades neutral trapping in the divertor volume, i.e., the effective closure. Reproduced with permission from Ref. 3.

open magnetic field lines that define the SOL. In the following sections we consider the properties of plasma transport in the three magnetic directions: parallel to the magnetic field, denoted by the symbol \parallel ; normal to the magnetic field and yet confined to the magnetic flux surface, known as the diamagnetic direction and denoted by the symbol \wedge ; and normal to the magnetic flux surface, known variously as the radial or perpendicular direction and denoted by the symbol \perp .

II.A. Perpendicular (Radial) Transport

Classical, collisional transport theory predicts that in a confined plasma, the projections of heat flux density of species a , denoted by q_a , in these directions must be ordered as follows:

$$q_{\parallel a} : q_{\wedge a} : q_{\perp a} \approx 1 : \Delta_a : \Delta_a^2, \quad \Delta_a = (\omega_{ca} \tau_a)^{-1}, \quad (2)$$

where $\omega_{ca} = e_a B / m_a$ is the gyrofrequency and τ_a is the collisional time of species a ; flux densities of particles, Γ_a , are ordered similar to electron heat flow q_e . Since $\omega_{ca} \gg \tau_a^{-1}$ ($\Delta_a \ll 1$) is one of the conditions that define a magnetized plasma, the other being $\delta_a \equiv \rho_a / L_{\perp} \ll 1$, where ρ_a is the gyroradius and L_{\perp} is the transverse gradient scale length of the electromagnetic fields, one generally finds a strong scale separation in the magnitudes of the parallel, diamagnetic, and radial fluxes, with $\Gamma_{\parallel} \gg$

$\Gamma_{\wedge} \gg \Gamma_{\perp}$. This fact underlies the thin, elongated, boundary layer aspect of the SOL, whose radial extent is determined by competition between parallel and radial fluxes. Neglecting volumetric sources, the radial e-folding lengths of the parallel particle flux density Γ_{\parallel} and the parallel heat flux density $q_{\parallel a}$, which are defined as $\lambda_{\Gamma} \equiv \Gamma_{\parallel} / \nabla_{\perp} \Gamma_{\parallel}$ and $\lambda_{q_a} \equiv q_{\parallel a} / \nabla_{\perp} q_{\parallel a}$, may be estimated as

$$\nabla \cdot \Gamma \approx 0 \Rightarrow \frac{\lambda_{\Gamma}}{L_{\parallel}} \sim \frac{\Gamma_{\perp}}{\Gamma_{\parallel}} \sim \Delta_e^2 \ll 1 \quad (3)$$

and

$$\nabla \cdot \mathbf{q}_a \approx 0 \Rightarrow \frac{\lambda_{q_a}}{L_{\parallel}} \sim \frac{q_{\perp a}}{q_{\parallel a}} \sim \Delta_a^2 \ll 1, \quad (4)$$

where L_{\parallel} is half the magnetic connection length between the divertor or limiter targets. The corresponding lengths for particle density, $\lambda_n \equiv n / \nabla_{\perp} n$, temperature, $\lambda_{T_a} \equiv T_a / \nabla_{\perp} T_a$, and pressure, $\lambda_{p_a} \equiv p_a / \nabla_{\perp} p_a$, are related to λ_{Γ} and λ_{q_a} as follows:

$$\lambda_{\Gamma}^{-1} = \lambda_n^{-1} + (2\lambda_T)^{-1}$$

and

$$\lambda_{q_a}^{-1} = \lambda_{\Gamma}^{-1} + \lambda_T^{-1} = \lambda_n^{-1} + 1.5\lambda_T^{-1}, \quad (5)$$

and $\lambda_{pa}^{-1} = \lambda_n^{-1} + \lambda_a^{-1}$. The estimates of Eqs. (3) and (4) are highly idealized, since unlike parallel and diamagnetic fluxes, which are typically well understood, radial fluxes in the SOL are governed by turbulent advection and can exceed the classical values by two to three orders of magnitude; we return to this point in Sec. II.D. As a result, the SOL is generally much broader than predicted by Eqs. (3) and (4), with typical values of $\lambda_n \sim \lambda_{Te} \sim \lambda_{pe} \sim 0.01r_0$, where r_0 is the minor radius of the torus.

It is conventional to divide the SOL into two radial regions: the near SOL, defined as the region of high plasma potential, $\varphi \approx 3T_{e,LCFS}$, strong radial electric fields, $E_\perp \approx \nabla_\perp \varphi \approx 3T_{e,LCFS}/\lambda_{Te,LCFS}$, and poloidal flow shear, $\nabla_\perp v_E \approx (E_\perp/B\lambda_{Te,LCFS})$, which extends $\sim \lambda_{Te,LCFS}$ beyond the LCFS, and the far SOL, which refers to the remaining region of the SOL extending toward the vessel wall. The near SOL is of particular importance to power deposition on divertor/limiter tiles, whereas the far SOL determines the degree of plasma interaction with the main chamber wall.

If the radial turbulent fluxes of particles and heat are expressed in terms of effective radial velocities, $v_{\perp n} = \Gamma_\perp/n$ and $v_{\perp T} = q_\perp/\frac{5}{2}nT$, or diffusivities, $D_\perp = \Gamma_\perp/\nabla n$ and $\chi_\perp = q_\perp/n\nabla T$, these may be inferred from the measured e-folding lengths as follows:

$$\begin{aligned}\lambda_\Gamma &\approx v_{\perp n} \tau_{\parallel n} , \\ \lambda_n \lambda_\Gamma &\approx D_\perp \tau_{\parallel n} , \\ \tau_{\parallel n} &\approx \frac{L_\parallel}{c_s}\end{aligned}\quad (6)$$

and

$$\begin{aligned}\lambda_q &\approx v_{\perp T} \tau_{\parallel T} , \\ \lambda_T \lambda_q &\approx \chi_\perp \tau_{\parallel T} , \\ \tau_{\parallel T} &\approx \frac{L_\parallel^2}{\chi_{\parallel e}} ,\end{aligned}\quad (7)$$

where $c_s = [(T_e + T_i)/m_i]^{1/2}$ is the plasma sound speed and $\chi_{\parallel e}$ is the parallel electron heat diffusivity, which is larger than the ion diffusivity by the square root of the mass ratio, hence $\chi_{\parallel e} \gg \chi_{\parallel i}$.^h On JET, under typical ohmic and L-mode conditions, the effective velocities and diffusivities are found in the range ~ 10 to 100 m/s and ~ 0.1 to 1 m²/s, respectively.

Simple models of the SOL suggest that all the above radial e-folding lengths are linearly proportional, $\lambda_n \sim$

^hNote that Eq. (7) presupposes the conduction-limited regime, $10 < \nu_e^* < 100$ (see Sec. II.C), i.e., that parallel energy transport is dominated by electron conduction; in the sheath-limited regime, $\nu_e^* < 10$, parallel convection dominates, and $\tau_{\parallel T} \approx \tau_{\parallel n}$.

$\lambda_\Gamma \sim \lambda_T \sim \lambda_p \sim \lambda_q$, such that D_\perp and χ_\perp can be approximated as

$$\lambda_n \sim \lambda_\Gamma \sim \sqrt{\tau_{\parallel n} D_\perp}$$

and

$$\lambda_T \sim \lambda_q \sim \sqrt{\tau_{\parallel T} \chi_\perp} . \quad (8)$$

In all the above expressions, the volumetric sources in the SOL were assumed to be negligible, which is reasonable for the simple SOL but not for the complex SOL, as defined in Sec. II. The influence of volumetric sources of particles S_n and heat S_q may be estimated by including these in Eqs. (3) and (4). For simplicity, let us consider the particle conservation equation, $\nabla \Gamma \approx S_n \approx S_{iz} - S_{rec}$, where S_{iz} and S_{rec} are the ionization and recombination densities (typically, $S_n \approx S_{iz} \gg S_{rec}$), which may be written as

$$\lambda_\Gamma = \frac{\Gamma_\perp}{S_{iz} + \Gamma_\parallel/L_\parallel^{iz}}$$

and

$$L_\parallel^{iz} \equiv \int_0^{L_\parallel} S_{iz} s_\parallel ds_\parallel / \int_0^{L_\parallel} S_{iz} ds_\parallel . \quad (9)$$

This expression differs from Eq. (3) in two respects:

1. The connection length L_\parallel is replaced by the ionization-weighted, parallel distance away from the target, L_\parallel^{iz} , which corresponds to the beginning of the recycling region L_r in Fig. 3; since $L_\parallel^{iz} < L_\parallel$, the parallel density removal time is thereby reduced, $\tau_{\parallel n}^{iz} = L_\parallel^{iz}/c_s < \tau_{\parallel n}$.

2. An additional (source) term appears in the denominator and tends to reduce λ_Γ when $S_n = S_{iz} - S_{rec}$ is positive and comparable to $\Gamma_\parallel/L_\parallel^{iz} \approx n/\tau_{\parallel n}^{iz}$.

Evidently, both of these effects act to increase the radial density gradient (reduce $\lambda_n \sim \lambda_\Gamma$). This is most clearly observed by rewriting the advective/diffusive expressions for λ_n and λ_Γ , Eq. (6), in terms of Eq. (9), which yields

$$\begin{aligned}\lambda_\Gamma &\approx \frac{v_{\perp n} \tau_{\parallel n}^{iz}}{1 + \alpha_{iz}} , \\ \lambda_n \lambda_\Gamma &\approx \frac{D_\perp \tau_{\parallel n}^{iz}}{1 + \alpha_{iz}} , \\ \tau_{\parallel n}^{iz} &\approx \frac{L_\parallel^{iz}}{c_s} ,\end{aligned}$$

and

$$\alpha_{iz} = \frac{S_{iz} \tau_{\parallel n}^{iz}}{n}. \quad (10)$$

Note that these complex SOL expressions reduce to the simple SOL expressions, Eq. (6), when $S_{iz} \ll n/\tau_{\parallel n}^{iz}$, in which case $\alpha_{iz} \rightarrow 0$, $L_{\parallel}^{iz} \rightarrow L_{\parallel}$ and $\tau_{\parallel n}^{iz} \rightarrow \tau_{\parallel n}$.

Similar expressions may be derived for λ_{T_a} and λ_{q_a} , starting with the heat conservation equation, $\nabla q_a \approx S_q \approx S_{heat} - S_{rad}$, where S_{heat} and S_{rad} are the volumetric densities of heating and radiation. Since S_{rad} is typically larger than S_{heat} in the SOL, S_q is generally negative and represents a net sink of heat. Thus, in contrast to the particle sources in the SOL, which are generally positive and thus tend to reduce λ_{Γ} and λ_n , energy sources are typically negative and thus tend to increase λ_{q_a} and λ_{T_a} , i.e., to broaden the temperature profiles.

II.B. Diamagnetic Transport

In the presence of strong radial gradients, as is the case in the near SOL, the magnetization condition $\delta_a = \rho_a/\lambda_a \ll 1$ and the associated scale separation, Eq. (2), are less pronounced, such that diamagnetic flux densities Γ_{\wedge} and $q_{\wedge a}$ can become comparable to parallel flux densities Γ_{\parallel} and $q_{\parallel a}$ and must be retained when calculating the net transport within the flux surface; i.e., the net poloidal flux densities Γ_{θ} and $q_{\theta a}$ should replace Γ_{\parallel} and $q_{\parallel a}$ in the estimate of the SOL radial extent in Eqs. (3) and (4). The poloidal projection of the leading diamagnetic flows in a divertor SOL configuration (see Sec. IV) is shown schematically in Fig. 10 in Ref. 8, with a normal direction of the toroidal magnetic field ($\mathbf{B} \times \nabla B$ toward the divertor). Since diamagnetic flows depend on the direction of the magnetic field (or, rather, the direction of $\mathbf{B} \times \nabla B$), all single arrows appearing in that figure would reverse when this direction is changed. For this reason, they have a significant effect on the time-average asymmetries in particle and power deposition on inner versus outer limiter or divertor plates (Sec. IV). More important, transient diamagnetic flows, which have opposite directions for ions and electrons, give rise to local charge separation and thus to fluctuating radial velocities, $v_{\perp} = \mathbf{E} \times \mathbf{b}/B \cdot \mathbf{e}_{\wedge} = E_{\wedge}/B$. When phase shifted with respect to local density fluctuations \tilde{n} and combined with a radial density gradient, these result in net radial particle outflow. Such phase shift can be produced by parallel resistivity or by unfavorable magnetic curvature, both of which lead to interchange-like motion of localized plasma structures. It is now widely accepted that this interchange mechanism, which naturally explains the ballooning nature of the observed radial fluxes—with outflow on the outboard side of the torus, on which the magnetic curvature is unfavorable—is the origin of plasma turbulence in the edge SOL region (see Sec. II.D).

II.C. Parallel Transport

Plasma transport along the magnetic field is, at least to first order, unaffected by the magnetic field and thus bears close resemblance to neutral gas dynamics, whether in their kinetic or fluid description. Nonetheless, it differs from gas dynamics in at least two major respects. The first is the formation of the magnetic presheath at the plasma-solid interface due to the mass difference between ions and electrons and their recombination at the solid surface. The main consequence of the sheath is the Bohm criterion, which states that the plasma enters the magnetic presheath with a fluid velocity no less than the local plasma sound speed, i.e., that the local parallel Mach number must exceed unity, $M_{\parallel} = v_{\parallel}/c_s \geq 1$. The second is the strong variation of $\chi_{\parallel e}$ with plasma temperature and density, arising from the fact that collisions impede parallel free streaming of heat and that the Coulomb collision cross section between charged particles decreases as the cube of their relative velocity. One thus obtains the Spitzer-Harm expression,^{9–11} $\chi_{\parallel e} = 3.2 v_{te} \lambda_e \propto L_{\parallel} v_{te}/\nu_e^* \propto T_e^{5/2}/n$, where v_{te} is the electron thermal velocity, $\lambda_e = v_{te} \tau_e$ is the electron-ion collisional mean-free-path, and $\nu_e^* = L_{\parallel}/\lambda_e \propto L_{\parallel} n T_e^{-2}$ is the electron collisionality.ⁱ When collisionality approaches unity, Spitzer-Harm diffusion reduces to parallel free-streaming of electron heat at some fraction of v_{te} , $q_{\parallel e} = \alpha_e v_{te} n T_e$, where α_e is known as the flux-limiting factor; heat flux limiting in SOL parallel transport is reviewed in Ref. 12. Combining these results with conservation equations of particles, momentum, and energy reveals three regimes of parallel plasma transport in the SOL (Ref. 13):

1. the sheath-limited/low recycling regime, relevant to low collisionality, $\nu_e^* < 10$, in which both temperature and pressure are roughly uniform along the magnetic field ($T_e/\nabla_{\parallel} T_e \approx p/\nabla_{\parallel} p \approx L_{\parallel}$) and parallel transport is dominated by the kinetic features of the plasma-surface interface, i.e., by the electrostatic sheath. Denoting the upstream, main SOL quantities by subscript u and solid target quantities by subscript t , the above constraints, which may be written as $T_u \approx T_t$ and $q_{\parallel u} \approx q_{\parallel t} = \gamma n_t T_t c_{st}$, together with total pressure conservation, $n_u T_u \approx (1 + M_t) n_t T_t \approx 2 n_t T_t$, define the sheath-limited regime and imply the following relations: $\Gamma_{\parallel t} \propto \Gamma_{0t} \propto n_t \propto n_u$ and $T_u \approx T_t \propto n_u^{-2/3}$, where Γ_{0t} is the flux of neutrals to the target.¹³

2. the conduction-limited/high-recycling regime relevant to moderate collisionality, $\nu_e^* \sim 10$ to 100, in which pressure remains uniform but parallel heat conduction is sufficiently impeded by collisions to support significant parallel temperature gradients in the region upstream of the near-target recycling flow, $T_e/\nabla_{\parallel} T_e \ll p/\nabla_{\parallel} p \sim L_{\parallel}$,

ⁱThis Spitzer-Harm expression is valid only under collisional conditions, $\nu_e^* \gg 1$.

while the recycling region is dominated by parallel convection (Fig. 3). Expressing the parallel heat flux density as $q_{\parallel} = n\chi_{\parallel e}\nabla_{\parallel}T_e = \kappa_{0e}T_e^{5/2}\nabla_{\parallel}T_e$ leads to the following relation between upstream and target temperatures: $T_u^{7/2} = T_t^{7/2} + 7q_{\parallel}L_{\parallel}/2\kappa_{0e}$. Using this relation in place of $T_u = T_t$, it is easily shown¹³ that $\Gamma_t \propto n_u^2$, $\Gamma_0 \propto n_t \propto n_u^3$, $T_t \propto n_u^{-2}$, and $T_u \propto n_u^0$. The experimental evidence for the transition from the low to the high recycling regime as n_u is increased is shown in Fig. 6 for a JET L-mode, diverted discharge in which a density scan was performed.¹⁵ Note the predicted change from $T_e \propto n_u^{-1}$ for low density to $T_e \propto n_u^0$ for high density and the fact that ions are warmer than electrons, $T_{iu}/T_{eu} \approx 2$, consistent with $\chi_{\parallel e}/\chi_{\parallel i} \sim 60$ and $T_{iu}/T_{eu} \propto (\kappa_{0e}/\kappa_{0i})^{2/7} \sim 3$.

3. the detached regime, relevant to high collisionality, $\nu_e^* > 100$, in which parallel plasma momentum is progressively removed by charge exchange collisions with neutrals (effective below $T_{et} \approx 5$ eV on JET), thus generating significant parallel pressure gradients, $T_e/\nabla_{\parallel}T_e \sim p/\nabla_{\parallel}p \ll L_{\parallel}$ (see Fig. 7). As a result, the plasma flux to the target and the target density decrease with upstream density, $\Gamma_t \propto n_u^{-\alpha}$ and $n_t \propto n_u^{-\beta}$, where $\alpha, \beta > 0$, while the

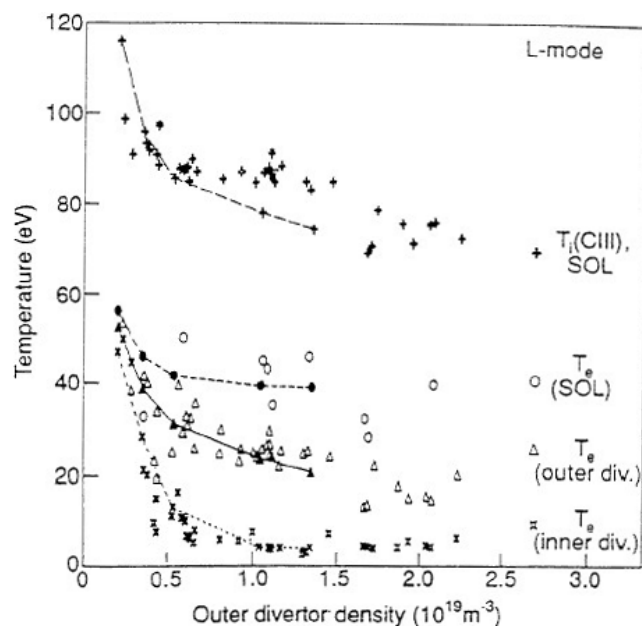


Fig. 6. Variation of inner T_{et}^{inner} and outer T_{et}^{outer} divertor target temperatures and of upstream electron T_{eu} and ion T_{iu} temperatures with the outer target density n_t^{outer} . The data were taken during a JET NBI-heated (L-mode), MkI diverted discharge in which the density was gradually increased by an additional gas puff. Electron temperatures were measured using fast-scanning, reciprocating probes,¹⁴ whereas ion temperatures were inferred from the widths of the CIII emission line. Reproduced with permission from Ref. 15.

target neutral flux continues to increase with n_u (Figs. 4 and 5). If volumetric recombination becomes significant (typically below $T_{et} \approx 1$ eV on JET), the target density tends toward zero and the plasma enters a strongly detached regime.

One might expect the upstream plasma to be virtually stagnant in a complex SOL due to the localized plasma recycling in the divertor volume, irrespective of the SOL transport regime. On the contrary, strong parallel flows, with Mach number of order unity, are observed over much of the SOL when the $\mathbf{B} \times \nabla B$ direction points toward the X point (the flows are smaller and toward the outer target when $\mathbf{B} \times \nabla B$ direction is reversed).^{17–20} Systematic studies of parallel SOL flow on JET were first performed in MkIIGB divertor SOL plasmas.^{19,20} The upstream SOL particle flux and parallel Mach number profiles for typical MkIIGB ohmic plasmas are shown in Fig. 8. The parallel SOL flows are believed to originate due to a combination of Pfirsch-Schlütter return flows^{21,22} and ballooning return flows caused by the turbulent outflow of plasma on the low-field side of the tokamak^{23,24} (see Sec. II.D).

II.D. Plasma Turbulence in the SOL

Since the SOL plasma is both tenuous and cold compared to the core or edge (pedestal) plasmas, it is often neglected, or rather approximated as a vacuum envelope, when considering the global stability against fast MHD motions. This omission, although clearly reasonable, is rarely taken to its logical conclusion, namely, that the SOL plasma is not in MHD equilibrium. This is not to say that nested magnetic flux surfaces are necessarily destroyed in the open field line region, but rather that their origin lies almost exclusively in currents external to the SOL—the toroidal field being generated due to external poloidal coils, the poloidal field due to toroidal currents inside the LCFS, including any edge-localized bootstrap current—such that the SOL plasma carries only a small toroidal current in response to the toroidal inductive electric field (EMF) in a pulsed tokamak. The cause of this behavior is twofold: First, the SOL plasma is cold and thus electrically resistive^j; second, the presence of open field lines, which terminate at either end with electrostatic sheaths at solid targets, likewise impedes charge flow and gives rise to a sheath resistivity η_{\parallel}^{sh} . The large effective SOL resistivity, $\eta_{\parallel}^{SOL} = \eta_{\parallel}^{coll} + \eta_{\parallel}^{sh}$, invalidates the cornerstone assumption of ideal MHD, $\mathbf{E}' = \mathbf{E} + \mathbf{V} \times \mathbf{B} = \eta_{\parallel} \mathbf{j} = 0$, known as the ideal MHD Ohm's law, along with such results as the frozen-in property of the magnetic flux and the Grad-Shafranov equation of two-dimensional (2-D) MHD equilibrium. Consequently, the

^jRecall that low T_e and high ν_e^* imply high resistivity, $\eta_{\parallel}^{coll} \propto n/\nu_{ei} \propto T_e^{-3/2}$.

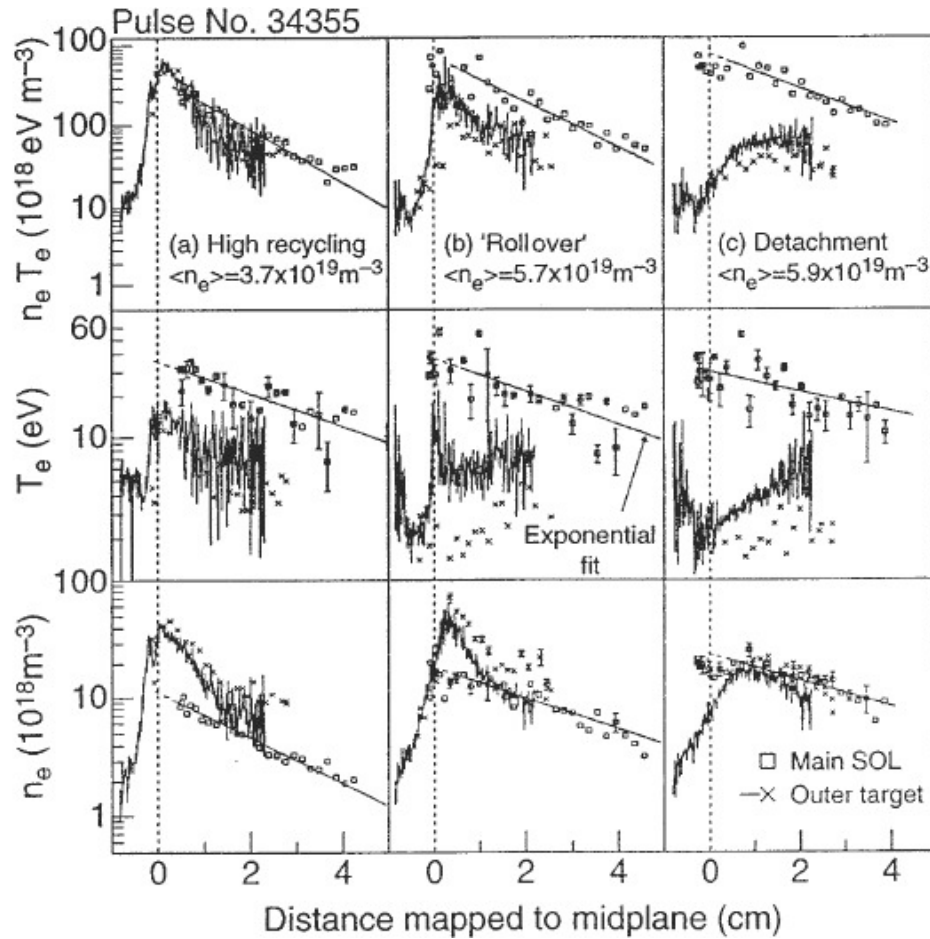


Fig. 7. Radial profiles of electron pressure (top), density (middle), and temperature (bottom) in the upstream SOL and at the outer divertor target of an MKI L-mode discharge. The three columns represent a density scan by additional gas puffing: (left) high recycling regime, (middle) the plasma flux “rollover,” and (right) partial detachment. Reproduced with permission from Ref. 16.

SOL cannot be in equilibrium in the sense of ideal MHD^k and is thus inherently unstable to a range of dynamical instabilities, first among which are the already mentioned interchange motions.

Parallel electrical resistivity has an equally strong effect on the dynamical evolution of the SOL plasma, which is clearly unable to follow the fast, electromagnetic (EM), MHD ordering and evolves instead according with the slower, electrostatic (ES), drift ordering. The two orderings, which are discussed extensively in Ref. 1, are defined in terms of the speed of transverse plasma motions compared to the plasma sound speed, i.e., in terms of the transverse Mach number M_{\perp} , with $M_{\perp} \sim 1$ in the MHD ordering and $M_{\perp} \ll 1$ in the drift

ordering. The two ordering schemes lead to a different relation between magnetic flux tubes and plasma filaments: in MHD ordering the two terms are practically synonymous, with the plasma filament frozen into the magnetic flux tube, whereas in drift ordering, the filament drifts across a succession of nearly stationary flux tubes.²⁵

Based on these observations, one would expect to find quite intense ES turbulent activity in the SOL but only moderate levels of EM turbulence, typically identified with magnetic flutter. The radial flux densities associated with each type of turbulence may be estimated as

$$\Gamma_{\perp}^{\text{ES}} \equiv \langle n v_{\perp} \rangle = \frac{\langle \tilde{n} \tilde{E}_{\perp} \rangle}{B},$$

$$q_{La}^{\text{ES}} \equiv \frac{3}{2} \langle n T_a v_{\perp} \rangle \approx \frac{3}{2} T_a \Gamma_{\perp}^{\text{ES}} + \frac{3}{2} n \frac{\langle \tilde{T}_a \tilde{E}_{\perp} \rangle}{B}, \quad (11)$$

^kThis is because the parallel return currents required to balance the thermal and Lorentz forces, $\nabla p = \mathbf{j} \times \mathbf{B}$, are impeded by the large $\eta_{\parallel}^{\text{SOL}}$.

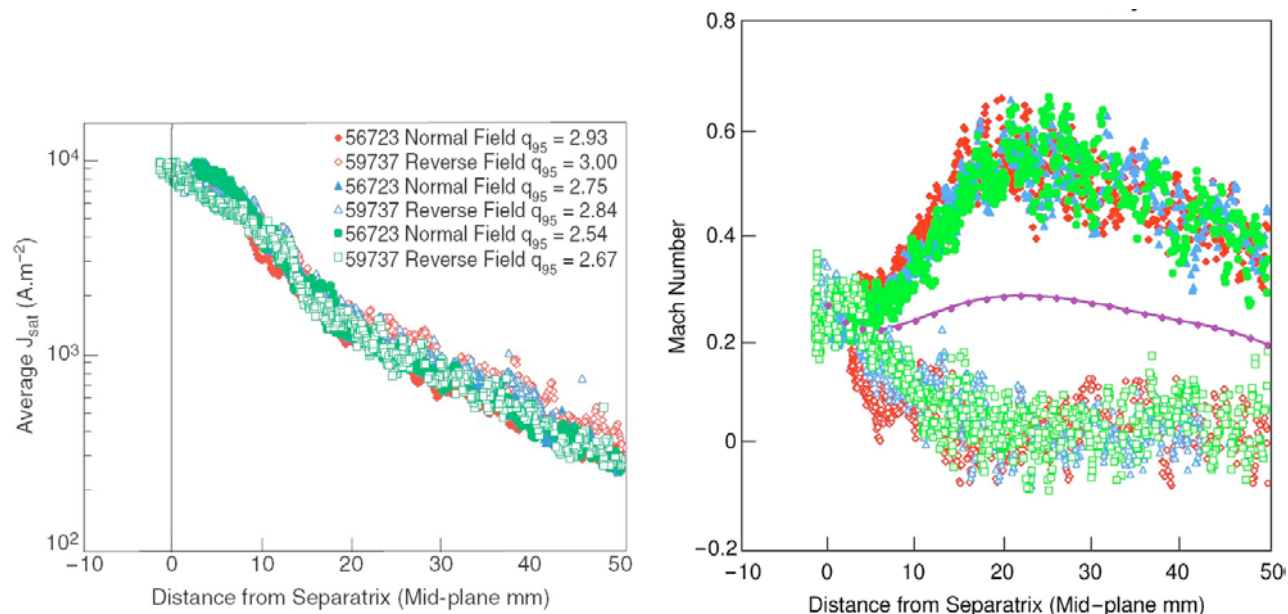


Fig. 8. Ion saturation current (left) and parallel Mach number (right) profiles measured by a reciprocating Mach probe located near the top of the JET vessel, in normal ($\mathbf{B} \times \nabla B$ toward the X point) and reversed ($\mathbf{B} \times \nabla B$ away from the X point) field directions in JET MkIIIGB divertor ohmic plasmas. The average value represents the $\mathbf{B} \times \nabla B$ -independent part of the flow, which shows a clear ballooning character (positive values indicate flow toward the inner divertor). Reproduced with permission from Ref. 20.

and

$$\Gamma_{\perp}^{\text{EM}} \approx \frac{\langle \tilde{n} c_s \tilde{B}_{\perp} \rangle}{B},$$

$$q_{\perp e}^{\text{EM}} \approx \frac{5}{2} T_e \Gamma_{\perp}^{\text{EM}} - q_{\parallel e} \left\langle \frac{\tilde{B}_{\perp}^2}{B^2} \right\rangle \frac{L_{\parallel}}{\lambda_{Te}}, \quad (12)$$

where the tilde denotes a fluctuating quantity, $\tilde{A} = A - \langle A \rangle$, the angle brackets represent a temporal average, and $q_{\perp a}$ are written as the sum of the convective and conductive terms. Measurements on a number of tokamaks, including JET, indicate that the relative fluctuations of density (\tilde{n}/n), temperature (\tilde{T}/T), and electric potential ($e\tilde{\varphi}/T_e$) approach unity in the SOL, whereas magnetic fluctuations are always much smaller than one, typically $\tilde{B}/B \sim 10^{-4}$. Recalling the earlier discussion, we may conclude that SOL turbulence is dominated by ES, drift-ordered dynamics.^{26,27} It is worth noting that since fluctuations in SOL quantities are comparable to ambient values, their dynamics cannot be described by standard quasi-linear turbulence theories and require instead a fully nonlinear treatment. In fact, as one moves away from the LCFS, \tilde{n}/n , \tilde{T}_e/T_e , and $e\tilde{\varphi}/T_e$ increase above unity and exhibit bursty, intermittent time signatures. This SOL intermittency can be interpreted as quasi-periodic ejection and radial movement of isolated, field-aligned structures, variously known as blobs or filaments, which advect

particles, momentum, and energy into the far SOL (Refs. 28 through 33). When averaged over all scales, this radial advection is the origin of the enhanced, or anomalous, radial transport in the SOL. It is worth noting that the large radial electric fields in the near SOL and the associated poloidal velocity shear (zonal flow) play an active and self-regulating role in edge SOL turbulence by decorrelating (effectively ripping apart) coherent structures, thus reducing radial turbulent fluxes; this mechanism has been demonstrated in numerical simulations of SOL turbulence (e.g., Ref. 34). To conclude, the theoretical framework of SOL turbulence thus appears to be well established and capable of explaining the observed phenomenology.

II.E. Effect of the H-Mode and ELMs on the SOL

For a brief and accessible introduction to the high-confinement regime (H-mode) in tokamaks and the related topic of edge-localized modes (ELMs), Ref. 35 is highly recommended. There are also several fine reviews of these subjects in the topical literature.^{36–47} For more information on ELM transport in the SOL, the reader is referred to a recent topical review⁴⁸; the key results of relevance to ITER are summarized in Refs. 49 and 50.

From the point of view of the SOL, ELMs can be viewed as semiperiodic eruptions of hot, dense plasma from the edge (pedestal) region, which on JET expel up to 10% of the plasma stored energy. There is now ample

evidence from many machines to suggest that this ejection is not uniform in space but occurs preferentially on the low-field side of the torus, i.e., exhibits ballooning character, and is localized in field-aligned, filamentary structures. The highly intermittent nature of these eruptions (typical inter-ELM time ~ 10 to 100 ms; typical ELM duration < 1 ms) motivates the division of SOL transport into the inter-ELM and ELM phases. For some applications, e.g., power loading on the target plates, one may also speak of ELM-averaged transport, which represents transport processes averaged over timescales much longer than the inter-ELM time.

Soon after the H-mode regime was first established on JET in the Mk0 divertor configuration, it was observed that following the $L \rightarrow H$ transition, the SOL density profiles became significantly steeper, and hence narrower, than the L-mode profiles.⁵¹ Averaged over the SOL, the degree of steepening varied from as little as 50% to more than a factor 2 (Ref. 51), but in the near-SOL region the H-mode profiles were up to 10 times steeper. Such an increase in the radial gradients is consistent with the reduction in edge turbulence (formation of the edge transport barrier) and hence the reduction of radial edge transport coefficients in the H-mode regime. Lower transport (improved confinement) produced a transient reduction in the particle flux crossing the LCFS and thus reaching the divertor; the particle confinement time, calculated based on the exponential recovery of the particle flux, was estimated as $\tau_p^{*H} \approx 0.5$ s in the H-mode phase, which was a factor of 3 larger than in the L-mode phase, $\tau_p^{*L} \approx 0.15$ s.

III. LIMITER SOL

Before the installation of the MkI divertor, JET was operated initially with discrete poloidal limiters, followed by two toroidal belt limiters, initially made from graphite, then replaced by beryllium. The belt limiters were removed during the installation of the MkI divertor and replaced by a dozen or so poloidal graphite limiters, which aside from occasional tile replacement are still on the machine today. Thus, JET offers a wealth of data on limiter SOL behavior, including the effect of limiter material, wall conditioning, and heating methods. The database of LCFS quantities and SOL profiles in JET limiter discharges was compiled in Refs. 52, 53, and 54 and its implications discussed in Refs. 55 and 56. With some modification these results are presented here and summarized in Table I.

III.A. Carbon Limiters

III.A.1. Ohmically Heated Discharges

During its “limiter” period (up to 1993), the standard mode of JET operation involved forming the LCFS on the outboard (poloidal or toroidal) limiters, although occasionally the LCFS was also formed on the inner wall. Radial profiles of $j_{sat} = \Gamma/e$, T_e , and n_e in the SOL in these limiter plasmas have been measured using a fast scanning Langmuir probe, reciprocating into the SOL near the top of the torus; plasma diagnosis by electrical, including Langmuir, probes is reviewed in Ref. 14.

TABLE I

Summary of Empirical Scalings of SOL Density and Temperature on the LCFS and Their Radial E-Folding Lengths in the SOL in JET Limiter and Divertor Discharges*

Configuration (Mode)	$n_e^{LCFS} \propto$	$T_e^{LCFS} \propto$	$\lambda_n, \lambda_T \propto$	$\lambda_{T_e}, \lambda_{p_e}, \lambda_q \propto$
Limiter discharges				
C, ohmic (Ω)	$(\bar{n}_e)^1$ to $(\bar{n}_e)^2$	$(\bar{n}_e)^{-2}$ to $(\bar{n}_e)^{-3}$	I_p^{-1}	$\bar{n}_e I_p^{-1.3}$
C, NBI (L)	—	—	$I_p^{-1.2} P_{NBI}^0$	$I_p^{-1.2} P_{NBI}^{0.4}$
C, ICRH (L)	—	—	$I_p^{-1.2} P_{ICRH}^{0.3}$	$P_{ICRH}^{0.5}$
Be, (L)	$(\bar{n}_e)^1$ to $(\bar{n}_e)^3$	$(\bar{n}_e)^{-0}$ to $(\bar{n}_e)^{-2}$	\bar{n}_e	\bar{n}_e
Divertor discharges				
Mk0, horizontal, Be (Ω, L)	$(\bar{n}_e)^2$	$(\bar{n}_e)^{-0}$ to $(\bar{n}_e)^{-1}$	$(\bar{n}_e)^0$ to $(\bar{n}_e)^1$	\bar{n}_e
Mk0, horizontal, C (Ω, L)	—	—	$(\bar{n}_e)^{0.3}$	—
MkI, horizontal, C (Ω, L)	$(\bar{n}_e)^2$	$(\bar{n}_e)^0$	$(\bar{n}_e)^{0.4}$ to $(\bar{n}_e)^{0.5} \times P_{tot}^{0.25}$ to $P_{tot}^{0.75}$	$(\bar{n}_e)^{0.75}$ to $(\bar{n}_e)^1 \times P_{tot}^0$ to P_{tot}^1
MkI, vertical, C (Ω, L)	—	—	$(\bar{n}_e)^0$	—
MkI, C (Ω, L)	—	—	$(\bar{n}_e/n_{GW})^{0.4} q_{95}^{0.4} P_{tot}^{0.3}$	$(T_e^{LCFS})^{-1.35} q_{95}^{0.4} P_{tot}^{0.45}$
MkIIA, NBI (L)	—	—	$B_\phi^{-0.8} q_{95}^{1.3} (\bar{n}_e)^{0.1} P_{SOL}^{-0.4}$	$B_\phi^{-0.8} q_{95}^{1.3} (\bar{n}_e)^{0.7} P_{SOL}^{-0.5}$
MkIIGB, NBI (L)	$(T_e^{LCFS})^2$	$(n_e^{LCFS})^{1/2}$	$\propto \lambda_q$	$q_{95} P_{SOL} (n_e^{LCFS})^{-1.2}$
MkIIGB, NBI (H)	—	—	—	$\lambda_q \propto A^\alpha Z^\beta B_\phi^{-0.93} q_{95}^{0.41} P_t^{-0.48} n_{eu}^{0.15}$

*The auxiliary heating method (NBI, ICRH), type of target material (C, Be), divertor targets used (horizontal or vertical), and mode of plasma operation (ohmic, L-mode, or H-mode) are also indicated in the configuration column. Note that in the final row, $\alpha + \beta = 1.1$.

It is instructive to begin the discussion by comparing the inboard-, or high-field-side- (HFS-), limited and the outboard-, or low-field-side- (LFS-), limited SOLs. Such a comparison is possible because of a carefully controlled study of two phases of a single ohmic discharge, the first limited on the inner wall (IW = HFS), the second on the lower belt (LB = LFS) limiter.⁵⁷ The change from the HFS-limited to the LFS-limited phase was accomplished by moving the plasma outward as a rigid body by ≈ 5 cm. The core plasma parameters were nearly identical during the two phases ($I_p = 3.1$ MA, $B_\phi = 2.9$ T, $\bar{n}_e \approx 2.5 \times 10^{19} \text{ m}^{-3}$, $P_{\text{SOL}} \approx 1.7$ MW, and $Z_{\text{eff}} \sim 4$), and helium was used as the background species to minimize effects of flow amplification due to ionization in the SOL.

Typical radial SOL profiles, plotted versus the radial distance at the probe location, are shown in Fig. 9 for the LFS phase (left) and the HFS phase (right). It is immediately obvious that the HFS phase profiles are much broader. Defining the enhancement factors of HFS phase compared to LFS phase quantities as $E(\mathcal{A}) \equiv \mathcal{A}^{\text{HFS}} / \mathcal{A}^{\text{LFS}}$, one finds that radial e-folding lengths of density, particle flow, and power flow are enhanced by a factor of ≈ 3 , and the temperature by a factor of ≈ 1.5 :

$$E(\lambda_n) \approx 55/17 \approx 3.2, \quad E(\lambda_T) \approx 100/76 \approx 1.3, \quad (13)$$

$$E(\lambda_\Gamma) \approx 44/14.5 \approx 3.0, \quad E(\lambda_q) \approx 30/12 \approx 2.5, \quad (14)$$

and

$$E(n\lambda_\Gamma) \approx 1.7 \times 3.1 \approx 5.3, \quad (15)$$

$$E(nT_e\lambda_q) \approx 1.7 \times 1.2 \times 2.5 \approx 5.1. \quad (15)$$

These are averages of ion and electron side quantities. The last two items, which represent enhancement factors of integrated fluxes of particles and power, are more than twice larger than expected based on plasma flow along a magnetic flux tube whose cross-sectional area scales inversely with toroidal magnetic field (due to magnetic flux conservation); i.e., $n\lambda_\Gamma \propto nT_e\lambda_q \propto B_\phi(R) \propto R^{-1}$ such that $E(n\lambda_\Gamma) = E(nT_e\lambda_q) = 2.2$. The origin of the additional enhancement of $\approx 5.2/2.2 \approx 2.4$ has not been resolved. The authors in Ref. 57 suggest subsonic flow into the inner-wall sheath, which they justify by the highly

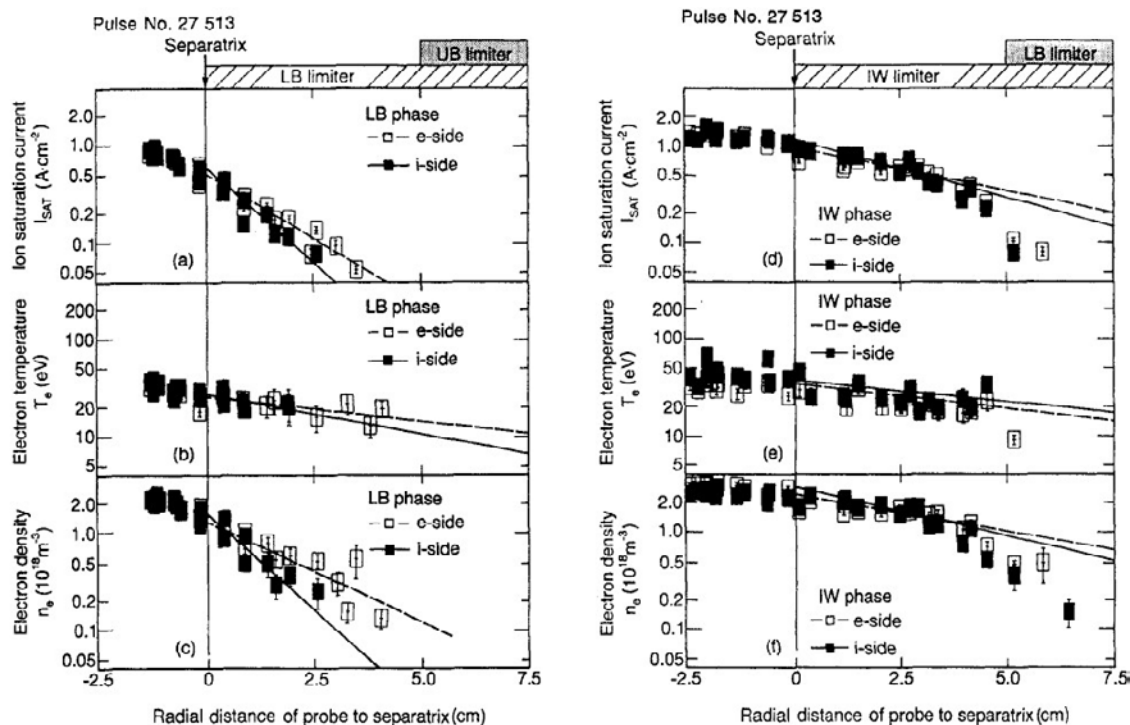


Fig. 9. Radial SOL profiles of $j_{\text{sat}} = \Gamma/e$, n , and T_e for LFS- (left) and HFS- (right) limited phases of JET pulse 27513. Horizontal axis is the radial distance at the position of the probe (which is 2.5 times larger than the radial distance at the outer midplane). Mapped to the outer midplane, the LFS phase e-folding lengths are found to be $\lambda_n \approx 7$ mm, $\lambda_T \approx 30$ mm, and $\lambda_q \approx 5$ mm. Reproduced with permission from Ref. 57.

grazing angle of incidence there (≈ 0.12 deg), for which the Bohm criterion could potentially be violated. More likely, the enhancement is caused by ballooning transport, which would tend to produce $E(L_{\parallel}) \approx 2m - 1$, where $\theta = \pi/m$ is the poloidal angle (from outer mid-plane) measuring the extent of uniform radial outflow. Since according to Eq. (6), $E(\lambda_n) \approx E(L_{\parallel})^{1/2}$, we can estimate the required $E(L_{\parallel})$ as $2.4^2 \approx 5.8$ or $\theta \approx \pi/3.4 \approx 50$ deg. For comparison, to account for the observed $E(\lambda_n)$ by ballooning transport alone requires $E(L_{\parallel}) \approx 3.2^2 \approx 10$ or $\theta \approx \pi/10 \approx 20$ deg. This range of values is comparable to those inferred in similar experiments on the Tore Supra,⁵⁹ where ballooning transport was established as the main cause of the observed profile broadening. However, unlike the Tore Supra experiments, where strong parallel flow (required by ballooning transport) was measured at the probe location during the HFS phase, JET experiments indicate only weak or moderate parallel flows at the probe location.

Since LFS-limited plasmas offer a larger plasma volume and limiter wetted area, they were historically the preferred choice for plasma operation. As a result, LFS-limited SOL profiles have been characterized more extensively than their HFS-limited counterparts. The results of one such systematic study, consisting of a scan in magnetic field B_{ϕ} , plasma current I_p , and line average

density \bar{n}_e for JET ohmic discharges using the earlier, poloidal limiters, are shown in Figs. 10 and 11.

We first consider the variation of electron density n_e^{LCFS} and temperature T_e^{LCFS} on the LCFS with \bar{n}_e and I_p (or ohmic heating power P_{Ω} , which is related roughly linearly to the plasma current $P_{\Omega} \approx 0.7I_p^{1.15}$), with power in MW and current in MA (Fig. 10). At fixed I_p (P_{Ω}), one finds

$$n_e^{\text{LCFS}} \propto (\bar{n}_e)^1 \text{ to } (\bar{n}_e)^2 ,$$

$$T_e^{\text{LCFS}} \propto (\bar{n}_e)^{-2} \text{ to } (\bar{n}_e)^{-3} ,$$

and

$$\Gamma_{\parallel}^{\text{LCFS}} \propto n_e T_e^{1/2} \propto (\bar{n}_e)^0 \text{ to } (\bar{n}_e)^{1/2} . \quad (16)$$

Note that $p_e^{\text{LCFS}} \propto (\bar{n}_e)^{-1}$ across this entire range. As I_p (P_{Ω}) increases, so do n_e^{LCFS} , T_e^{LCFS} , $\Gamma_{\parallel}^{\text{LCFS}}$, and p_e^{LCFS} (Fig. 10); the latter is consistent with the linear increase of $\tau_E \propto nT_e/P_{\text{heat}}$ with I_p , and its decrease as the square root of P_{heat} , as described by most empirical scalings, e.g., the Goldstone L-mode scaling, $\tau_E \propto I_p P_{\text{heat}}^{-1/2} \propto I_p^{1/2}$ for $P_{\text{heat}} \propto P_{\Omega} \propto I_p$. Similarly, the approximate dependence inferred from Fig. 10 (right frame),

$$T_e^{\text{LCFS}} \propto I_p (\bar{n}_e)^{-2} \propto P_{\Omega} (\bar{n}_e)^{-2} , \quad (17)$$

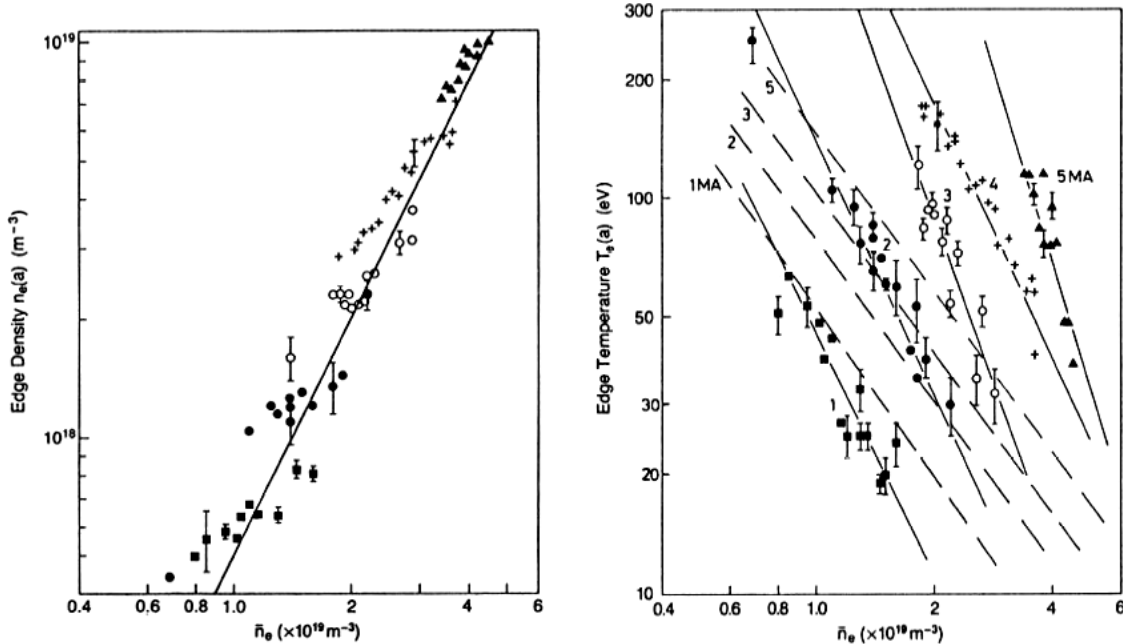


Fig. 10. Variation of the density and electron temperature at the LCFS with line average density in JET limiter ohmic discharges. Solid squares, 1 MA, 2.1 T; solid circles, 2 MA, 2.1 T; open circles, 3 MA, 3.4 T; crosses, 4 MA, 3.4 T; and solid triangles, 5 MA, 3.4 T. The solid line in the left figure represents Eq. (18), $n_e^{\text{LCFS}} \propto (\bar{n}_e)^2$, with neutral penetration velocity of $v_0 = 30$ km/s. The solid lines in the right figure are fits to the data, and the dashed lines are predictions of a basic model $T_e^{\text{LCFS}} \propto I_p^{2/3} (\bar{n}_e)^{-4/3}$; much better agreement is found using the model based on empirical particle confinement time, which yields $T_e^{\text{LCFS}} \propto I_p (\bar{n}_e)^{-1.8}$. Reproduced with permission from Ref. 60.

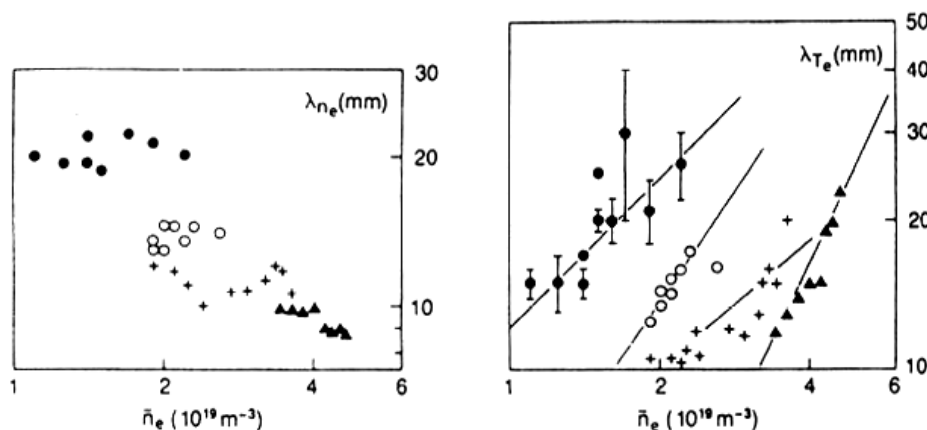


Fig. 11. Variation of radial e-folding lengths of SOL density and temperature with line average density in JET limiter ohmic discharges. The notation is the same as in Fig. 10. Reproduced with permission from Ref. 5.

is consistent with the empirical particle confinement time scaling $\tau_p \propto (\bar{n}_e)^{-0.8}$, which leads to the prediction $T_e^{\text{LCFS}} \propto P_\Omega (\bar{n}_e)^{-1.8}$; note that, as expected, $p_e^{\text{LCFS}} \propto P_\Omega$. The same model predicts $n_e^{\text{LCFS}} \propto P_\Omega^{-1/2} (\bar{n}_e)^{2.7}$, which is in fair agreement with the I_p scan data in Fig. 10 (left frame) but overestimates the density dependence for any given value of I_p .

The above behavior of n_e^{LCFS} and T_e^{LCFS} with \bar{n}_e may be understood in terms of a simple, one-dimensional model of particle balance in which the plasma is fueled by radial influx of neutrals and is depleted by a diffusive, ambipolar outflux of ions and electrons. Equating these two fluxes yields the following relation for the LCFS plasma density:

$$n_i^{\text{LCFS}} \approx \frac{\lambda_n n_i^{\text{ped}}}{\lambda_0} \approx \frac{(\bar{n}_i)^2 \lambda_n \sigma_0}{2} \approx \frac{(\bar{n}_i)^2 \lambda_n \langle \sigma_{iz} v \rangle}{2v_0}, \quad (18)$$

where the n_i^{ped} refers to the density at the pedestal location, i.e., $r_{\text{ped}} \approx r_{\text{LCFS}} - \lambda_0$, σ_0 is given by Eq. (1), and the effective neutral penetration velocity is defined as $v_0 = \langle \sigma_{iz} v \rangle / \sigma_0$. Since λ_0 scales inversely with n_i^{ped} , the model predicts that the LCFS density will increase as $(\bar{n}_e)^2$, in agreement with the I_p scan data. The reduction of T_e^{LCFS} as the square-cube of \bar{n}_e is then a direct consequence of the compression of the edge plasma, which requires less energy per ion-electron pair leaving the core. It is significant that the $(\bar{n}_e)^2$ dependence predicted by Eq. (18), and observed at high densities, is due to a diffusive plasma outflux, $\Gamma_\perp \sim D_\perp \nabla_\perp n \sim D_\perp n / \lambda_n$; in contrast, an advective outflux, $\Gamma_\perp \sim n v_\perp$, results in a linear density scaling, as observed at lower densities. This suggests that radial outflux in the edge, or pedestal, region is advective at low densities and diffusive at higher densities, for any given value of I_p .

We next turn to consider the variation of radial e-folding lengths in the SOL. An early study⁶¹ indicated typical values of $\lambda_n \approx 30$ to 60 mm and $\lambda_{T_e} \approx 50$ to 100 mm, measured at the probe, for plasma currents ranging from 1 to 3 MA. Later,^{60,62} an inverse dependence on plasma current was established (see Fig. 11), which may be approximated as

$$\lambda_\Gamma^\Omega \approx 30 I_p^{-1}, \quad \lambda_{T_e}^\Omega \approx 3 \times 10^{-18} \bar{n}_e I_p^{-1.3}, \quad (19)$$

where the line average density is in units of m^{-3} , the plasma current in MA, and the e-folding lengths in mm; these are once again defined in terms of vertical distance at the probe location and must be reduced by a factor of ≈ 2 to 2.5 when mapped to the outer midplane. At low density, λ_n decreases slowly, and λ_q increases slowly, with \bar{n}_e , whereas at high density ($> 3 \times 10^{19} \text{ m}^{-3}$), λ_n and λ_q are independent of \bar{n}_e . Note that at low density $\lambda_n / \lambda_{T_e} > 1$, whereas at higher density $\lambda_n \rightarrow \lambda_\Gamma$ so that $\lambda_n / \lambda_{T_e} \rightarrow 10^{19} I_p^{0.3} / \bar{n}_e < 1$. Similar results were obtained with toroidal belt limiters,⁶³ although the absolute value of λ_n was found to be roughly 25% smaller, consistent with shorter connection lengths in the belt-limiter configuration. In addition, both λ_n and λ_T were found to scale as I_p^{-1} .

For constant toroidal field, which is the case for most of the data points in Fig. 11, I_p is linearly proportional to the poloidal magnetic field B_θ is inversely proportional to the safety factor at the 95% flux surface q_{95} and to the parallel connection length $L_\parallel \approx \pi R q_{95}$, and is nearly linearly related to the ohmic heating power and LCFS pressure:

$$I_p \propto B_\theta \propto q_{95}^{-1} \propto L_\parallel^{-1} \propto P_\Omega^{0.85} \propto (p_e^{\text{LCFS}})^{0.85}. \quad (20)$$

Using Eqs. (17) and (20), one may thus rewrite Eq. (19) as

$$\lambda_n^\Omega \approx \lambda_\Gamma^\Omega \propto L_\parallel, \quad \lambda_{T_e}^\Omega \propto L_\parallel^{1.3} \bar{n}_e \propto L_\parallel^{0.7} (T_e^{\text{LCFS}})^{-1/2}. \quad (21)$$

Note that the effect of the toroidal field B_ϕ is difficult to extract from the data since B_ϕ was varied for only one set of discharges. Combining Eqs. (6) and (21), one obtains the effective particle velocity and diffusivity as

$$v_{\perp n}^\Omega \propto c_s^{\text{LCFS}} \propto (T_e^{\text{LCFS}})^{1/2}, \quad D_\perp^\Omega \propto L_\parallel c_s^{\text{LCFS}} \propto L_\parallel (T_e^{\text{LCFS}})^{1/2}, \quad (22)$$

with typical values of $D_\perp \sim 0.1$ to $1 \text{ m}^2/\text{s}$ and $v_\perp \sim 10$ to 100 m/s . Note that Eq. (17) implies that D_\perp scales inversely with both line average density and the square root of the plasma current; the inverse scaling with \bar{n}_e was already derived in Ref. 64. This result can also be obtained by recalling Eq. (8) and subsequent discussion, which suggest that the SOL density profile is most simply explained in terms of radial advection with $v_{\perp n}/c_s^{\text{LCFS}} \propto \text{constant}$, for which Eq. (8) yields $\lambda_n/L_\parallel \propto \text{constant}$, in agreement with Eq. (21).¹ The derived scaling of Eq. (22) is consistent with theories of interchange-(curvature-) driven SOL turbulence, which predict plasma filaments to move radially with a velocity proportional to the plasma sound speed.³⁴

Assuming sheath-limited parallel transport (generally applicable to limiter SOL on JET), the effective velocity and diffusivity of heat transport may be derived using Eqs. (7) and (21):

$$v_{\perp T}^\Omega \propto L_\parallel^{-0.3} \propto (p_e^{\text{LCFS}})^{0.25} \quad (23)$$

and

$$\chi_\perp^\Omega \propto L_\parallel^{-0.6} \propto (p_e^{\text{LCFS}})^{0.5}. \quad (24)$$

With conduction-limited parallel transport, these expressions for $v_{\perp T}$ and χ_\perp have to be divided by $\nu_{e,\text{LCFS}}^*$ and $\nu_{e,\text{LCFS}}^{*2}$, respectively. Note that both coefficients in Eq. (23) increase moderately with plasma current, ohmic heating power, and LCFS pressure; e.g., $v_{\perp T} \propto L_\parallel^{-0.3} \propto I_p^{0.3} \propto P_\Omega^{0.25} \propto (p_e^{\text{LCFS}})^{0.25}$.

To summarize, in ohmically heated JET limiter discharges, radial transport in the edge, or pedestal, region appears to be dominantly advective/convective at low density and dominantly diffusive/conductive at high density. Radial transport in the SOL appears to be dominantly advective/convective, with SOL transport coefficients most easily represented in terms of effective radial velocities, $v_{\perp n} \propto c_s$ and $v_{\perp T} \propto L_\parallel^{-0.3}$.

¹Although it is not possible to distinguish between advective and diffusive transport based on radial profile scaling alone, there is ample evidence from a number of tokamaks to suggest that SOL particle transport is indeed dominated by radial motion of field-aligned filaments or blobs, i.e., by radial advection of mass.

III.A.2. NBI-Heated Discharges

When additional power is coupled to the plasma, the above expressions are modified depending on the type of heating method, which can be generally divided into NBI and rf heating.

NBI heating is more straightforward to consider, since it transfers most of the injected power directly to the core plasma. This can be inferred from the rise time of SOL quantities following the beginning of NBI heating, which change on the timescale of the global energy confinement time, typically $\sim 0.5 \text{ s}$. Thus, NBI does not directly heat the SOL, but rather, NBI power is conveyed to the SOL by radial convection and conduction across the LCFS. It should be noted that suprathermal particles are promptly observed in the SOL following the start of NBI heating and can be attributed to shine-through losses, beam-plasma charge exchange, and loss of fast ions on large banana orbits and those trapped in toroidal ripple magnetic wells. However, these fast particles, which represent a high-energy tail of the velocity distribution and thus only a small fraction of the total SOL population, do not affect the bulk, thermal population.

For pure NBI-heated plasmas,^{62,65} the particle flux e-folding length shows little, if any, dependence on the NBI heating power and decreases somewhat stronger than linearly with the plasma current, $\lambda_\Gamma \propto I_p^{-1.2}$, in fair agreement with the ohmic scaling of Eq. (19); the density e-folding length, shown in Fig. 12, exhibits a similar scaling, $\lambda_n \propto I_p^{-1.2}$. The temperature e-folding length increases slowly with input power, $P_{\text{tot}} = P_\Omega + P_{\text{NBI}}$, mainly

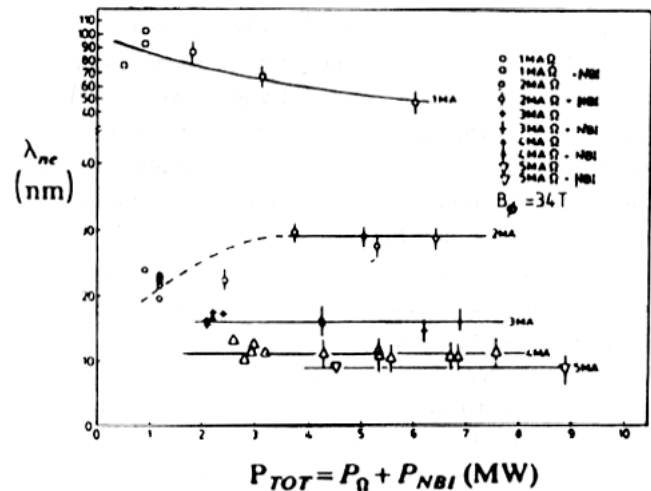


Fig. 12. Variation of radial e-folding length (in mm) of SOL density with total input power in JET limiter ohmic (open symbols without vertical bars) and NBI-heated (open symbols with bars) discharges for several values of plasma current from 1 to 5 MA (from top to bottom in descending order) for a toroidal field of 3.4 T. Reproduced with permission from Ref. 65.

due to the observed increase of \bar{n}_e with P_{tot} , which according to Eq. (21) should lead to a similar increase in λ_{T_e} ; large scatter in the temperature data prevents an accurate determination of the power law exponent. Finally, the parallel power e-folding length is found to scale as $\lambda_q \propto P_{tot}^{0.4} I_p^{-1.2}$, with most of the heating power dependence ascribed to temperature profile broadening. We may conclude that, to first order, the nature of SOL transport is not modified by NBI heating, i.e., that radial transport in the limiter SOL is governed by the same physical mechanism in ohmic and L-mode plasmas. Although limiter H-modes have been obtained on JET (see Sec. II.E), their SOL profiles have not been sufficiently studied to justify a separate discussion; H-mode SOL profiles in divertor discharges are discussed in Sec. II.E.

III.A.3. ICRH Discharges

In contrast to NBI heating, ICRH produces an almost instantaneous increase in n_e and T_e across the SOL—on the timescale of the rise time of the antenna, typically $<200 \mu\text{s}$ —which indicates that some ICRH power is coupled directly to the SOL plasma. This conclusion is supported by observations, reported from a number of machines, of hot ions in the SOL during ICRH. These ions lead to guard limiter (and other wall component) erosion by physical sputtering, thus generating local sources of carbon and/or metal impurities, and to localized heating of plasma-facing surfaces, resulting in thermal degassing of adsorbed molecules. Such hydrogenic and impurity influxes are well correlated with ICRH power and are believed to be responsible for the observed increase in line average density and the broadening of the SOL particle flux and density profiles with total input power, $P_{tot} = P_{\Omega} + P_{ICRH}$. This broadening appears to be highly sensitive to the (limiter) surface condition, i.e., the surface concentration of hydrogen, helium, oxygen, or various metallic impurities (mainly nickel), due to helium discharges, disruptions, or high-power ICRH. As a result, density profile broadening during ICRH can be reduced significantly by wall-conditioning discharges: The cleaner the limiter surface, the narrower the observed SOL profile; indeed, profile broadening disappeared altogether in graphite belt limiter operation at higher current, although the temperature profile continued to increase with ICRH power.

For nominal surface conditions, the e-folding lengths of density and particle flux increase moderately with ICRH power, $\lambda_{\Gamma} \propto \lambda_n \propto P_{ICRH}^{0.3}$, whereas the temperature e-folding length exhibits a somewhat stronger dependence, $\lambda_{T_e} \propto P_{ICRH}^{0.5}$. This behavior is also observed in mixed (NBI + ICRH) heated discharges for which $\lambda_{\Gamma} \propto P_{tot}^{0.3}$ over a wide range of total heating power, $P_{tot} = P_{\Omega} + P_{NBI} + P_{ICRH} = 2$ to 16 MW, and plasma current, $I_p = 3$ to 5 MA; comparison of the influence of P_{NBI} and P_{ICRH} allows the observed broadening to be ascribed largely to ICRH. As expected, the power profile shows more pro-

nounced broadening than the density profile, $\lambda_q \propto P_{tot}^{0.3}$ to $P_{tot}^{0.5}$. The results may be summarized as follows:

$$\frac{\lambda_{\Gamma}^{ICRH}}{\lambda_{\Gamma}^{\Omega}} \sim L_{\parallel}^{0.2} P_{ICRH}^{0.3} \sim P_{\Omega}^{-0.17} P_{ICRH}^{0.3}$$

and

$$\frac{\lambda_{T_e}^{ICRH}}{\lambda_{T_e}^{\Omega}} \sim P_{ICRH}^{0.5}, \quad (25)$$

where $\lambda_{\Gamma}^{\Omega}$ and $\lambda_{T_e}^{\Omega}$ are given by Eq. (19). Since the sources of particles (electrons) and energy in the SOL due to ICRH are difficult to characterize, it is equally difficult to determine their influence on the mechanisms governing radial SOL transport. Although the effect of ICRH can be included in the SOL transport coefficients,

$$\frac{v_{\perp n}^{ICRH}}{v_{\perp n}^{\Omega}} \sim L_{\parallel}^{0.2} P_{ICRH}^{0.3} \sim P_{\Omega}^{-0.17} P_{ICRH}^{0.3}$$

and

$$\frac{v_{\perp T}^{ICRH}}{v_{\perp T}^{\Omega}} \propto P_{ICRH}^{0.5}, \quad (26)$$

the effect on the underlying transport mechanisms is not easily quantified. One plausible explanation would be that the subthermal component of SOL transport remains unchanged, whereas n_e and T_e profile broadening is caused by significant hydrogenic and impurity influxes and direct heating of thermal and suprathreshold electrons/ions by electromagnetic waves in front of the antenna, e.g., due to sheath rectification effects.

III.B. Beryllium Limiters

In 1989, beryllium (Be) was first evaporated on the carbon (C) belt limiters and walls, after which beryllium belt limiters were installed. The findings of these experiments, which were described in Refs. 52 and 67 and are briefly reviewed here, are of particular importance to ITER, which is planned to start up with two beryllium limiters.

Because of the effective pumping of the Be surface, strong fueling, either by gas puffing or pellet injection, was necessary to control the core density. Consequently, a larger range of densities was accessible with Be limiters than with C limiters, and the LCFS density and temperature were thereby decoupled from the line average density (Fig. 13, left). Thus, in ohmic, gas-fueled plasmas ($I_p = 3$ MA and $B_{\phi} = 3.1$ T), it was found that $n_e^{LCFS} \propto (\bar{n}_e)^2$ and $T_e^{LCFS} \propto (\bar{n}_e)^{-1}$ in the fueling phase whereas $n_e^{LCFS} \propto (\bar{n}_e)$ and $T_e^{LCFS} \propto (\bar{n}_e)^0$ in the nonfueling, i.e., wall-pumping, phase. Above some critical density, roughly $\bar{n}_e \approx 2 \times 10^{19} \text{ m}^{-3}$ for ohmic and $\bar{n}_e \approx 3 \times$

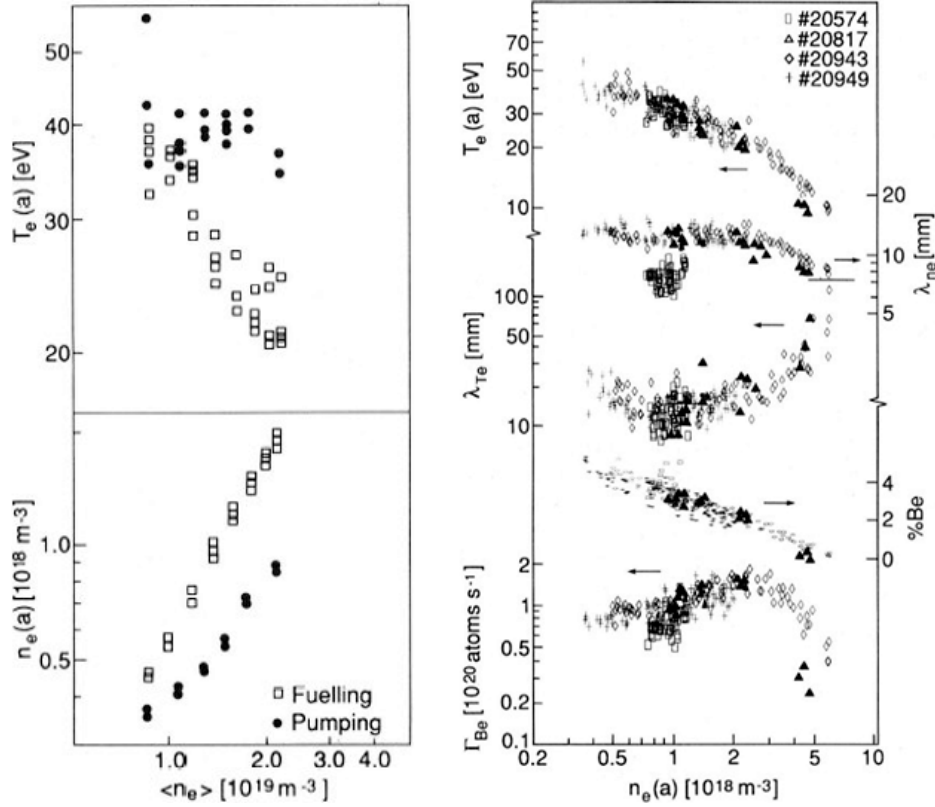


Fig. 13. Be limiter results in ohmic, gas-fueled plasmas ($I_p = 3$ MA and $B_\phi = 3.1$ T). LCFS density and temperature as a function of line average density (left) and LCFS temperature, density, and temperature e-folding lengths, SOL Be concentration, and total Be influx from limiter as a function of LCFS density (right). Reproduced with permission from Ref. 67.

10^{19} m^{-3} for L-mode discharges with $P_{\text{NBI}} = 10$ MW, the LCFS density increased, and the LCFS temperature decreased, sharply with line average density, $n_e^{\text{LCFS}} \propto (\bar{n}_e)^3$ and $T_e^{\text{LCFS}} \propto (\bar{n}_e)^{-2}$ (Fig. 14), similar to the behavior observed with carbon limiters. Power balance indicates that while the LCFS electron temperature does not exceed ≈ 40 to 60 eV, the LCFS ion temperature approaches values of several hundred eV at low density (Fig. 14); these high values are consistent with the thermal decoupling of ion and electron species at low collisionality.⁵² At high densities, $\bar{n}_e > 3 \times 10^{19} \text{ m}^{-3}$, the ion temperature decays sharply, consistent with effective ion-electron energy equipartition.

The variation of various SOL quantities as a function of LCFS density in the fueled ohmic discharges is shown in Fig. 13 (right). It is instructive that the relation between edge temperature and density, which is roughly $T_e^{\text{LCFS}} \propto (n_e^{\text{LCFS}})^{-0.5}$ at low density and $T_e^{\text{LCFS}} \propto (n_e^{\text{LCFS}})^{-1}$ at high density, is independent of the fuelling method; this critical density $\bar{n}_e \approx 2 \times 10^{19} \text{ m}^{-3}$ corresponds to $T_e^{\text{LCFS}} \sim 20$ eV. Analysis of L-mode data, in which similar results although shifted to higher densities, are obtained (compare Fig. 14), reveals that the edge temperature, and not

the density, is indeed the controlling parameter. Below this temperature, radiation in the edge/SOL region begins to strongly cool the edge/SOL plasma, producing a self-enhanced thermal instability.⁶⁸ Consistent with this effect and with the analysis of Sec. II.A, the radial e-folding lengths remain roughly constant at $\lambda_n \approx \lambda_{T_e} \approx 15$ mm for $T_e^{\text{LCFS}} > 20$ eV and increase/decrease with density as $\lambda_{T_e} \propto \lambda_n^{-1} \propto (\bar{n}_e)$ for $T_e^{\text{LCFS}} < 20$ eV; i.e., as expected, the increased electron influx makes the density profile more narrow, whereas the increased radiation broadens the temperature profile. The estimated concentration of Be atoms in the SOL decreases steadily with n_e^{LCFS} , whereas the influx of Be from the limiters increases gradually for $T_e^{\text{LCFS}} < 20$ eV, after which it decreases sharply; this behavior has been observed over a range of heating powers up to 30 MW. For $T_e^{\text{LCFS}} > 20$, the inferred particle diffusivity, calculated using Eq. (6), scales roughly linearly with the sound speed, i.e., $v_{\perp n} \propto D_{\perp} \propto (T_e^{\text{LCFS}})^{1/2} \propto c_s^{\text{LCFS}}$, in agreement with the carbon limiter result, Eq. (22). Below this critical point, it decreases sharply with temperature, $D_{\perp} \propto (T_e^{\text{LCFS}})^2 \propto c_s^{\text{LCFS}} \nu_{e,\text{LCFS}}^{*-1}$ for $T_e^{\text{LCFS}} < 20$ eV, suggesting the dominating effect of collisions. A detailed derivation of the

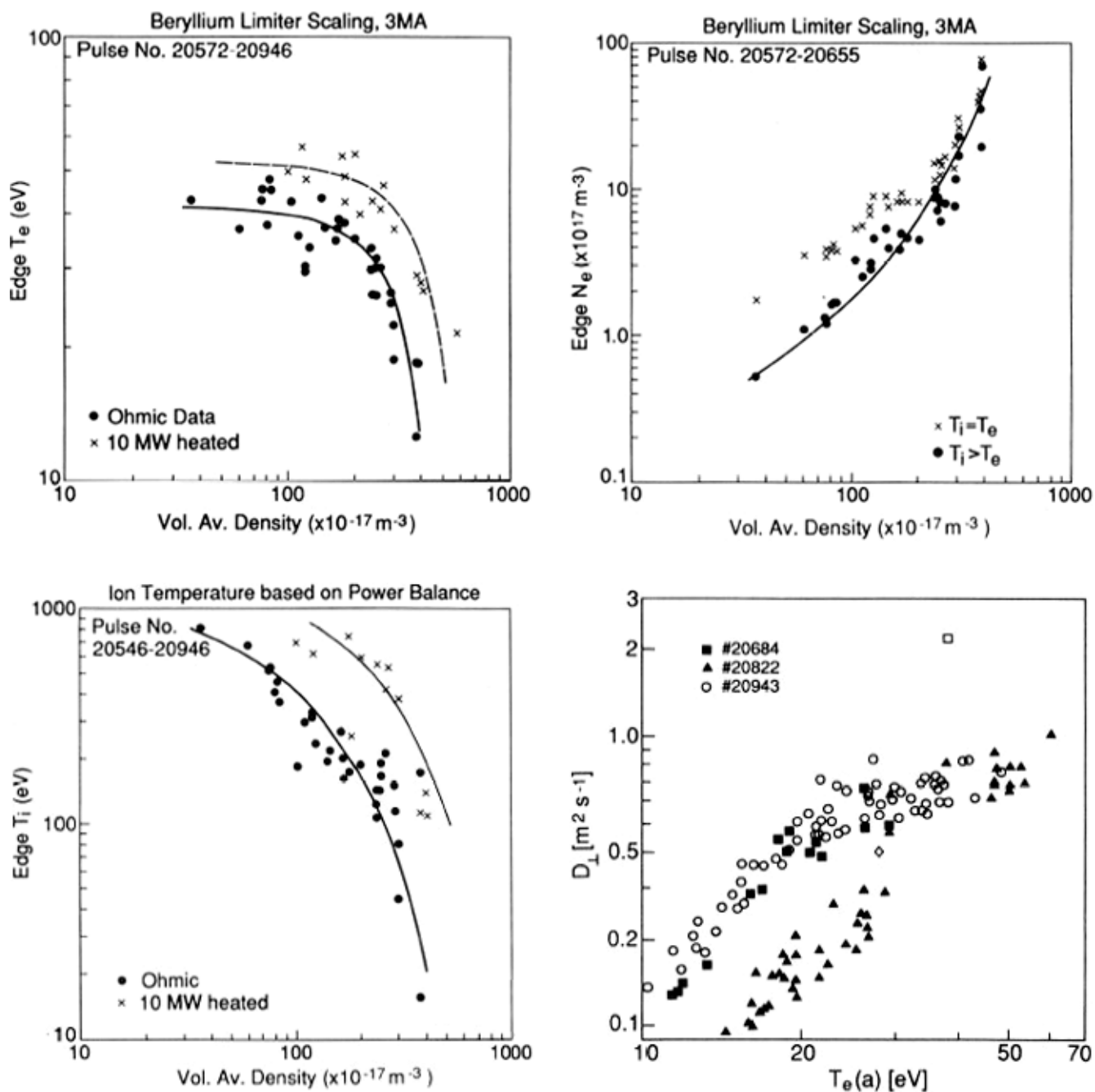


Fig. 14. Variation of n_e^{LCFS} (top left), T_e^{LCFS} (top right), and T_i^{LCFS} (bottom left) with line average density in Be limiter ohmic and L-mode (8 MW ICRH + 2 MW NBI) discharges ($I_p = 3$ MA and $B_\phi = 3.1$ T). Also shown is the inferred particle diffusivity for one ohmic (20943) and two L-mode discharges, 7 MW ICRH + 1 MW NBI (20822) and 10 MW ICRH + 9 MW NBI (20684), as a function of LCFS temperature. Reproduced with permission from Refs. 52 and 67.

particle diffusivity, and its relation to the Bohm diffusion coefficient,

$$D_{\perp}^{\text{Bohm}} = 0.66 T_e^{\text{LCFS}} / B \quad (\text{SI/eV units}), \quad (27)$$

may be found in Ref. 69.

III.C. SOL Turbulence and the H-Mode in Limiter Plasmas

Edge and SOL turbulence in JET limiter ohmic plasmas was characterized in a dedicated study using a specially designed reciprocating electrical probe, composed of several probe tips and sampled in the MHz range. The

assembly is known collectively as a turbulence probe.⁷⁰ Consistent with observations on other tokamaks, as represented schematically in Fig. 10 in Ref. 8, one finds a poloidal velocity shear layer in the edge region, roughly 1 cm, the width of a banana orbit, inside the LCFS. The floating potential and the poloidal phase velocity were found to change sign in this layer. The relative fluctuation amplitude increased with radius, whereas the turbulence flux reached a maximum at the LCFS and then decayed radially. The measured turbulent particle flux across the LCFS was consistent with the global energy confinement time of these limiter plasmas; the radial diffusivity was inferred as $D_{\perp} \sim 1.5 \text{ m}^2/\text{s}$.

We conclude our discussion of JET limiter plasmas with a mention of a recent study in which the high-confinement regime (see Sec. IV) was obtained in low field and current (0.8 T and 0.9 MA) limiter plasmas by applying significant levels (up to 7 MW) of NBI heating.⁷¹ The H-mode phases were brief (<20 ms) but clearly distinguishable due to a pronounced reduction in the edge density fluctuations and D_{α} emission and the increase of the edge density by up to 20%. The effect of the $L \rightarrow H$ transition on the density fluctuation spectrum was shown to be the same as in divertor (X -point) phases, with a quantifiable shift toward lower frequencies (<10 kHz). Although the $L \rightarrow H$ transition appears to be purely electrostatic, the $L \rightarrow H$ back-transition is accompanied by a burst of magnetic fluctuations, i.e., some type of ELM (see below).

IV. DIVERTOR SOL

As outlined in Sec. II, there are three main features that distinguish divertor from limiter SOLs:

1. the magnetic geometry, including the poloidal field X point and the magnetic shear
2. divertor plasma recycling due to localized ionization and neutral particle trapping
3. parallel gradients that develop as the SOL enters the highly collisional, conduction-limited regime and can lead to partial or total detachment of the divertor plasma.

One startling consequence of these differences is the appearance of the H-mode regime above some threshold heating power, $P_{tot} > P_{L-H}$, in which the energy confinement time roughly doubles compared to that of the low-confinement (L-mode) regime; the L-H threshold power has been found to scale as

$$P_{L-H} \approx 4.2 \times 10^{18} (\bar{n}_e)^{0.64} B_{\phi}^{0.78} A_p^{0.94}, \quad (28)$$

where \bar{n}_e is the line average density in m^{-3} , B_{ϕ} is the toroidal field in T, and A_p is the plasma surface area in m^2 (Ref. 72); i.e., the power flux crossing the LCFS

must exceed some threshold value that increases with density and toroidal field. The H-mode regime corresponds to the formation of an edge transport barrier (ETB) and its sporadic destruction by ELMs. Although the divertor geometry is not a necessary condition for accessing the H-mode, it appears to play an essential role in preventing a rapid $H \rightarrow L$ back-transition typically observed in limiter H-modes⁷¹ (see Sec. III.C); indeed the H-mode was “discovered” soon after the installation of a divertor in the Asdex tokamak,⁷³ and the two concepts (divertor and H-mode) have been closely tied ever since. It is thus natural to divide the discussion of divertor SOL transport on JET into two parts, the first dealing with ohmic and L-mode discharges, the second with H-mode discharges. In each of these sections, we consider divertors of increasing geometrical closure: Mk0 (1986 to 1992) \rightarrow MkI (1994 to 1995) \rightarrow MkIIA (1996 to 1998) \rightarrow MkIIGB (1999 to 2004), which also reflects the chronology of their installation.

The earliest divertor plasmas on JET formed the X point below/above the upper/lower dump plates, which thus played the role of horizontal divertor targets. This Mk0 divertor configuration was almost entirely open and devoid of any active (cryogenic) pumping, thus resembling the simple schematic shown in Fig. 2. However, the Mk0 divertor plasmas offered the opportunity of assessing the effect of divertor target materials on SOL profiles, since at one point the upper dump plate was made of carbon and the lower one of beryllium.

The first pumped divertor installed on JET, labeled MkI, included in-vessel coils, active cryopumping, carbon divertor targets, and toroidally tilted (fish scale) tile design; the ideas motivating the MkI divertor design are outlined in Ref. 75. The relatively open divertor structure provided little neutral compression, but MkI proved to be a useful reference for comparison with the more closed MkIIA and MkIIGB divertors that soon followed (Fig. 5). Since MkI was the first pumped divertor on JET, its effects on plasma behavior have been studied extensively. Indeed, virtually all aspects of the resulting experiments are well documented in numerous publications.^{7,76–106}

The relatively open MkI divertor was followed by the more closed MkIIA divertor, likewise with carbon targets and active pumping (Fig. 1). The new targets were arranged poloidally to better match the curved magnetic field lines, thus enhancing neutral particle trapping. Not surprisingly, the increased closure of the MkIIA structure roughly doubled the divertor neutral compression (the ratio of divertor to main chamber pressures) compared to MkI (Fig. 5) and reduced the density required for detachment by $\sim 30\%$ (Ref. 107). To increase the neutral compression even further, the toroidal gaps in the MkIIA structure were later plugged, thus reducing any bypass leaks to the main chamber. This plugged divertor, known as MkIIAP, further increased neutral trapping (Fig. 5) and reduced the density required for detachment.

The overall pumping speed was increased by roughly a factor of 3 compared to MkI (Ref. 82).

To increase divertor closure even further, the MkIIA divertor was eventually replaced by the more compact MkIIGB (gas box) design in which the inner and outer divertor chambers were separated by a vertical septum plate (Fig. 1; subsequent removal of the septum and its replacement by a horizontal metal plate revealed that it had only a minor effect on divertor, main SOL, and core plasma behavior). As in MkIIA, all target tiles were made from carbon, and cryogenic pumping was applied via corner slots between vertical and horizontal tiles. The enhanced closure of the MkIIGB structure further increased divertor neutral compression and the effective pumping speed compared to MkIIA (Fig. 5), thus allowing divertor plasma detachment at lower line average densities. The influence of puffing location on detachment in the MkIIGB configuration, as measured by plasma flux rollover, is shown in Fig. 4. The inner divertor leg detached most readily with gas injection in the inner chamber, whereas the detachment of the outer leg was only mildly sensitive to puffing location, with main chamber fueling being most effective. It is noteworthy that the increased closure of the MkIIGB divertor improved plasma purity (reduced Z_{eff}) by roughly 20% for the same value of line average density.¹⁰⁸ A good review of the influence of divertor geometry, including the sequence of Mk0-MkI-MkIIA-MkIIAP-MkIIGB, on plasma performance may be found in Ref. 3.

In a recent shutdown, the horizontal septum replacement plate was removed and replaced by a tilted, load-bearing tile made from carbon. This new tile allows higher-triangularity plasmas than were possible with the MkIIGB divertor design. Initial results were presented in Ref. 109.

IV.A. Mk0 (1986 to 1992)

The results of the Mk0 divertor experiments are reported in Refs. 58 and 74. Unfortunately, all discharges were performed at the same value of the plasma current, $I_p = 3.1$ MA, with only a small variation in the toroidal field, $B_\phi = 2.2$ to 3.4 T. Although both NBI and ICRH heating was applied, detailed scaling with P_{tot} is not reported, aside from a generic variation between ohmic, L-mode, and H-mode regimes,

$$\begin{aligned} \lambda_n^L/\lambda_n^\Omega &\approx \lambda_{T_e}^L/\lambda_{T_e}^\Omega \approx 1.4 \text{ to } 1.6 \ , \\ \lambda_\Gamma^\Omega &\approx 3 \text{ cm}, \quad \lambda_{T_e}^\Omega \approx 6 \text{ cm} \ . \end{aligned} \quad (29)$$

Indeed, only the results of the density scan with the Be target (lower single null) are reported in detail and thus are the focus of our discussion below.

Typical radial profiles of electron density in the SOL of Mk0 divertor discharges (3.0 MA and 2.8 T) are shown in Ref. 58 for three values of line average density. Under L-mode conditions, the density e-folding length in-

creased gradually with density, with typical values of $\lambda_n \approx 3$ cm. In NBI-heated L-mode discharges, λ_n was found to increase moderately with line average density,

$$\begin{aligned} n_e^{\text{LCFS}} &\propto (\bar{n}_e)^2 \ , \\ T_e^{\text{LCFS}} &\propto (\bar{n}_e)^{-0} \text{ to } (\bar{n}_e)^{-1} \ , \\ \lambda_n^{\text{LCFS}} &\propto (\bar{n}_e)^0 \text{ to } (\bar{n}_e)^1 \ , \end{aligned}$$

and

$$\lambda_{T_e}^{\text{LCFS}} \propto (\bar{n}_e)^1 \ , \quad (30)$$

with $\lambda_n \propto (\bar{n}_e)^0$ for $\bar{n}_e < 2.5 \times 10^{19} \text{ m}^{-3}$ and $\lambda_n \propto (\bar{n}_e)^1$ for $\bar{n}_e > 2.5 \times 10^{19} \text{ m}^{-3}$; note that these exponents were obtained by analyzing the figures presented in Ref. 58 and differ slightly from the ones reported in the article; e.g., the decrease of T_e^{LCFS} appears to be weaker, λ_{T_e} increases linearly rather than quadratically, and the reported break in the λ_n dependence is not immediately obvious. These results are independent of the gas-puffing location (outer midplane versus X point), although the X-point puff leads to larger parallel gradients along the SOL field lines, due to the strong pumping of the Be tiles; similar results are also found in ohmic discharges. Aside from the smaller T_e^{LCFS} reduction and more pronounced λ_n enhancement with line average density, the above scalings are similar to the ones obtained in high-density limiter plasmas, e.g., Eqs. (16) and (19). Few results are reported for Mk0 C target plasmas, the exception being the SOL density profile broadening, $\lambda_n \propto (\bar{n}_e)^{0.3}$, which is weaker than in the case of Be target plasmas, $\lambda_n \propto (\bar{n}_e)^0$ to $(\bar{n}_e)^1$, and is more reminiscent of limiter discharges (Figs. 11, 12, and 13).

The upstream H-mode profiles are much steeper at lower densities but approach the L-mode values at highest densities^{58,74}:

$$\begin{aligned} \bar{n}_e &\approx 1.4 \times 10^{19} \text{ m}^{-3} \ , \\ \lambda_{p_e}^H/\lambda_{p_e}^L &\approx 11 \text{ mm}/24 \text{ mm} \approx 0.45 \ , \end{aligned} \quad (31)$$

and

$$\begin{aligned} \bar{n}_e &\approx 2.7 \times 10^{19} \text{ m}^{-3} \ , \\ \lambda_{p_e}^H/\lambda_{p_e}^L &\approx 26 \text{ mm}/32 \text{ mm} \approx 0.8 \ . \end{aligned}$$

One may conclude that turbulent transport, which is effectively suppressed by the H-mode transition, increases with edge density and/or collisionality. This effect is independent of the puffing location (outer midplane versus X point) and/or divertor target material (C versus Be) (Refs. 58 and 74).

IV.B. MkI (1994 to 1995)

Although the vertical targets in the MkI divertor were separated by a distance comparable to the minor

radius of a typical JET plasma, it was possible to perform discharges with strike points placed on either the horizontal or vertical targets. The fueling efficiency of ohmic plasmas was nearly twice larger with vertical targets than with horizontal targets, although the density limit was not affected and corresponded to $f_{rad} \sim 0.8$, where $f_{rad} = P_{rad}/P_{tot}$ is the radiative power fraction⁷⁶; in the low-clearance (small wall gap) configuration, the density limit was reduced to $f_{rad} \sim 0.6$. The target profiles with vertical and horizontal targets are quite similar, with (partial) detachment occurring first at the magnetic strike point. Not surprisingly, the fueling efficiency was reduced as the X point was moved farther away from the target in the horizontal divertor configuration.⁷⁶ Similarly, the density corresponding to the onset of detachment, as indicated by the particle flux rollover, was reduced. Tomographic reconstructions of bolometric measurements showed that for small X-point-to-target distances, the radiative cloud moved toward and beyond the X point at $f_{rad} \sim 0.6$, whereas for larger distances it remained predominantly in the divertor SOL up to the density limit at $f_{rad} \sim 0.8$. This movement of the radiative zone, which coincides with the region of high impurity density, has been broadly reproduced by 2-D fluid modeling of detachment, including the EDGE2D/NIMBUS code,⁷ although the results are sensitive to the assumptions of radial transport and plasma-surface interaction. The key mechanism driving impurities toward the X-point region has been identified as the temperature gradient force (in contrast, the friction force tends to drive them toward the targets). During detachment, as the ionization/recombination front moves toward the X point, the net force on the impurities changes sign, leading to impurity accumulation and strong radiation in the X-point region.

Plasma detachment in the MkI divertor, which typically was observed when f_{rad} exceeded 0.7, is comprehensively reviewed in Refs. 16 and 77. The onset of detachment in typical ohmic/L-mode discharges, as measured by the “rollover” of the ion flux to the MkI divertor targets, is shown in Fig. 4. Note that the inner divertor leg not only detaches earlier than the outer leg but also exhibits a qualitatively different profile evolution. This may be inferred by considering the width of the particle flux profile at the target, which is proportional to the ratio of the integrated and peak fluxes, $\lambda_{\Gamma} \approx \int \Gamma_t dr / \Gamma_t^{\max}$. This ratio is roughly constant at the inner target but decreases by more than a factor of 2 at the outer target,

$$\begin{aligned} \text{Inner: } \lambda_{\Gamma}^{det} / \lambda_{\Gamma}^{att} &\approx 1 \quad , \\ \text{Outer: } \lambda_{\Gamma}^{det} / \lambda_{\Gamma}^{att} &\approx 0.4 \quad , \end{aligned} \quad (32)$$

where the superscripts *att* and *det* refer to the high-recycling (attached) and detached regimes. Although EDGE2D/NIMBUS modeling is able to capture the rollover behavior of the integrated flux, it does not repro-

duce the outer target broadening. To capture this effect, the radial particle diffusivity D_{\perp} , which was kept constant during the simulation, would have to increase in the outer divertor during the course of detachment, i.e., with local density, as is indeed indicated by the increased levels of fluctuations with the onset of detachment.

Temporal evolution of upstream and outer target radial profiles of n_e , T_e , and p_e in the course of a MkI L-mode density scan is shown in Fig. 7. All three profiles gradually broaden with the approach of detachment, such that

$$\lambda_{p_e}^{det} / \lambda_{p_e}^{att} \approx 22 \text{ mm} / 13 \text{ mm} \approx 1.7 \quad ,$$

$$\lambda_{T_e}^{det} / \lambda_{T_e}^{att} \approx 72 \text{ mm} / 33 \text{ mm} \approx 2.2 \quad ,$$

and

$$\lambda_{n_e}^{det} / \lambda_{n_e}^{att} \approx 42 \text{ mm} / 22 \text{ mm} \approx 1.9 \quad , \quad (33)$$

where *att* and *det* refer to attached and detached conditions. Since $p_{eu}^{det} / p_{eu}^{att} \approx (\bar{n}_{eu})^{det} / (\bar{n}_{eu})^{att} \approx 1.6$ in this discharge, one finds that λ_{p_e} increases roughly linearly with the upstream pressure and/or the line average density, $\lambda_{p_e} \propto p_{eu} \propto \bar{n}_{eu}$; here, the subscript *u* refers to the upstream value on the LCFS. In Fig. 7, the upstream and target p_e profiles in the above L-mode discharge are compared with an H-mode density scan at similar field and current. In the H-mode case, one finds that $\lambda_{p_e}^{det} / \lambda_{p_e}^{att} \approx 15 \text{ mm} / 7 \text{ mm} \approx 2.1$, which is consistent with the L-mode result, $\lambda_{p_e} \propto p_{eu}$, considering the error in the upstream pressure estimate in this discharge (see Fig. 7).

The reduced trapping of hydrogenic neutrals, that is, the reduced closure of the MkI versus the Mk0 divertor structure, was clearly observed in ohmic plasma detachment.⁷⁹ Examination of MkI divertor target profiles revealed the growth of an additional peak as the density was increased in the high-recycling regime; the disappearance of the peak was found to be concurrent with the onset of detachment.⁸⁰ A substantial part of the volumetric power, ~ 1 MW in ohmic discharges, was found to be removed by charge-exchange neutrals with energies in the range 1.5 to 3 eV (Ref. 81). The charge-exchange region, as well as the region of strong line radiation, moved toward the X point during detachment.

In reversed field discharges, i.e., with $\mathbf{B} \times \nabla B$ away from the X point, the L-mode SOL density profiles became significantly steeper when the strike point was moved from the horizontal target, $\lambda_n^{hor} \approx 3.1$ cm, to the vertical target, $\lambda_n^{ver} \approx 1.6$ cm (Ref. 84); this change was not observed, or was much smaller, in normal-field discharges, i.e., with $\mathbf{B} \times \nabla B$ toward the X point. The effect was also more pronounced at higher density, for which $\lambda_n^{ver} < \lambda_n^{hor}$ (Ref. 86). The following scalings are reported for the horizontal target under L-mode conditions:

$$\lambda_n^{hor} \propto (\bar{n}_e)^{0.5} P_{tot}^{0.25} \quad , \quad (\bar{n}_e)^{0.4} P_{tot}^{0.75} \quad (34)$$

and

$$\lambda_{p_e}^{hor} \propto (\bar{n}_e) , \quad (\bar{n}_e)^{0.75} P_{tot} , \quad (35)$$

with the first expressions for $P_{tot} < 4$ MW and the second for $P_{tot} \approx 4$ to 8 MW; for the vertical target under L-mode conditions, the e-folding length was independent of density, $\lambda_n^{ver} \propto (\bar{n}_e)^0$ (Refs. 87 and 88). Note that the increase of λ_n with \bar{n}_e is indicative of (the approach to) plasma detachment, as predicted by 2-D fluid/neutral codes (see below) and observed experimentally in the MkI divertor (Fig. 7).

These results emphasize the importance of neutral recycling on upstream density profiles as highlighted in Ref. 15 and illustrated schematically in Fig. 3. They are also consistent with the complex SOL expression, Eq. (10), and with the picture of the influence of sources on radial profiles discussed in Sec. II.A. This picture may be summarized as follows: Since, on average, the recombining neutrals leave the divertor target in a direction normal to its surface, they tend to travel away/toward the separatrix in horizontal/vertical divertor configurations and thus ionize in the far/near SOL in these two cases, the far-SOL plasma being relatively cold and dilute compared to that in the near SOL. In the vertical divertor case, the near-SOL flux tubes can thus become overionized; i.e., the particle source can exceed the local sink to the target, producing a backflow toward the upstream region. Such flow reversal, as the effect is generally known, tends to increase the radial density gradient and thus decrease λ_n^{ver} compared to λ_n^{hor} , in agreement with experiment. Unfortunately, since the role of neutral sources is comparable to that of radial transport, a detailed, quantitative analysis requires 2-D coupled plasma-neutral codes; it is thus reassuring that numerical modeling performed using the EDGE2D/NIMBUS code confirmed this picture and reproduced the experimental data reasonably well.^{88,89}

The scalings of λ_n and λ_{T_e} with various plasma and field parameters in JET MkI divertor ohmic and L-mode discharges are discussed in Ref. 90, together with data from other large tokamaks. In the high-recycling (conduction-limited) regime, the following scalings are reported for JET MkI discharges:

$$\lambda_n^{LCFS} \propto (\bar{n}_e/n_{GW})^{0.42} q_{95}^{0.37} P_{tot}^{0.29} \quad (36)$$

and

$$\lambda_{T_e}^{LCFS} \propto (T_e^{LCFS})^{-1.34} q_{95}^{0.39} P_{tot}^{0.46} , \quad (37)$$

where n_{GW} is the Greenwald density,¹¹⁰

$$n_{GW} = 10^{14} \frac{I_p}{\pi a^2} \text{ (SI units)} . \quad (38)$$

The λ_n expression is broadly consistent with Eq. (34). In the λ_{T_e} scaling, the reduction with T_e^{LCFS} is partly offset

by the increase with the heating power. Since the two parameters are generally related, this scaling appears to contain a degree of redundancy, which we discuss in the following section. In the low-recycling (sheath-limited) regime, JET MkI data are discussed only as part of the multimachine scaling, which indicates that, roughly speaking,

$$\lambda_n^{LCFS}, \lambda_{T_e}^{LCFS} \propto (A_p/I_p)^{0.7} \quad (39)$$

across many machines.

The radial heat diffusivity in the SOL, inferred from Eq. (8), ranged between 0.1 and 0.6 m²/s in the MkI divertor experiments and increased roughly linearly with total heating power.⁸⁶ These values were confirmed based on modeling using both the onion skin method⁹² (OSM) and the EDGE2D/NIMBUS code,⁷ which suggested $D_{\perp} \approx 0.1$ m²/s and $\chi_{\perp} \approx 0.5$ m²/s in L-mode discharges (H-mode values were a factor of 2 lower); note that this value of D_{\perp} is at least an order of magnitude smaller than the Bohm diffusivity, Eq. (27). The OSM-extracted radial profiles of χ_{\perp} suggest a reduction of the diffusivity with the heating power, $\chi_{\perp} \propto P_{tot}^{-1}$, and a gradual increase of χ_{\perp} away from the LCFS, consistent with a flattening of the SOL power profiles,⁹¹ i.e., the increase of λ_q away from the LCFS, as can be seen directly in Fig. 7. EDGE2D/NIMBUS simulations⁷ indicate that the flattening of the temperature profile can largely be explained by the reduction of parallel electron conduction at lower temperatures (Sec. II.C). The effect of the $L \rightarrow H$ transition on MkI divertor detachment is investigated in Ref. 16, where detachment in three types of ELMy H-mode plasmas are considered: (a) unfueled, natural density, (b) deuterium fueled with Type-I ELMs, and (c) nitrogen seeded with Type-III ELMs. In the D_2 fueled case, the divertor plasma only detaches in the inter-ELM phase and promptly reattaches during the ELMs; i.e., the ELMs carry sufficient energy to burn through the cloud of neutrals/impurities at the detachment front and reestablish fully ionized plasma contact with the target plate, Fig. 16, MkI ELMy H-mode detachment. In contrast, nitrogen seeded H-modes, in which the ELMs are substantially smaller, allow the plasma to remain detached at all times. The seeded nitrogen tends to accumulate in the divertor during detachment, yielding enrichment factors of 30 or more.⁷⁻⁹

As mentioned previously and illustrated in Fig. 7, the upstream pressure profile during H-mode conditions gradually broadens with the approach of detachment. Although the degree of broadening is consistent with that observed under L-mode conditions, which is roughly linear with the upstream pressure, $\lambda_{p_e} \propto p_{eu}$, Eq. (33), the inter-ELM H-mode profiles are narrower than the corresponding L-mode profiles and tend to converge with increasing density,

$$\text{Attached: } \lambda_{p_e}^H / \lambda_{p_e}^L \approx 7 \text{ mm} / 13 \text{ mm} \approx 0.55$$

and

$$\text{Detached: } \lambda_{p_e}^H / \lambda_{p_e}^L \approx 15 \text{ mm} / 22 \text{ mm} \approx 0.7, \quad (40)$$

in line with the Mk0 result, Eq. (31).

IV.C. MkIIA (1996 to 1998)

Although changing the strike point location from horizontal to vertical targets in MkIIA did not affect the divertor neutral pressure, it increased the density limit by $\sim 10\%$, suggesting that the fueling efficiency was slightly reduced. Whereas in the MkI divertor, detachment of the inner and outer divertor legs occurred at similar densities, in MkIIA the inner divertor leg detached much earlier when the strike points were located on the horizontal targets and at roughly the same density as the outer leg when they were placed on the vertical targets.¹⁰⁷ The approach to detachment was also much more gradual in the vertical divertor configuration. All of these changes can be ascribed to differences in the ionization and recycling patterns, as shown in Fig. 3 and discussed in Secs. II.A and IV.B. MkIIA divertor studies also established a clear link between the onset of detachment and volumetric recombination, which was detected based on spectroscopic line ratios and was found to be concentrated near the strike points at both divertor targets. This observation implied that plasma temperature dropped below 1 eV at the targets following detachment. As with the MkI divertor, the radiation cloud was seen to move to the X-point region, where in ohmic and L-mode discharges, recombination was also detected. Despite the lower upstream neutral pressure with MkIIA and MkIIAP divertors, the level of impurities in the core plasma was not affected; i.e., Z_{eff} remained unchanged from the MkI scaling.

Similar to the MkI study, the divertor target n_e and T_e profiles were measured across the MkIIA divertor target with an array of Langmuir probes in a large number of ohmic, L-mode, and H-mode discharges of varying I_p , B_ϕ , q_{95} , P_{tot} , and \bar{n}_e (Ref. 111; see Fig. 15); in all cases the SOL plasmas were attached and ranged over both sheath-limited and conduction-limited regimes. A two-point onion skin method was then used to map these profiles to the upstream SOL and to calculate the resulting radial e-folding lengths and heat diffusivity profiles (Fig. 17). The OSM method was validated based on a limited number of (MkI) discharges for which the upstream profiles were measured directly with the reciprocating probe and Li beam diagnostic, and which were found to be in fair agreement with the OSM predictions.⁹¹ The complete MkI + MkIIA database included more than 40 discharges, two dozen of which are compiled in Table I of Ref. 111. Under ohmic and L-mode conditions, the resulting e-folding lengths fall in the range $\lambda_n^{\text{LCFS}} \approx 5$ to 40 mm and $\lambda_{T_e}^{\text{LCFS}} \approx 7$ to 60 mm, generally increasing away from the separatrix (Fig. 17). Such pro-

file broadening in the far SOL, which is more pronounced for λ_{T_e} than for λ_n , is consistent with earlier observations in MkI discharges (Fig. 7). Comparison of discharges with vertical versus horizontal targets and with low versus high flux expansion revealed no clear differences in upstream SOL profiles, suggesting that main SOL transport is largely independent of the degree of divertor closure.

In Ref. 111 it is concluded that the near-SOL e-folding lengths λ_n^{LCFS} and $\lambda_{T_e}^{\text{LCFS}}$ are not correlated with any single main plasma parameter. Nonetheless, a multivariable regression analysis of these lengths with B_ϕ , q_{95} , P_{SOL} , and \bar{n}_e (note that $P_{\text{SOL}} = P_{\text{tot}} - P_{\text{rad}}$ and $I_p \propto B_\phi / q_{95}$ are decoupled in L-mode discharges due to the presence of auxiliary heating) yields close agreement between the experimental values and the following relations:

$$\lambda_n^{\text{LCFS}} \propto B_\phi^{-0.8} q_{95}^{1.3} (\bar{n}_e)^{0.1} P_{\text{SOL}}^{-0.4} \quad (41)$$

and

$$\lambda_{T_e}^{\text{LCFS}} \propto B_\phi^{-0.8} q_{95}^{1.3} (\bar{n}_e)^{0.7} P_{\text{SOL}}^{-0.5}, \quad (42)$$

or repeating the regression with \bar{n}_e and P_{SOL} replaced by n_e^{LCFS} and T_e^{LCFS} ,

$$\begin{aligned} \lambda_n^{\text{LCFS}} &\propto B_\phi^{-0.8} q_{95}^{1.3} (n_e^{\text{LCFS}})^{0.5} (T_e^{\text{LCFS}})^{-1.2} \\ &\sim L_{\parallel} (\nu_e^* \text{LCFS})^{1/2} \end{aligned} \quad (43)$$

and

$$\begin{aligned} \lambda_{T_e}^{\text{LCFS}} &\propto B_\phi^{-0.8} q_{95}^{1.3} (n_e^{\text{LCFS}})^{0.8} (T_e^{\text{LCFS}})^{-1.4} \\ &\sim L_{\parallel} (\nu_e^* \text{LCFS})^{1/2}, \end{aligned} \quad (44)$$

with correlation factors > 0.8 . The inverse scaling with I_p —note that for constant magnetic field, $q_{95}^{1.3} \propto I_p^{-1.3}$, in agreement with Eq. (19)—and the positive scaling with \bar{n}_e are similar to the limiter results of Eq. (19), but the inverse scaling with P_{SOL} is contrary to the results reported earlier with the MkI divertor [see Eq. (34)]. It is not clear whether this is due to actual differences between MkI and MkIIA discharges or to the approximate nature of OSM modeling, the absence of current and field scaling in Eq. (34), or some other, unknown factors, e.g., the uncertainty in the separatrix location. It is worth noting that $\lambda_{T_e}^{\text{LCFS}}$ scales inversely with T_e^{LCFS} across all plasma regimes, including inter-ELM H-mode. This dependence, which can be approximated as $\lambda_{T_e} T_e \sim \text{constant}$, is consistent with the broadening of the SOL temperature profile with radial distance away from the LCFS (Fig. 17).

Combining Eqs. (43) and (8), one obtains the effective radial velocity

$$\begin{aligned} v_{\perp n_e}^{\text{LCFS}} &\propto L_{\parallel}^{0.3} (n_e^{\text{LCFS}})^{0.5} (T_e^{\text{LCFS}})^{-0.8} \\ &\sim (\nu_e^* \text{LCFS})^{1/2}, \end{aligned} \quad (45)$$

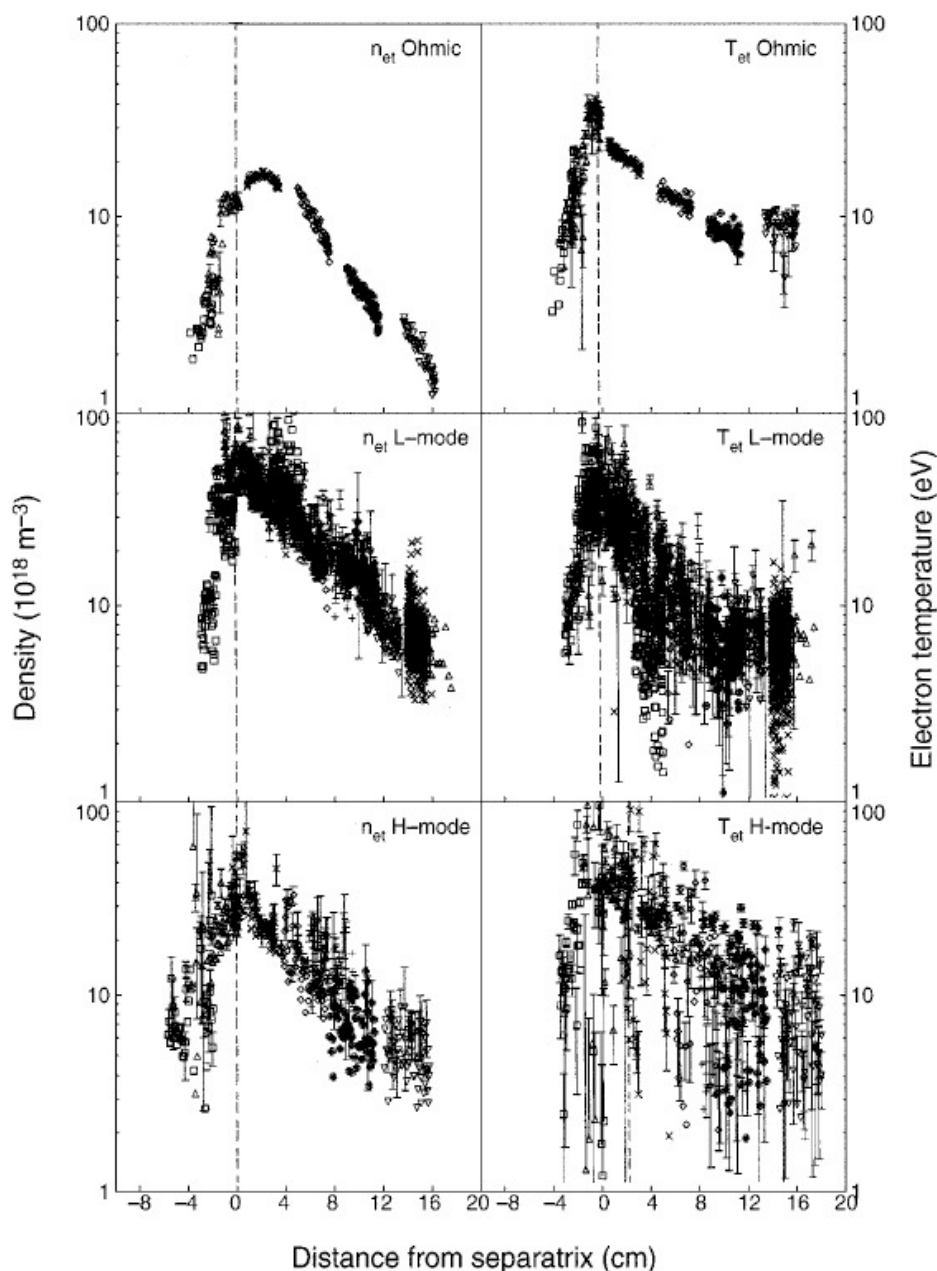


Fig. 15. Radial profiles of electron density and temperature at the MkIIA divertor outer target in ohmic, L-mode, and H-mode discharges. Note the increase in the fluctuation levels of both n_e and T_e with the heating power. Reproduced with permission from Ref. 111.

which is found to increase roughly with the square root of the collisionality. This divertor (conduction-limited) result differs substantially from the limiter (sheath-limited) result, Eq. (22), where $v_{\perp ne}^{\text{LCFS}}$ was found to be independent of v_e^{LCFS} and directly proportional to c_s^{LCFS} . Similarly, the heat diffusivity derived using OSM modeling increases linearly with collisionality, $\chi_{\perp}^{\text{LCFS}} \propto (T_e^{\text{LCFS}})^{-2} \propto v_e^{\text{LCFS}}$, with typical near-SOL values in the range of 0.03 to 0.3 m²/s (Fig. 17). Once again, these

values are somewhat larger than the earlier results, which indicate $\chi_{\perp}^{\text{LCFS}} \sim 0.2$ to 1 m²/s in ohmic and L-mode discharges.

The absolute values of $v_{\perp n}^{\text{LCFS}}$ derived using Eq. (8), which are found to vary between 10 and 30 m/s, are in good agreement with typical radial effective velocities measured by the turbulence probe in ohmic MkIIA plasmas¹¹²; these values are consistent with diffusion coefficients of ~ 0.15 to 0.3 m²/s. This direct measurement

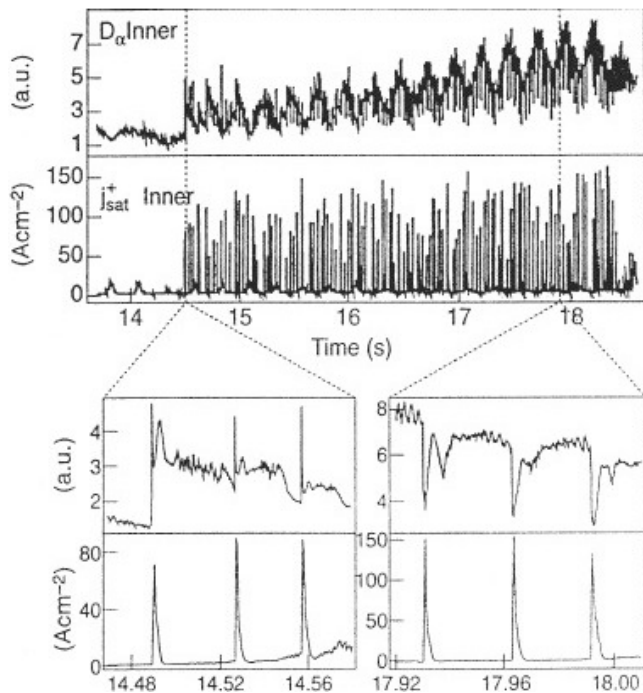


Fig. 16. Inner divertor D_α and $j_{sat} = \Gamma_t/e$ for an ELMy H-mode density scan in the MkI divertor with Be targets; note that ELM frequency generally increases, and hence ELM size decreases with gas puffing and line average density. At the lowest densities (left), the divertor plasma is attached at all times, such that both D_α and j_{sat} increase during ELMs. In contrast, at the highest densities (right), it detaches in the inter-ELM period, reattaching briefly during the ELM, such that j_{sat} increases but D_α decreases during the ELM. This effect is sometimes referred to as a negative ELM. Note that Be emission remains negligible at all times, implying a low (<10 eV) electron temperature even during the ELM. Reproduced with permission from Ref. 16.

indicates that $v_{\perp n}$ is substantially smaller in the divertor (X-point) phase compared to the limiter phase of the same discharge and is insensitive to the divertor configuration (horizontal versus vertical). The difference between limiter and divertor SOL is mainly due to higher density fluctuation levels in the limiter SOL, and to a lesser extent to increased correlation between density and potential fluctuations.¹¹² One also observes that $v_{\perp n}$ decays gradually with radius in the limiter far SOL but remains roughly constant across the divertor far SOL; it is not possible to comment on the near-SOL region since the exact position of the separatrix is not known in the X-point phase. The constancy of $v_{\perp n}$ with radius suggests that Eq. (45) remains applicable across the SOL, since n_e often decreases faster than T_e , thus keeping the collisionality roughly constant (see Sec. IV.D).

The variation of both pedestal and separatrix densities, normalized by the line average density with ELM

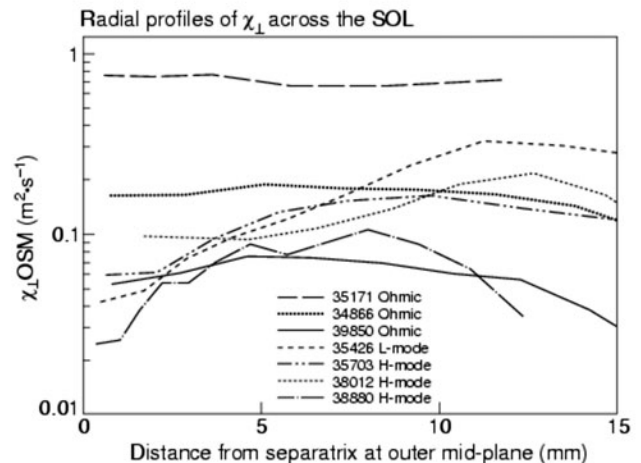
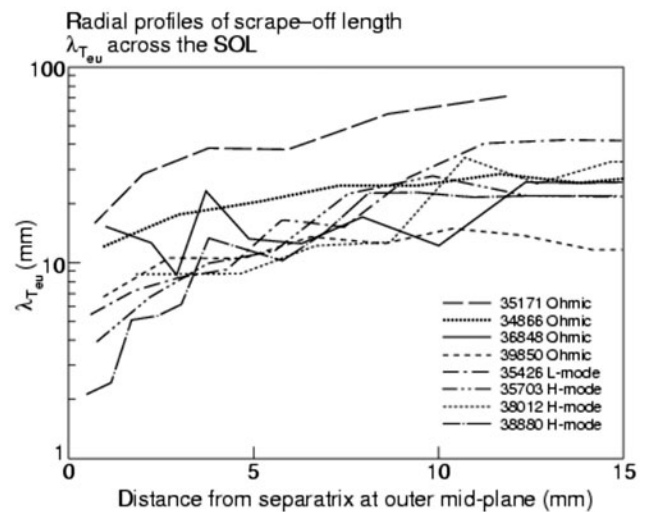
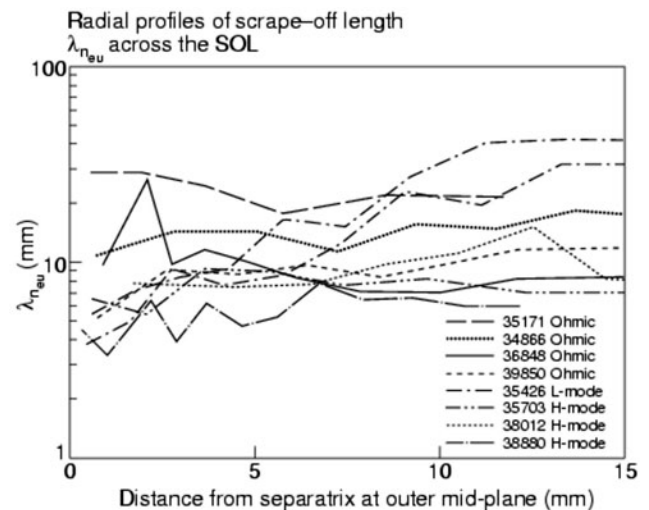


Fig. 17. Radial profiles of density and temperature e-folding lengths and radial heat diffusivities in MkI (<36000) and MkIIA (>36000) divertor ohmic, L-mode, and H-mode discharges extracted from target profiles of density and electron temperature using the onion skin method. Reproduced with permission from Ref. 111.

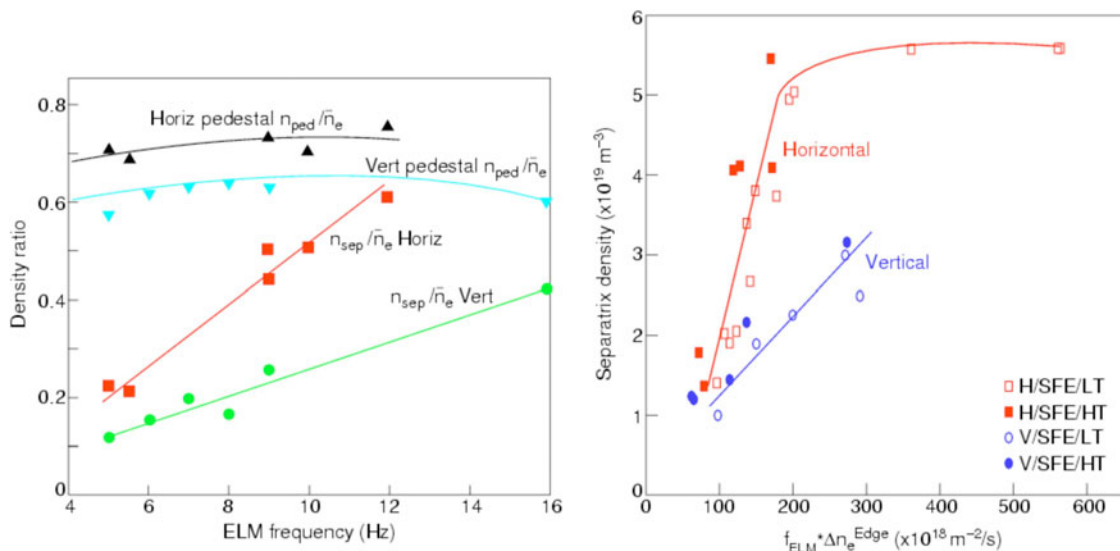


Fig. 18. The variation of pedestal and separatrix densities, normalized by the line average density, with ELM frequency (left) and of the separatrix density with the rate of particle loss due to ELMs (right) in MkIIA ELMY H-mode plasmas. The plots compare data from low-triangularity (LT) plasmas with data from high triangularity (HT) plasmas with horizontal and vertical target divertor configurations. Reproduced with permission from Refs. 82 and 113.

frequency, f_{ELM} , is shown in Fig. 18. Whereas n_e^{ped}/\bar{n}_e was clearly independent of f_{ELM} , n_e^{LCFS}/\bar{n}_e was found to increase linearly with f_{ELM} , from 0.1 to 0.2 at 5 Hz to 0.4 to 0.6 at 15 Hz; this scaling is consistent with the ohmic and L-mode dependence (Fig. 20) in that f_{ELM} generally increased with \bar{n}_e . The constant of proportionality, $C = n_e^{LCFS}/\bar{n}_e f_{ELM}$, was larger with horizontal targets than with vertical targets and with high plasma triangularity than with low plasma triangularity.¹¹³ The latter dependence could be eliminated by replotting n_e^{LCFS} versus the rate of particle loss due to ELMs, $f_{ELM} \Delta n_e^{ped}$ (Fig. 18), suggesting a correlation between triangularity and the ELM frequency. The remaining difference between vertical and horizontal targets can be ascribed to the difference in neutral compression and recycling patterns in these two configurations. Energy confinement degradation was likewise related to the ELM frequency, or more accurately to the product $f_{ELM} \tau_{ped} = \tau_{ped}/\tau_{inter-ELM} \equiv \xi_{ELM}$, where τ_{ped} is representative of the time taken to reheat the edge plasma following an ELM, i.e., to rebuild the H-mode pedestal. The $H97$ confinement factor (corrected for fast ions) was well reproduced by the following expression:

$$H97 = 1.23 - 0.57 \xi_{ELM} [1 - \exp(-1/\xi_{ELM})], \quad (46)$$

where $\tau_{ped} \approx 34$ ms was inferred from the experimental data. MkIIA results also showed that confinement degradation is better correlated with the ELM frequency, and hence with the upstream LCFS density, than with the upstream neutral pressure, as was postulated based on MkI data. In other words, $H97$ decreased monotonically

with n_e^{LCFS}/\bar{n}_e , with $H97 \approx (1.0, 0.9, 0.8, \text{ and } 0.7)$ for $n_e^{LCFS}/\bar{n}_e = (0.1, 0.5, 0.7, \text{ and } 0.8)$.

IV.D. MkiIGB (1999 to 2004)

The MkI + MkIIA database discussed in Sec. IV.C was extended by a further two dozen n_e and T_e target profiles in the MkiIGB divertor, all but one of these in ohmic and L-mode plasmas under attached conditions. As before, a two-point OSM method was used to map the target profiles to the upstream SOL. For selected cases, this technique was also compared against an advanced OSM method in which the parallel transport equations were solved by computational fluid dynamic techniques between the target and upstream regions.^{114–116} Although the absolute values differed by up to a factor of 2 between the two techniques, the upstream e-folding lengths agreed reasonably well. The advanced OSM method was further validated against the upstream n_e and T_e profiles measured using the reciprocating probe in selected MkiIGB L-mode discharges (Fig. 19). Note that the inferred heat diffusivity profiles tend to increase away from the separatrix, with $\chi_{\perp} \approx 0.1$ to $0.2 \text{ m}^2/\text{s}$ in the near SOL to $\chi_{\perp} \approx 0.4$ to $0.6 \text{ m}^2/\text{s}$ in the far-SOL regions, consistent with earlier results (Fig. 17), and with the broadening of the $T_e(r)$ profile.

The complete MkiIGB database is summarized in Table 2 of Ref. 117, with the most notable results presented in Fig. 20. It is interesting to note that the upstream separatrix density and temperature across many discharges appear to be related as $n_{eu}^{LCFS} \propto (T_{eu}^{LCFS})^2$,

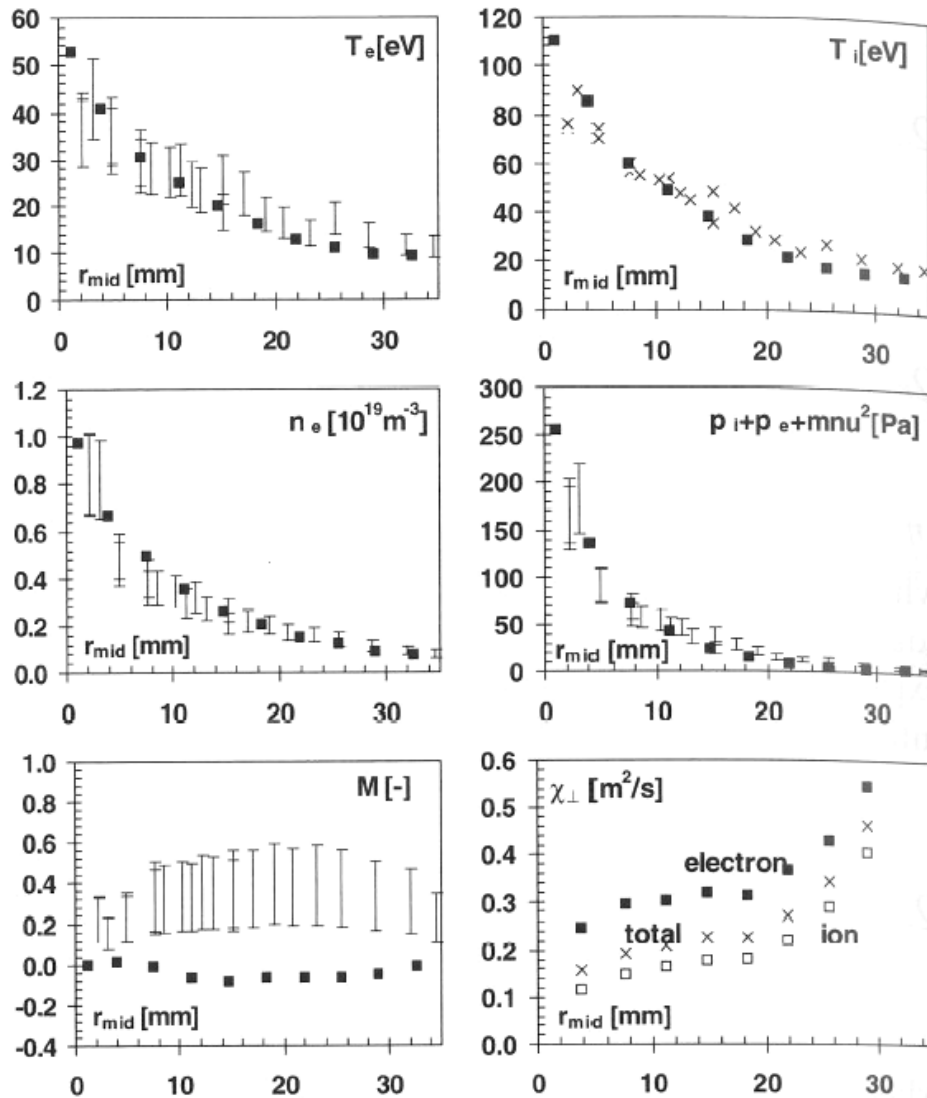


Fig. 19. Comparison of radial profiles of upstream electron and ion temperatures, electron density, total pressure, and parallel Mach number computed using an advanced OSM solver based on target profiles and measured directly by a reciprocating probe in an MkiIGB L-mode discharge. Also shown are the radial heat diffusivity profiles inferred by the OSM method, which are seen to increase radially away from the separatrix. Reproduced with permission from Ref. 114.

albeit with a large scatter. Moreover, the same dependence appears to hold approximately across the SOL for upstream profiles in any given discharge, i.e., $n_{eu} \propto T_{eu}^2$ (Fig. 20). Since $L_{||} \approx \pi R q_{95}$ has only a small variation across discharges and varies by less than a factor of 2 across the SOL, these relations imply that the upstream collisionality remains bounded roughly by $20 < \nu_{eu}^* < 80$ across the entire MkiIGB database (Fig. 20). The approximate constancy of ν_{eu}^* across many discharges can be attributed to the fact that only high-recycling-regime plasmas were selected, which from the discussion in Sec. II.C, implies that $10 < \nu_e^* < 100$. The constancy of ν_e^* radially across the SOL is more difficult to explain; we return to this observation later. Finally, the ratio of the upstream

and line average densities increases from ~ 0.2 for lowest densities to ~ 0.8 for highest densities (Fig. 20).

The magnitudes of upstream e-folding lengths are somewhat smaller in MkiIGB than in the Mki + MkiIA database: $\lambda_n^{LCFS} \approx 5$ to 30 mm and $\lambda_{T_e}^{LCFS} \approx 8$ to 40 mm. This might be ascribed to the fact that virtually all the Mki + MkiIA data were obtained in the horizontal divertor configuration, whereas the MkiIGB results were obtained in the vertical configuration, in which the divertor recycling pattern becomes more important and tends to produce somewhat narrower SOL widths. More important, the MkiIGB lengths are only weakly correlated with the Mki + MkiIA scalings, Eqs. (41) through (44). Indeed, the MkiIGB data exhibit a significantly

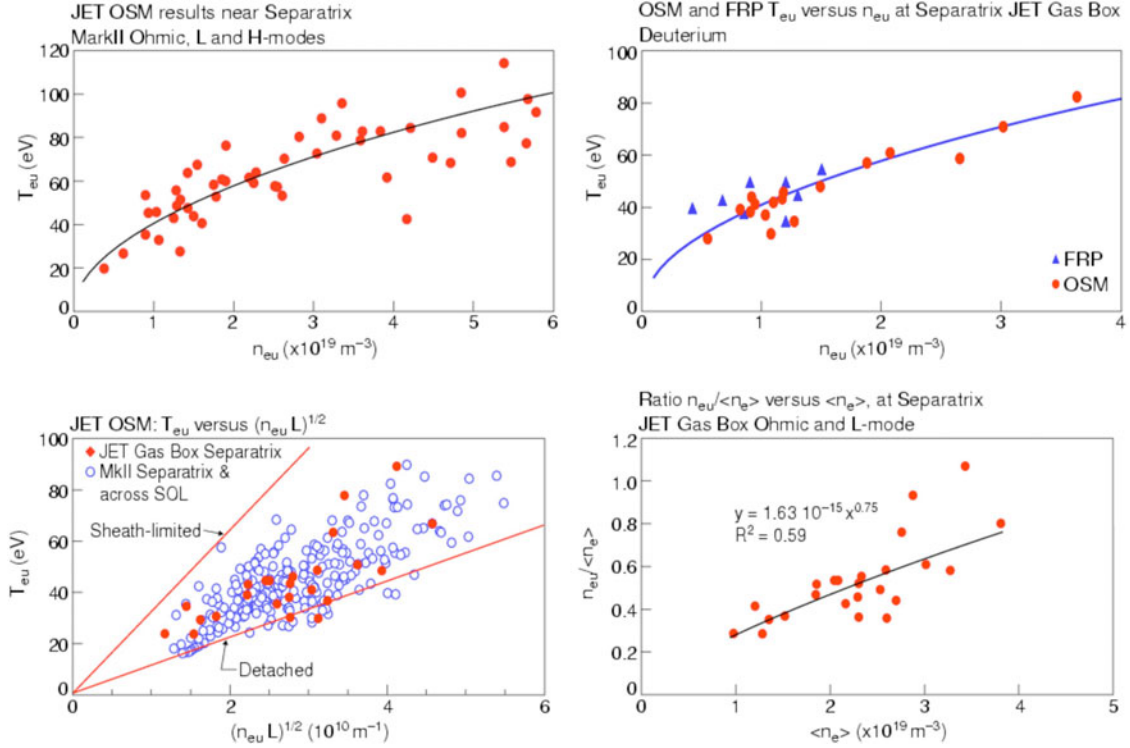


Fig. 20. Relation between OSM-derived upstream density and temperature in MkIIA ohmic, L-mode, and H-mode plasmas (upper left). Similar relation for MkIIIGB, including several reciprocating probe measurements (upper right). Collisionality diagram for MkIIA and MkIIIGB points (bottom left); all data fall in the conduction-limited regime, i.e., are bounded by straight lines indicating $\nu_e^* = 10$ sheath-limited and $\nu_e^* = 80$ detached regimes. Ratio of upstream to line average density (bottom right). Reproduced with permission from Refs. 117 and 118.

larger scatter than the MkI + MkII data, such that even the best fit for λ_n^{LCFS} and $\lambda_{T_e}^{\text{LCFS}}$ yields correlation factors of less than 0.4. The origin of this scatter is not clear and strongly suggests some hidden variable. One possible cause is the approach to divertor detachment, which occurs for lower upstream densities with vertical, rather than with horizontal, targets. Since the two-point OSM method is not applicable for detached plasmas, it might produce significant errors in the presence of vertical targets. This should be kept in mind when reviewing the MkIIIGB results discussed here.

Roughly speaking, both e-folding lengths were found to be inversely proportional to upstream quantities,

$$\lambda_n^{\text{LCFS}} \propto (T_e^{\text{LCFS}})^{-0.85} \propto (n_e^{\text{LCFS}})^{-0.38} \quad (47)$$

and

$$\lambda_{T_e}^{\text{LCFS}} \propto (T_e^{\text{LCFS}})^{-0.65} \propto (n_e^{\text{LCFS}})^{-0.45} . \quad (48)$$

Consequently, the power e-folding length and the inferred heat diffusivity tend to decrease with both the upstream density, $\chi_{\perp}^{\text{LCFS}} \propto (n_e^{\text{LCFS}})^{-1.25}$, and the power into the SOL, $\chi_{\perp}^{\text{LCFS}} \propto P_{\text{SOL}}^{-1.07}$. The following scalings,

$$\lambda_q^{\text{LCFS}}/L_{\parallel} \propto P_{\text{SOL}}(n_e^{\text{LCFS}})^{-1.2} \quad (49)$$

and

$$\chi_{\perp}^{\text{LCFS}} \propto (P_{\text{SOL}} L_{\parallel})^2 (n_e^{\text{LCFS}})^{-2.7} , \quad (50)$$

give a reasonable fit to the MkIIIGB ohmic and L-mode results, provided these are plotted on a logarithmic scale, such that the inherent scatter in the data is reduced; note the appearance of the anticipated $\chi_{\perp} \propto L_{\parallel}^2 \propto q_{95}^2$ scaling in Eq. (50). The above relations, with the factor 1.2 replaced by $\frac{7}{4} = 1.75$ and 2.7 replaced by $\frac{13}{4} = 3.25$, can be derived for the conduction-limited regime from Eq. (7) by estimating the power into the SOL as $P_{\text{SOL}} L_{\parallel} \propto q_{\parallel} \lambda_q$. This leads to the estimate of the upstream temperature,

$$T_{eu} \propto (P_{\text{SOL}} L_{\parallel})^{4/9} (n_e^{\text{LCFS}} \chi_{\perp}^{\text{LCFS}})^{-2/9} , \quad (51)$$

and the following relations between $\chi_{\perp}^{\text{LCFS}}$ and $\lambda_{T_e}^{\text{LCFS}} \sim \lambda_q^{\text{LCFS}}$:

$$\begin{aligned} \lambda_q^{\text{LCFS}}/L_{\parallel} &\propto (P_{\text{SOL}} L_{\parallel})^{-5/9} (n_e^{\text{LCFS}} \chi_{\perp}^{\text{LCFS}})^{7/9} \\ &\propto (T_e^{\text{LCFS}})^{-5/4} (n_e^{\text{LCFS}} \chi_{\perp}^{\text{LCFS}})^{1/2} . \end{aligned} \quad (52)$$

Good accounts of the derivation may be found in Ref. 117 and Chap. 65 of Ref. 13.

One of the main conclusions emerging from the above studies is the close relationship between the density and temperature e-folding lengths, with $\lambda_n/\lambda_{T_e} \sim 1$. To see this more clearly, consider the density and temperature profiles for MkiIGB ohmic plasma at three different densities, obtained simultaneously from a variety of diagnostics (see Figs. 3 and 9 in Ref. 20). Here, the density was measured by two reciprocating Langmuir probes separated toroidally by 180 deg, as well as a lithium beam and edge LIDAR diagnostics.²⁰ The temperature was inferred from the floating potential–temperature relation for a Langmuir probe.²⁰ One observes a gradual broadening of the $T_e(r)$ profile, with λ_{T_e} increasing gradually with distance away from the separatrix, from ~ 10 to 20 mm in the near SOL to >50 mm in the far SOL. In contrast, the $n(r)$ profile is characterized by a single e-folding length, $\lambda_n \approx 15$ to 25 mm, roughly constant across the SOL. One thus finds $\lambda_n/\lambda_{T_e} > 1$ in the near-SOL and $\lambda_n/\lambda_{T_e} < 1$ in the far-SOL regions.

It is not immediately obvious why the two lengths should be comparable in a complex SOL, where the sources of particles and energy are clearly decoupled. A simple explanation may be obtained from taking the ratio of Eqs. (6) and (7). Assuming radially advective transport with $v_{\perp n} \approx v_{\perp T} \approx v_{\perp}$ representing the effective radial velocity of turbulent filaments or blobs, the ratio λ_n/λ_{T_e} reduces to the ratio of parallel loss times of particles and electron energy,

$$\frac{\lambda_n}{\lambda_{T_e}} \approx \frac{\tau_{\parallel n}}{\tau_{\parallel T}} \approx \frac{\chi_{\parallel e}}{c_s L_{\parallel}} \approx \frac{v_{te}}{v_{ti}} \frac{\lambda_{ei}}{L_{\parallel}} \approx \left(\frac{T_e m_i}{T_i m_e} \right)^{1/2} \frac{1}{\nu_e^*} \approx \frac{60}{\nu_e^*}, \quad (53)$$

where we neglected factors of order unity and evaluated the final expression for a deuterium plasma with equal ion and electron temperatures. Although Eq. (53) neglects several important effects, e.g., ion-electron energy collisional exchange, which tends to couple λ_{T_e} and λ_{T_i} , it clearly illustrates why $\lambda_n/\lambda_{T_e} \sim 1$ in the conduction-limited regime for MkiIGB SOL, for which typically $\nu_e^* \sim 40$ to 80 (Fig. 20). Note that Eq. (53) predicts a linear decrease of λ_n/λ_{T_e} with ν_e^* , such that $\lambda_n/\lambda_{T_e} \gg 1$ for $\nu_e^* \ll 60$ and $\lambda_n/\lambda_{T_e} \ll 1$ for $\nu_e^* \gg 60$. Similar arguments, but based on the diffusive rather than the advective assumption, may be found in Ref. 118 and Chap. 5 of Ref. 13.

SOL turbulence studies were actively pursued in MkiIGB divertor plasmas and are described in several articles.^{122–138} As with the MkiIA divertor, a turbulence probe was used to measure the radial $\mathbf{E} \times \mathbf{B}$ particle flux profiles in MkiIGB ohmic, L-mode, and H-mode discharges.¹²⁰ In the ohmic plasma investigated, the effective radial velocity and particle diffusivity remained

constant across the SOL, with $v_{\perp n} \approx 100$ m/s and $D_{\perp} \approx 0.7$ m²/s. Although these values are a factor of 3 larger than those measured in MkiIA ohmic plasmas, one should keep in mind that they correspond to lower field, current, and density. However, the observation that $v_{\perp n} \sim$ constant is consistent with the $v_{\perp n} \propto \nu_e^{*1/2}$ scaling, Eq. (45), and the approximate constancy of ν_e^* across the SOL. The L-mode results indicate that $v_{\perp n}$ is insensitive to the NBI heating power, at least between 1 and 5 MW, and tends to decrease radially from ≈ 50 m/s in the near SOL to ≈ 25 m/s in the far SOL; i.e., the turbulent structures appear to decelerate as they move away from the LCFS.

One novel element introduced during the MkiIGB period was the statistical description of SOL transport. In JET, as in other devices, the probability distribution function (PDF) of radial turbulent fluxes showed significant non-Gaussian features, bearing evidence to high levels of intermittency in SOL turbulence¹²² (Fig. 21). It was found that the PDF of radial turbulent fluxes could be rescaled using a finite-size scaling law¹²⁶:

$$\text{PDF}(\Gamma_{\perp}^{ES}) = L^{-1} g(\Gamma_{\perp}^{ES}/L), \quad (54)$$

where Γ_{\perp}^{ES} is the radial turbulent flux, g is an arbitrary function, and L is a scaling factor, which was directly related with the root-mean-square value of j_{sat} fluctuations, i.e., $L \propto \text{RMS}(\tilde{j}_{sat})$. The empirical similarity in turbulent fluxes suggests that edge plasma turbulent transport evolves into a state in which transport PDFs exhibit the same behavior over the entire amplitude range.¹²¹

The effective radial velocities of turbulent structures (blobs, filaments) have also been characterized by statistical methods. In particular, different multiprobe systems have been developed to investigate the links between transport, gradients, and poloidal and parallel flows.^{124,125} The effective radial velocity was of the order of 30 m/s, consistent with earlier measurements (e.g., Ref. 119) and with transport modeling, e.g., using B2-EIRENE and EGDE2D/NIMBUS. The size and velocity of turbulent structures were found to be correlated, such that both increased when the plasma deviated from the average (most probable) gradient. Since most of the time this deviation was small, the ejection of large, fast blobs occurred only sporadically. The effective radial velocity increased up to 500 m/s during these rare but intense plasma bursts. It is worth noting that the magnitude of the turbulent fluxes measured by the probe was generally too high to be consistent with global particle balance. At present, this disagreement still has not been satisfactorily resolved, although the arguments presented earlier concerning poloidal asymmetries (ballooning character) of the turbulence appear to offer the most promising explanation for this discrepancy.

Investigations of the naturally occurring poloidal velocity shear layer (see Fig. 10 in Ref. 8) in the edge region of JET MkiIGB plasmas revealed a link between

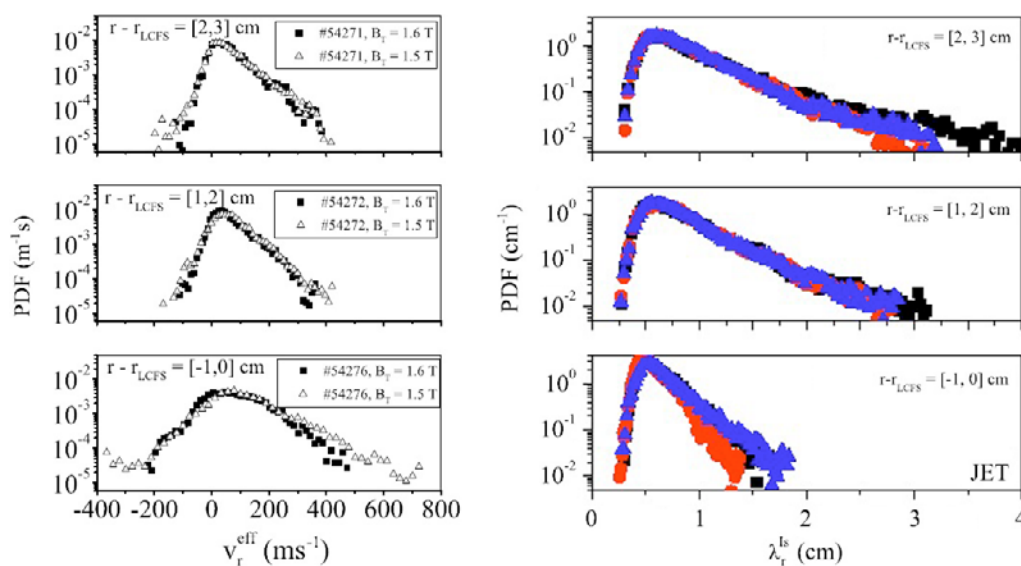


Fig. 21. PDFs of radial effective velocity (left) and radial correlation length of the floating potential (right) as measured by the turbulence probe in the upstream edge/SOL MkiIGB L-mode plasmas. Three radial positions of the probe are shown, corresponding to the far-SOL (top), near-SOL (middle), and edge (bottom) regions, for which $r - r_{\text{LCFS}} = 2$ to 3 cm, 1 to 2 cm, and -1 to 0 cm, respectively. Note the increasing skewness of both PDF profiles with distance away from the LCFS, indicating strongly intermittent transport dominated by sporadic, large bursts. Reproduced with permission from Ref. 123.

fluctuations, parallel flows, and marginal stability.¹²² The $\mathbf{E} \times \mathbf{B}$ shear (zonal) flow in the neighborhood of the LCFS appeared to self-organize so as to maintain the radial gradients in the thermodynamic variables at marginal stability. The influence of sheared flows on the statistical properties of fluctuations has also been studied, showing that PDFs become more Gaussian in the presence of radial gradients in the poloidal $\mathbf{E} \times \mathbf{B}$ velocity.¹²³ It was also established that turbulence can act both as a sink and as a source of energy for the mean (zonal) flow in the shear layer, while measurements of the turbulence production indicated the importance of three-dimensional effects in the energy transfer between flows and turbulence.¹²⁷ Finally, a dynamical coupling between turbulent transport and parallel SOL flows was demonstrated and quantified.^{128,130}

Recently, first attempts at edge/SOL turbulence modeling of JET ohmic and L-mode plasmas were undertaken. The simulations, as described in Ref. 24, made use of an edge-SOL electrostatic (ESEL) code,^{139–141} coupled to first-principles expressions for parallel losses and collisional damping rates.²⁴ Although the radial temperature profiles were well reproduced, the simulated density profiles were somewhat broader than in the experiment.

As usual, the effect of the $L \rightarrow H$ transition on radial SOL fluxes and effective SOL diffusivities in MkiIGB plasmas was investigated using the turbulence probe.¹²⁰ Typical results indicate that radial transport in the near-SOL region was clearly reduced during the H-mode compared to the ohmic phase and that this re-

duction disappeared in the far-SOL region. These results suggest that the H-mode affects SOL (turbulent) transport primarily via the extension of the ETB into the near-SOL region.

The techniques used for the statistical characterization of edge/SOL turbulence in ohmic and L-mode discharges were also applied to ELMy H-mode plasmas to characterize the radial propagation of turbulent blobs and ELM filaments.¹³¹ A similar gradient-velocity relation was detected for both types of structures (Fig. 22). Moreover, ELM filament radial velocities corresponded to those expected of largest turbulent blobs, $v_{\perp} \sim 1$ km/s. This finding was further reinforced by the observed link between the radial velocity and the amplitude (size) of ELM filaments—with less frequent, larger ELMs traveling faster, approximately as $v_{\perp} \propto f_{\text{ELM}}^{-1} \propto \Delta W/W$ (Ref. 129; see Fig. 22).^m In particular, it was concluded that competition between parallel and radial transport was responsible for the observed particle and energy losses to the divertor plates associated with ELMs (Refs. 142 and 144). In spite of the large particle fluxes measured in the far SOL during type-I ELMs, the energy carried by electrons to the main chamber plasma-facing components by the ELM filaments was found to be quite small ($<5\%$ of the ELM energy losses) in the discharges considered.¹²⁹ Indirect measurements of energy loss to the wall associated with ELMs confirmed the hypothesis that larger

^mThis suggests that similar mechanisms are involved in the dynamical evolution of both structures.

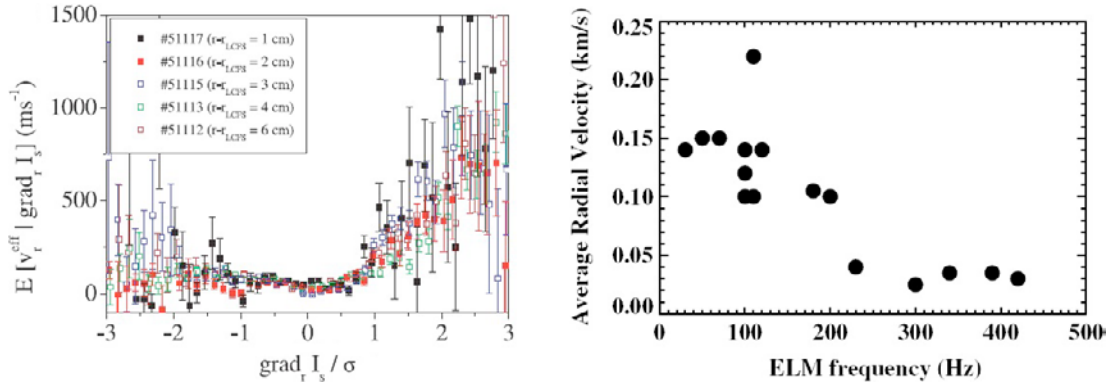


Fig. 22. Expected value of the radial effective velocity for a given saturation current gradient at different radial positions in the SOL of an ELMy H-mode MkiIGB plasma (left) and the average ELM filament velocity as a function of ELM frequency (right). Note that ELM size typically scales inversely with ELM frequency, which means that larger ELMs generally travel faster, approximately as $v_{\perp} \propto f_{\text{ELM}}^{-1} \propto \Delta W/W$. Reproduced with permission from Refs. 129 and 131.

filaments moved faster and indicated fractional loss up to 40% for the largest ELMs (Ref. 143).

The above results were confirmed by time-of-flight measurements of ELM filament velocities using limiter Langmuir probes.¹⁴² The time of arrival of the ELM filament increased linearly with the radial distance of the probe from the separatrix, whereas its width [full-width at half-maximum (FWHM)] increased as the square root of this distance (Fig. 23). Averaged over the SOL, the ELM filament velocities were estimated to be ~ 600 m/s and their radial diffusivities, i.e., the degree of radial broadening, to be ~ 500 m^2/s . The corresponding elec-

tron temperature in the ELM filament at the limiter radius was measured as ~ 25 eV, compared to the pedestal temperature of ~ 1 keV. On the other hand, the ion temperature in the ELM filaments reaching the wall, as measured by a retarding field analyzer probe head mounted on the reciprocating probe head assembly, was found to be substantially larger than the electron temperature, typically $T_i/T_e \sim 2$ to 3 (Ref. 145). All the above data were well reproduced by a parallel loss model, in which the radial propagation velocity of the filament was taken from the experiment and parallel losses of particles and energy were calculated in the filament frame of Ref. 144.

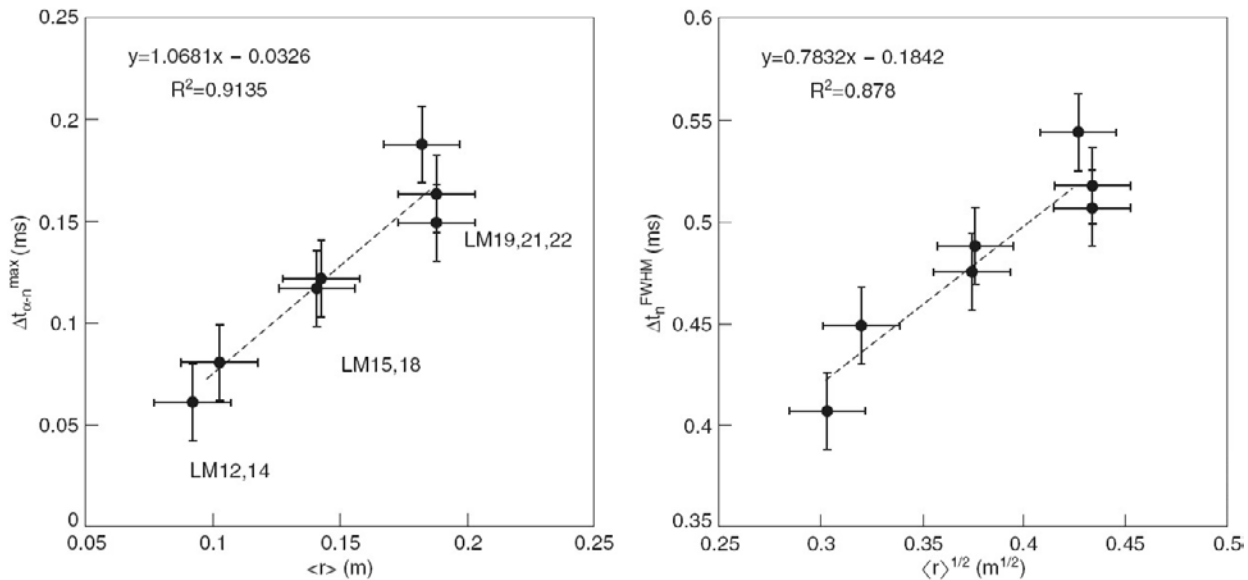


Fig. 23. Average peak time delay, $\Delta t_{\alpha-n}^{\text{max}} = t_n^{\text{max}} - t_{\alpha}^{\text{max}}$, for each probe versus average probe radius $\langle r \rangle$ (left). Average peak current FWHM for each probe versus the square root of the average probe radius (right). Reproduced with permission from Ref. 142.

SOL target profiles of particle flux, electron temperature and hence electron power flux, and the OSM-reconstructed upstream profiles in ELMy H-mode MkIIGB plasmas were found to be similar to those obtained in MkIIA plasmas.^{117,118} The determination of the total power deposited on the divertor required the knowledge of the ion temperature, which cannot be measured with Langmuir probes. Measurement of total, ELM-averaged power using infrared thermography was complicated by the presence of surface layers and spatial resolution of the optical system. In this regard, an important innovation introduced in the MkIIGB period was the development of an additional diagnostic technique capable of measuring the total, ELM-averaged power deposited on the divertor plates.^{146,147} This technique was based on slowly lifting the plasma in rigid body motion over the course of the discharge, such that the strike points traveled over the locations of embedded thermocouples. By reconstructing the thermocouple traces using finite element modeling of the divertor tiles, the average power deposition profile could be extracted. ELM-averaged outer target profiles measured by the three diagnostic techniques (Langmuir probes, infrared thermography, and thermocouples) for a high-power, unfueled (natural density) type-I ELMy H-mode plasma are shown in Fig. 24. Also shown are inner and outer profiles obtained by lifting the plasma (strike point

on a shot-by-shot basis and examining the partition of deposited energy, as measured by thermocouples, between two vertical tiles. All techniques indicate a narrow power deposition profile of less than 5 mm, mapped to the outer midplane, i.e., less than the poloidal ion gyroradius evaluated at the pedestal temperature. The peak total power load on the outer divertor tile increased stronger than linearly with deposited power in unfueled ELMy H-mode plasmas, whereas the electron power (measured by the Langmuir probes) increased weaker than linearly. The excess power, which has been attributed to ELMs and/or energetic ions in the inter-ELM phases of the discharge, increased with heating power or decreased with collisionality. It is noteworthy that the excess power was quite small in the more collisional strongly fueled ELMy H-mode plasmas and/or in helium plasmas, for which the ELMs were also much smaller (type III versus type I) than in deuterium plasmas.

The above techniques formed the basis of a dedicated power exhaust study, including variation in field, current, heating power, density, field ($\mathbf{B} \times \nabla B$) direction, and ion species (D versus He). For a review of these experiments the reader is referred to Refs. 8 and 150. In JET H-mode discharges, the integral width of the total power deposited on the outer divertor target has been found to scale as

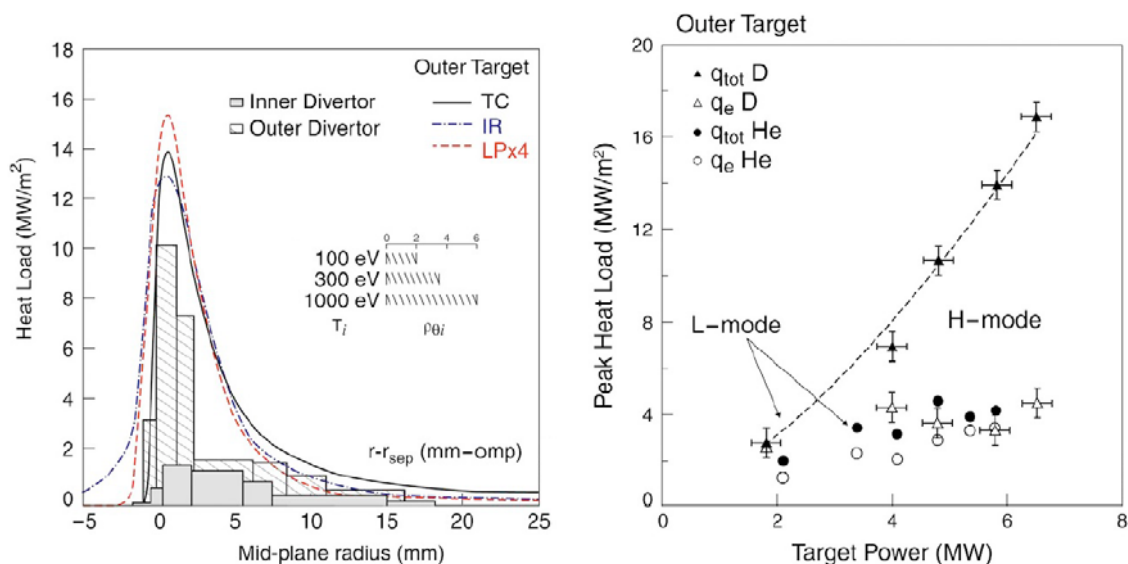


Fig. 24. Comparison of steady-state power deposition profiles measured with thermocouples, infrared thermography, and Langmuir probes at the outer target for an MkIIGB ELMy H-mode plasma (2.5-MA, 2.4-T, 16-MW NBI) (left). The infrared profiles have been averaged over the ELMs. The scale of the electron heat flux (Langmuir probes) is four times smaller in the high-power case. Also shown are the profiles obtained for a 12-MW type-I H-mode (same field and current), using the shot-by-shot thermocouple method. For comparison, the poloidal gyroradius at the outer midplane is shown for three values of the ion energy. The right frame shows the steady-state total (thermocouple) and electron (Langmuir probe) peak heat loads for D and He plasmas as a function of power entering the SOL. The thermocouple values increase faster than linearly with P_T . The excess power becomes more pronounced in D for high-power H-modes. Reproduced with permission from Ref. 8.

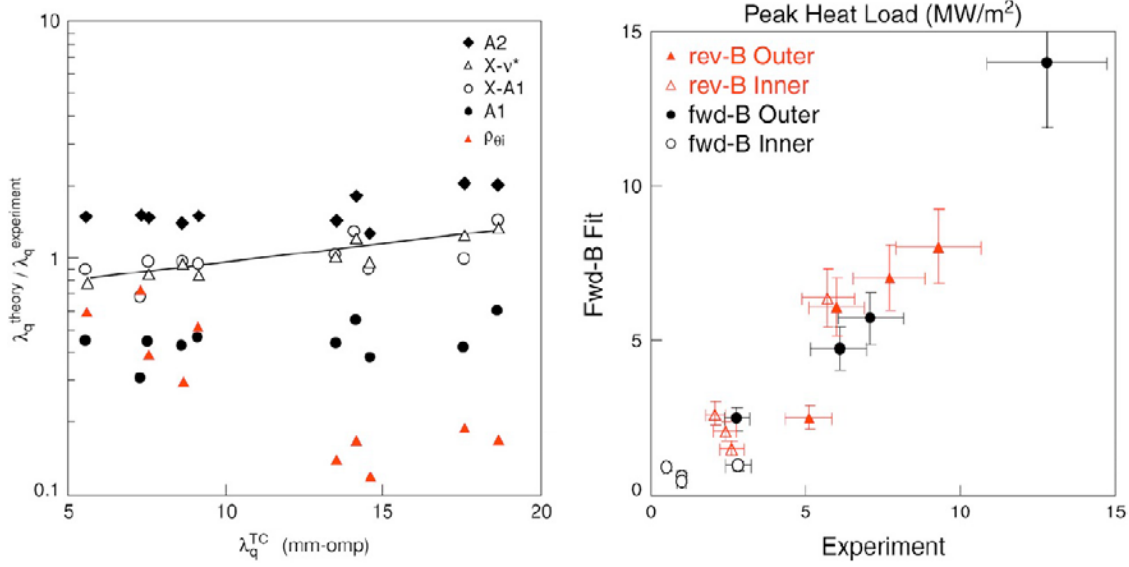


Fig. 25. Ratio of theoretical (neoclassical) and experimental λ_q values for neoclassical and classical ion conduction, A2 and A1, two collisionally modified ion orbit loss estimates, $X - \nu^*$ and $X - A1$, and the poloidal gyroradius, $\rho_{\theta i}$ (left). Comparison of outer target total peak heat loads: best fit to all normal field data versus the experiment, for both field directions and both targets (right). Reproduced with permission from Ref. 8.

$$\lambda_q^{all} \propto A^\alpha Z^\beta B_\phi^{-1.03} q_{95}^{0.6} P_t^{-0.41} n_{eu}^{0.25}, \quad \alpha + \beta = 1.04, \quad (55)$$

if all discharges are included and as

$$\lambda_q^H \propto A^\alpha Z^\beta B_\phi^{-0.93} q_{95}^{0.41} P_t^{-0.48} n_{eu}^{0.15}, \quad \alpha + \beta = 1.11, \quad (56)$$

if only H-mode plasmas are considered.^{8,148,149} To establish the underlying mechanism of (ELM-averaged) SOL energy transport, the measured profile scalings were compared with two dozen theoretical models of radial heat diffusivity in the SOL. The best overall agreement between theory and experiment was obtained with (neo)-classical ion conduction.^{8,148} The appearance of neoclassical diffusion is consistent with the extension of the edge transport barrier into the near-SOL region and the associated reduction in near-SOL turbulence. The comparison between various neoclassical predictions and the measured power widths, shown in Fig. 25, indicate a collisional ion orbit loss as the most likely neoclassical process to explain the observed profile. Collisionless, or direct, ion orbit loss, which was postulated to explain the observations of narrow power profiles in earlier studies (e.g., Ref. 105), was discounted based on the results of a reversed field experiment together with Monte Carlo simulations of ion orbit loss using the ASCOT code.^{149,151–153} Although the code predicted the ion orbit loss profiles to be strongly affected by field reversal, no such effect was observed in the experiment (Fig. 25). The

footprint of direct ion orbit loss on the outer divertor target was calculated based on ASCOT simulations over a wide range of R , B_ϕ , q_{95} , A , and Z (Refs. 8 and 151):

$$\lambda_q^X \propto A^{0.35} Z^{-0.8} B_\phi^{-0.89} q_{95}^{0.88} T_{i,ped}^{0.39} n_{e,ped}^{-0.08} R^{0.8}. \quad (57)$$

This result was used to define two alternative formulations of the collisional ion orbit loss width⁸:

$$\lambda_q^{X-\nu^*} = \lambda_q^X \nu_i^{*1/2}$$

and

$$\lambda_q^{A1-X} = 2.4\zeta \lambda_q^{A1} + (1 - \zeta) \lambda_q^X, \quad (58)$$

where $\zeta = \nu_i^*/(1 + \nu_i^*)$. Both expressions offer excellent fits, within the experimental error of 20%, to the measured power widths (Fig. 25).

IV.E. Effect of Divertor SOL on Plasma Purity, Radiation, and Confinement: MkI to MkIIGB

The effective charge of the core plasma in attached, MkI diverted discharges was found to scale, to a fair approximation, according with⁷⁸

$$Z_{eff} \approx 1 + \frac{7P_{rad}}{A_p(\bar{n}_e)^2}. \quad (59)$$

That is, $Z_{eff} - 1$ increased linearly with the radiative power per unit area P_{rad}/A_p and decreased quadratically with the line average electron density \bar{n}_e . During density

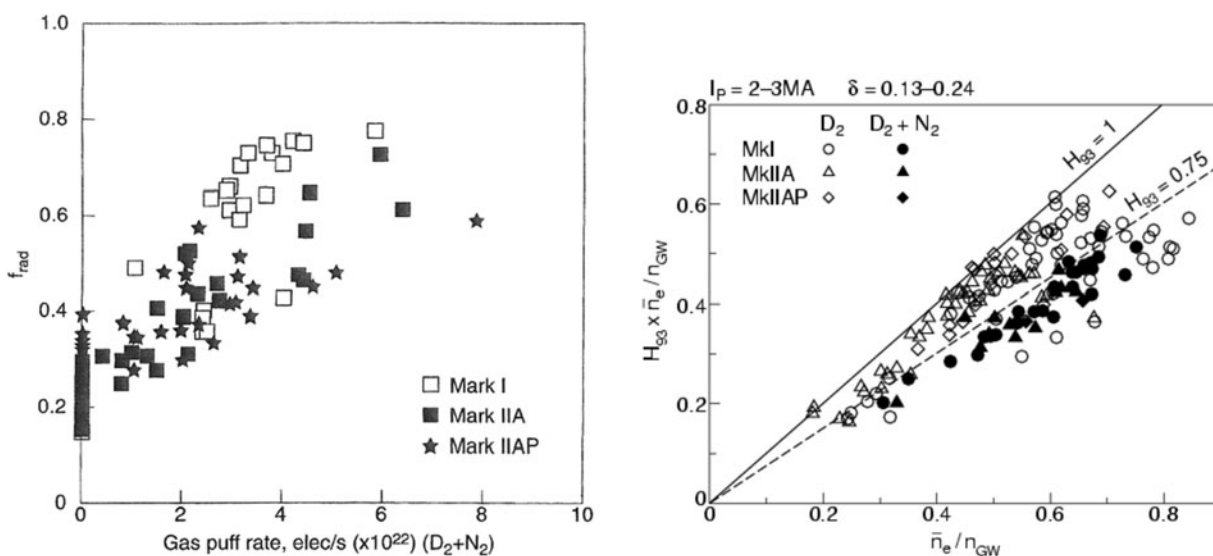


Fig. 26. Variation of the radiative power fraction with the gas puffing rate (left), of the Lawson product $n\tau_E$ normalized by the ITER-93 energy confinement time scaling and the Greenwald density versus the line average density normalized by the Greenwald density (right) in MkI, MkIIA, and MkIIAP ELMy H-modes. Reproduced from Ref. 82.

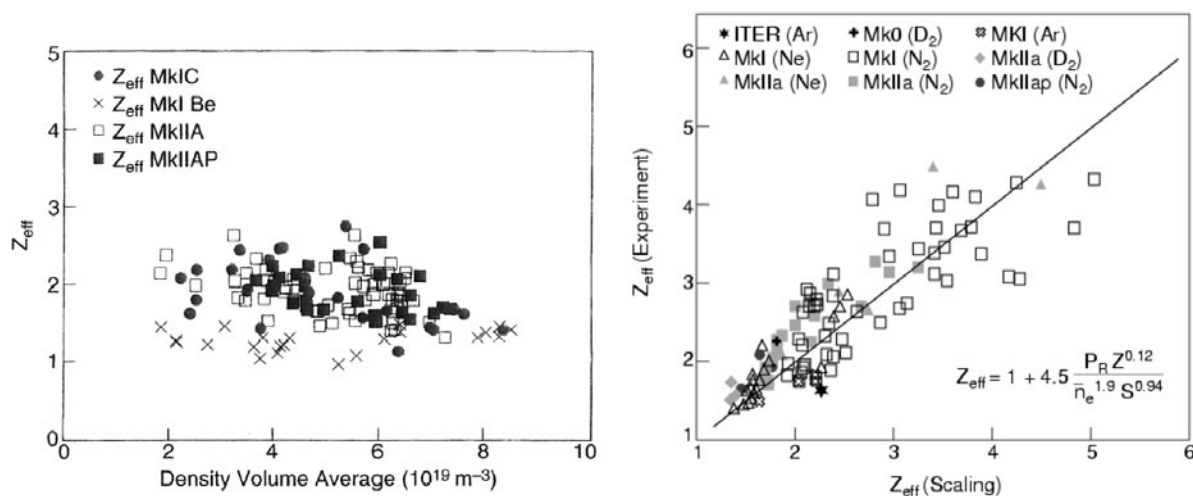


Fig. 27. Variation of Z_{eff} with average density in Mk0, MkI, MkIIA, and MkIIAP ELMy H-modes (left). Comparison of the experimental and best fit expression, which closely resembles Eq. (59), in ELMy H-mode plasmas (right). The best fit expression is shown in the right frame, where P_R represents the radiative power and S the plasma area. Reproduced from Refs. 82 and 83.

scans performed in MkI diverted plasmas (see Sec. IV.B), Z_{eff} followed this attached scaling well into the detached regime, with similar behavior observed in both L-mode and ELMy H-mode plasmas.

The impact of divertor closure (MkIIA versus MkI)¹¹ on plasma purity, radiation, and confinement (normalized

¹¹The results obtained with the MkIIGB divertor were consistent with the MkIIA versus MkI trends.

Lawson product) of the core plasma in ELMy H-mode discharges is shown in Figs. 26 and 27. For a given gas (deuterium) puffing rate, the radiative power fraction was reduced by increasing the divertor closure (MkI \rightarrow MkIIA \rightarrow MkIIAP), without affecting the plasma confinement, which followed the H_{93} scaling up to a Greenwald fraction of 60% (Fig. 26). Similarly, divertor closure had little effect on the confinement properties of nitrogen-seeded plasmas, which generally resulted in

type-III ELMy H-mode, with confinement reduced by ~25% with respect to deuterium-fueled, type-I ELMy H-mode (Fig. 26).

Despite the lower upstream neutral pressure with MkIIA(P) compared to MkI, and consequently smaller charge exchange fluxes onto the main chamber wall, the level of impurities in the core plasma (both intrinsic and extrinsic) was not reduced; i.e., Z_{eff} roughly followed the MkI scaling, Eq. (59), irrespective of divertor closure. This is evident from Fig. 27, which shows Z_{eff} from MkI to MkIIAP together with a best fit scaling.⁸³ The lack of dependence of Z_{eff} on upstream neutral pressure suggests that plasma impact, rather than sputtering by charge-exchange neutrals, was the main cause of impurity influxes from the wall. In particular, similar Z_{eff} values were observed with MkI, MkIIA, and MkIIAP divertors with carbon targets (Z_{eff} in MkI with Be targets was only moderately reduced).

SOL transport of intrinsic impurities, mainly carbon, in MkIIIGB plasmas was studied by injecting known amounts of methane (CD_4) gas at various poloidal and toroidal locations into the torus and calculating the change in the core impurity levels (Z_{eff}) compared to injection of similar amounts of D_2 gas.^{158–160} Partial results for L-mode, inter-ELM H-mode, and ELM-averaged H-mode conditions are shown in Fig. 28, from which it is evident that Z_{eff} was larger in H-mode plasmas, in both the inter-ELM and ELM-averaged sense, consistent with the larger energy input per particle and the L-mode carbon screening dependence [see Eq. (61)].

The L-mode impurity content decreased with density and increased with power as

$$Z_{eff} \propto P_{tot}^{0.2} (\bar{n}_e)^{-0.4} . \tag{60}$$

These results were expressed and explained in terms of the screening parameter S_C , defined as the rate of change of core carbon content divided by the rate of carbon injection; e.g., for outer midplane injection, it was found that S_C increased roughly with the energy per particle ($\sim P_{SOL}/\bar{n}_e$) and with the square root of the SOL connection length, or more accurately,

$$S_C \propto P_{SOL}^{0.85} (\bar{n}_e)^{-1} q_{95}^{0.5} . \tag{61}$$

Under L-mode conditions, S_C was 3 to 20 times smaller in diverted plasmas than in limited plasmas, showing the beneficial effect of distancing the source of impurities away from the LCFS. Similarly, S_C was much smaller, by roughly a factor of 5 or more, for CD_4 injection from the divertor than from the outer midplane. It was also 1.5 to 2 times larger in H-mode, compared to L-mode, plasmas. This variation of the screening parameter was then used to explain the intrinsic carbon levels; e.g., the reduction of Z_{eff} with density was partly due to improvement of carbon screening (lower S_C) and partly due to decreased carbon influxes. In MkIIIGB diverted L-mode plasmas, intrinsic carbon concentration could be explained in terms of low main chamber influxes that were poorly screened and much higher divertor influxes that were well screened, with the net contribution of the two being comparable. Although the same mechanism applied to H-mode plasmas, there the core carbon appeared to originate primarily due to carbon influxes from the divertor, especially due to ELMs.

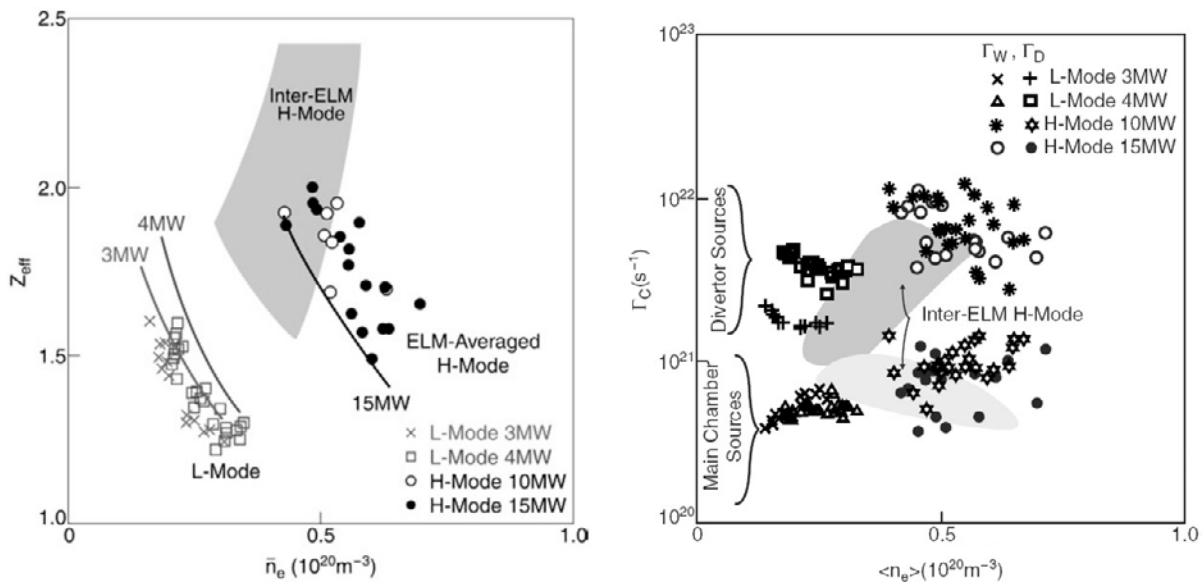


Fig. 28. Core plasma Z_{eff} (left) and intrinsic carbon main chamber and divertor influxes (right) versus line average density in L-mode, inter-ELM H-mode (shaded regions), and ELM-averaged H-mode MkIIIGB plasmas at two levels of NBI heating. Reproduced from Ref. 159.

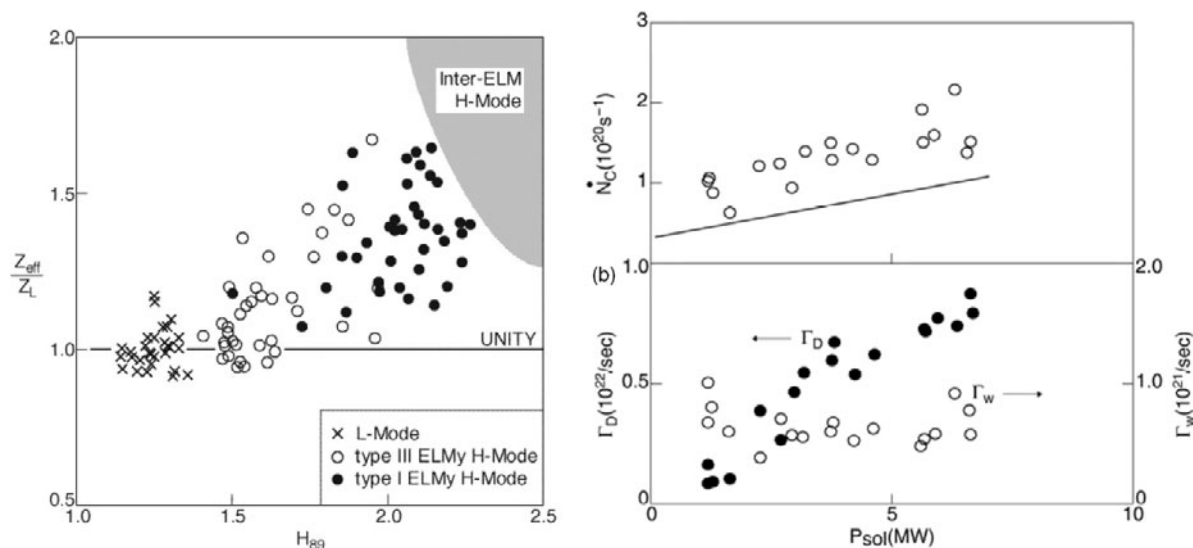


Fig. 29. Ratio of Z_{eff} normalized by the L-mode scaling, Eq. (60), as a function of the energy confinement enhancement factor H_{89} (left), and the rate of change of core carbon content, $\dot{N}_c \equiv dN_c/dt$, and influx of carbon from the divertor Γ_D and the main chamber wall Γ_w as a function of power entering the SOL (right). Reproduced from Ref. 159.

Differences between L-mode and H-mode impurity content are highlighted in Fig. 29. As the confinement increases beyond the L-mode value, so does the core impurity content. Although one detects a positive correlation between these two quantities, the substantial scatter in the data suggests some hidden variable not contained within either scaling. On average, type-I ELMs lead to higher impurity influxes than type-III ELMs, which is likely a consequence of the ELM size (energy per ELM, ΔW_{ped}) and/or the pedestal height (primarily the temperature of the ions, $T_{i,ped}$, expelled by the ELM), both of which are larger for type-I ELMs, thus producing more carbon via physical sputtering (primarily of the divertor targets). However, it is important to note that one could not differentiate between the two types of ELMs on the basis of their Z_{eff}/Z_L versus H_{89} scaling. The shaded region in Fig. 29 reflects the levels of carbon accumulation during the ELM-free period, 0.2 s before the first ELM. During this period, the carbon content increased roughly 4 to 8 times faster than either the deuterium or the energy content; the increase was well correlated with the carbon influx from the divertor, as shown in the right frame of Fig. 29.

The major trends of carbon transport in the SOL were consistent with numerical modeling using both multi-fluid (EDGE2D/NIMBUS) and Monte Carlo (DIVIMP) transport codes, indicating that the experimental results could be explained based on the physical processes contained in these models. In short, modeling indicated that carbon ions were swept toward the divertor whenever the “downstream”-pointing convective forces exceeded the “upstream”-pointing temperature gradient forces. In particular, carbon removal by parallel loss to the divertor

occurred primarily in the far SOL and benefited from cool plasma conditions, allowing more effective collisional coupling between impurity ions and strong hydrogenic parallel flows. For comprehensive reviews of material migration in MkIIIGB plasmas, including the effect of ELMs, the reader is referred to Refs. 156 and 157.

Another important result, first obtained with the MkIIIGB divertor, is the connection between methane puffing into the main SOL and the rise in the far-SOL density profile.¹⁵⁴ In a dedicated study CD_4 was injected near the outer midplane and its effect on the density profile was compared with D_2 injection near the top of the vessel. The results, shown in Fig. 30, show a clear increase of the peripheral density profile, which is directly proportional to the total fluence of injected CD_4 molecules.⁹ Since the ionization mean-free-path for CD_4 is shorter than that for D_2 , it was initially postulated that the excess density is due to local overionization of the SOL flux tubes in the vicinity of the CD_4 with $r - r_{LCFS} \approx 2$ cm, which corresponds to the most probable ionization location. However, EDGE2D/NIMBUS modeling indicated that such overionization had only a small effect on the density profile since parallel losses were also enhanced. To match the observed profiles, it was necessary to increase the radial particle transport in the region

⁹Not surprisingly, the increased far-SOL density had a beneficial effect on lower hybrid power coupling with both D_2 and CD_4 puffing in ELMy H-mode plasmas. This effect was observed provided the gas was injected onto field lines that were magnetically connected with the rectangular area in front of the antenna grill.¹⁵⁵

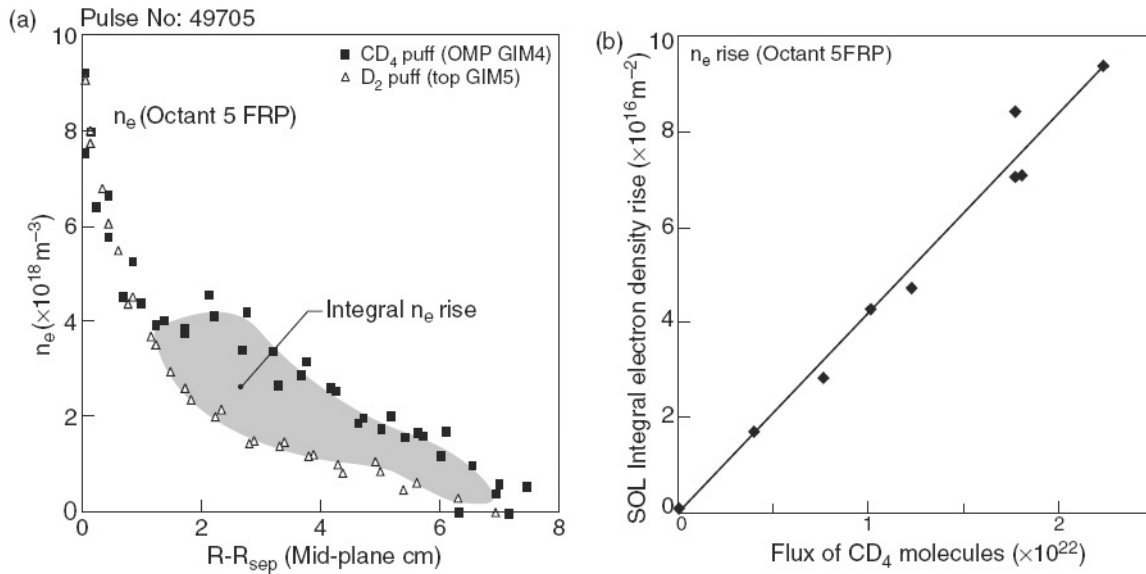


Fig. 30. Upstream density profiles in an MkIIIGB L-mode discharge during a D_2 puff from the top of the torus and CD_4 puff from the outer midplane for the same line average density (left). Peripheral density rise (shaded area in the left plot) versus CD_4 injection fluence (right). Reproduced from Ref. 154.

$r - r_{\text{LCFS}} \approx 1 - 3$ cm. Indeed, such enhancement of the radial $\mathbf{E} \times \mathbf{B}$ fluxes was measured by the turbulence probe. When the inferred diffusivity profile was inserted into EDGE2D/NIMBUS, good agreement was obtained with the measured density profiles. It is significant that the absolute value of the diffusivity had to be reduced by a factor of 5 compared to the peak value of $D_{\perp} \approx 4 \text{ m}^2/\text{s}$ measured with the turbulence probe. Similarly, poloidally uniform diffusivities, $D_{\perp} \approx 0.5$ to $1.5 \text{ m}^2/\text{s}$, combined with EDGE2D/NIMBUS were found to offer a good match to the experimentally measured n_e and T_e profiles shown in Figs. 3 and 9 in Ref. 20. The excess of outer midplane, compared to poloidally averaged, diffusivities is consistent with the known ballooning character of turbulent transport, in which significant radial outflux occurs only in a small poloidal region around the outer midplane. The estimated poloidal extent of this active region ($\Delta\theta \sim 2\pi/5 \sim 70$ deg) is in fair agreement with that measured on Tore Supra⁵⁹ and inferred from JET limiter discharges, Sec. III.A.1.

V. CONCLUSIONS

In this chapter, the progress made in the understanding of boundary plasma, or SOL, physics on JET has been reviewed, focusing mainly on the hydrogenic plasma. The main findings of these investigations are summarized in Table I, which lists selected empirical scalings of LCFS quantities and radial e-folding lengths under various SOL types (limiter versus divertor), target materials

(C versus Be), and confinement regimes (ohmic, L-mode, and H-mode). Broadly speaking, the dominant parameter determining the width of the SOL is the plasma current, which is inversely related to the SOL e-folding length. In addition, a weak density scaling of λ_n is sometimes reported. The limiter and divertor SOLs exhibit similar behavior. Both are dominated by the competition between radial advection of turbulent structures (blobs) and parallel losses. Similar profiles are found in ohmic and L-mode conditions. H-mode profiles are narrower by roughly a factor of 2. There is some, but only moderate, effect of divertor recycling on upstream profiles, e.g., as reflected in the comparison of vertical versus horizontal targets. Similarly, there is a small effect of target material (Be versus C) due to radiation and dilution of the plasma. During H-mode, the ETB is found to extend into the SOL, such that the ELM-averaged profiles appear to be dominated by (neo)classical rather than by turbulent transport. Although the ELM transport in the SOL was not discussed here, it was noted that ELM buffering (radiation of ELM energy) by impurity seeding is not possible.

ACKNOWLEDGMENTS

The author thanks S. K. Erents, G. F. Matthews, R. A. Pitts, A. Loarte, V. Philipps, P. C. Stangeby, and V. Naulin for helpful discussions. The work was funded jointly by the U.K. Engineering and Physical Sciences Research Council and by the European Communities under the contract of association between EURATOM and UKAEA. The view and opinions expressed herein do not necessarily reflect those of the European Commission.

REFERENCES

1. R. D. HAZELTINE and J. D. MEISS, *Plasma Confinement*, Addison-Wesley, New York (1992).
2. M. KEILHACKER et al., *Nucl. Fusion*, **41**, 1925 (2001).
3. A. LOARTE, *Plasma Phys. Control. Fusion*, **43**, R183 (2001).
4. A. LOARTE and P. J. HARBOUR *Nucl. Fusion*, **32**, 681 (1992).
5. P. C. STANGEBY and G. McCracken, *Nucl. Fusion*, **7**, 1225 (1990).
6. C. S. PITCHER and P. C. STANGEBY, *Plasma Phys. Control. Fusion*, **39**, 779 (1997).
7. A. LOARTE, *J. Nucl. Mater.*, **241–243**, 118 (1997).
8. W. FUNDAMENSKI et al., *Nucl. Fusion*, **45**, 950 (2005).
9. L. SPITZER and R. HÄRM, *Phys. Rev.*, **89**, 977 (1953).
10. L. SPITZER, *The Physics of Fully Ionised Gases*, Interscience, New York (1956).
11. S. I. BRAGINSKII, *Rev. Plasma Phys.*, **1**, 205 (1965).
12. W. FUNDAMENSKI, *Plasma Phys. Control. Fusion*, **47**, R163 (2005).
13. P. C. STANGEBY, *The Plasma Boundary of Magnetic Fusion Devices*, IoP Press, Bristol, United Kingdom (2000).
14. G. F. MATTHEWS et al., *Plasma Phys. Control. Fusion*, **36**, 1595 (1994).
15. G. C. VLASES, *Plasma Physics and Controlled Nuclear Fusion Research*, IAEA-CN-56/A-5-1 (1992).
16. A. LOARTE et al., *Nucl. Fusion*, **38**, 331 (1998).
17. A. V. CHANKIN and W. KERNER, *Nucl. Fusion*, **36**, 563 (1996).
18. M. J. SHAFFER et al., *Nucl. Fusion*, **37**, 83 (1997).
19. S. K. ERENTS et al., *Plasma Phys. Control. Fusion*, **42**, 905 (2000).
20. K. ERENTS et al., *Plasma Phys. Control. Fusion*, **46**, 1757 (2004).
21. D. PFIRSCH and A. SCHLÜTER, MPI/PA/7/62, Max-Planck Institute (1962).
22. N. ASAKURA et al., *Nucl. Fusion*, **44**, 503 (2004).
23. B. LaBOMBARD et al., *Nucl. Fusion*, **44**, 1047 (2004).
24. W. FUNDAMENSKI et al., *Nucl. Fusion*, **47**, 417 (2007).
25. W. FUNDAMENSKI et al., *Plasma Phys. Control. Fusion*, **49**, R43 (2007).
26. S. J. ZWEBEN and R. W. GOULD, *Nucl. Fusion*, **25**, 171 (1985).
27. A. J. WOOTTON et al., *Phys. Fluids B*, **2**, 2879 (1990).
28. E. SÁNCHEZ et al., *Phys. Plasmas*, **7**, 1408 (2000).
29. M. ENDLER, *J. Nucl. Mater.*, **266–269**, 84 (1999).
30. J. P. GRAVES, J. HORACEK, R. A. PITTS, and K. I. HOPCRAFT, *Plasma Phys. Control. Fusion*, **47**, L1 (2005).
31. J. A. BOEDO et al., *Phys. Plasmas*, **8**, 4826 (2001).
32. G. ANTAR et al., *Phys. Plasmas*, **10**, 419 (2003).
33. S. J. ZWEBEN et al., *Nucl. Fusion*, **44**, 134 (2004).
34. O. E. GARCIA, V. NAULIN, A. H. NIELSEN, and J. J. RASMUSSEN, *Physica Scripta*, **T122**, 89 (Feb. 2006).
35. J. WESSON, *Tokamaks*, Chap. 9, Oxford University Press, New York (1997).
36. H. ZOHM, *Plasma Phys. Control. Fusion*, **38**, 1213 (1996).
37. J. W. CONNOR, *Plasma Phys. Control. Fusion*, **40**, 191 (1998).
38. J. W. CONNOR, *Plasma Phys. Control. Fusion*, **40**, 531 (1998).
39. J. W. CONNOR and H. R. WILSON, *Plasma Phys. Control. Fusion*, **42**, R1 (2000).
40. W. SUTTROP, *Plasma Phys. Control. Fusion*, **42**, A1 (2000).
41. A. BECOULET et al., *Plasma Phys. Control. Fusion*, **45**, A93 (2003).
42. A. HERRMANN et al., *J. Nucl. Mater.*, **313–316**, 759 (2003).
43. T. EICH et al., *J. Nucl. Mater.*, **337–339**, 669 (2005).
44. M. BECOULET et al., *J. Nucl. Mater.*, **337–339**, 677 (2005).
45. G. T. A. HUYSMANS, *Plasma Phys. Control. Fusion*, **47**, B165 (2005).
46. H. R. WILSON, S. C. COWLEY, A. KIRK, and P. B. SNYDER, *Plasma Phys. Control. Fusion*, **48**, A71 (2006).
47. A. L. LEONARD et al., *Plasma Phys. Control. Fusion*, **48**, A149 (2006).
48. W. FUNDAMENSKI et al., *Plasma Phys. Control. Fusion*, **49**, R43 (2007).
49. ITER PHYSICS BASIS, *Nucl. Fusion*, **39**, 2391 (1999).
50. A. LOARTE et al., *Nucl. Fusion*, **47**, 6, S203 (June 2007).
51. S. K. ERENTS et al., *J. Nucl. Mater.*, **176–177**, 533 (1990).
52. S. K. ERENTS et al., *J. Nucl. Mater.*, **176–177**, 301 (1990).
53. J. A. TAGLE et al., *Proc. 18th EPS Conf. Controlled Fusion*, Berlin, Germany, Vol. 15C, III, p. 149 (1991).
54. J. A. TAGLE et al., *Proc. 14th EPS Conf. Controlled Fusion*, Madrid, Spain, Vol. 11D, II, p. 662 (1987).
55. G. M. McCracken et al., *J. Nucl. Mater.*, **176–177**, 392 (1990).
56. P. H. REBUT et al., in *Fusion Technology*, Vol. I, p. 171, Elsevier, New York (1990).
57. P. J. HARBOUR and A. LOARTE, *Nucl. Fusion*, **35**, 759 (1995).
58. J. A. TAGLE et al., *J. Nucl. Mater.*, **196–198**, 409 (1992).
59. J. GUNN et al., *J. Nucl. Mater.*, **363**, 484 (June 2007).
60. S. K. ERENTS et al., *Nucl. Fusion*, **28**, 1209 (1988).
61. S. K. ERENTS et al., *Nucl. Fusion*, **26**, 1591 (1986).
62. S. K. ERENTS and J. A. TAGLE, TAN(87)2-23, UKAEA (1987).
63. S. K. ERENTS et al., *J. Nucl. Mater.*, **162–164**, 226 (1989).
64. P. C. STANGEBY et al., *Plasma Phys. Control. Fusion*, **30**, 1787 (1988).
65. S. K. ERENTS et al., *J. Nucl. Mater.*, **145–147**, 231 (1987).
66. M. BURES et al., *Plasma Phys. Control. Fusion*, **30**, 149 (1988).
67. S. CLEMENT et al., *J. Nucl. Mater.*, **176–177**, 432 (1990).
68. J. NEUHAUSER et al., *Nucl. Fusion*, **26**, 1679 (1986).
69. P. C. STANGEBY et al., *Plasma Phys. Control. Fusion*, **32**, 475 (1990).
70. I. GARCIA-CORTES et al., *Plasma Phys. Control. Fusion*, **42**, 389 (2000).
71. D. BORBA et al., *Plasma Phys. Control. Fusion*, **48**, 757 (2006).
72. T. TAKIZUKA et al., ITPA H-mode Power Threshold Database Working Group, *Plasma Phys. Control. Fusion*, **46**, A227 (2004).
73. F. WAGNER et al., *Phys. Rev. Lett.*, **49**, 1408 (1982).

74. J. A. TAGLE et al., *Proc. 18th EPS Conf. Controlled Fusion*, Berlin, Germany, Vol. 15C, III, p. 93 (1991).
75. G. C. VLASES, *Plasma Phys. Control. Fusion*, **35**, B6 (1993).
76. C. G. LOWRY et al., *J. Nucl. Mater.*, **241–243**, 438 (1997).
77. G. F. MATTHEWS et al., *Plasma Phys. Control. Fusion*, **37**, A227 (1995).
78. G. F. MATTHEWS et al., *J. Nucl. Mater.*, **241–243**, 450 (1997).
79. J. K. EHRENBERG et al., *J. Nucl. Mater.*, **241–243**, 420 (1997).
80. R. D. MONK et al., *J. Nucl. Mater.*, **241–243**, 396 (1997).
81. R. REICHLER et al., *J. Nucl. Mater.*, **241–243**, 456 (1997).
82. G. C. VLASES et al., *J. Nucl. Mater.*, **266–269**, 160 (1999).
83. G. F. MATTHEWS et al., *Nucl. Fusion*, **39**, 19 (1999).
84. D. J. CAMPBELL, *Plasma Physics and Controlled Nuclear Fusion Research*, IAEA-CN-60/A-4-I-4 (1994).
85. D. J. CAMPBELL et al., *Plasma Phys. Control. Fusion*, **36**, A255 (1994).
86. S. J. DAVIES et al., *Proc. 22nd EPS Conf. Controlled Fusion*, Bournemouth, Vol. III, p. 257 (1995).
87. A. LOARTE et al., *J. Nucl. Mater.*, **220–222**, 606 (1995).
88. A. LOARTE et al., *Proc. 22nd EPS Conf. Controlled Fusion*, Bournemouth, Vol. III, p. 305 (1995).
89. R. D. MONK et al., *Proc. 22nd EPS Conf. Controlled Fusion*, Bournemouth, Vol. III, p. 293 (1995).
90. K. McCORMICK et al., *J. Nucl. Mater.*, **266–269**, 99 (1999).
91. S. K. ERENTS et al., *J. Nucl. Mater.*, **241–243**, 433 (1997).
92. R. D. MONK et al., *J. Nucl. Mater.*, **220–222**, 612 (1995).
93. D. J. CAMPBELL et al., *J. Nucl. Mater.*, **241–243**, 379 (1997).
94. C. F. MAGGI et al., *J. Nucl. Mater.*, **241–243**, 414 (1997).
95. H. Y. GUO et al., *J. Nucl. Mater.*, **241–243**, 385 (1997).
96. M. MAYER et al., *J. Nucl. Mater.*, **241–243**, 469 (1997).
97. K. GUENTHER et al., *J. Nucl. Mater.*, **241–243**, 462 (1997).
98. J. P. COAD et al., *J. Nucl. Mater.*, **241–243**, 408 (1997).
99. S. J. DAVIES et al., *J. Nucl. Mater.*, **220–222**, 426 (1995).
100. G. K. McCORMICK et al., *J. Nucl. Mater.*, **241–243**, 444 (1997).
101. D. J. CAMPBELL et al., *Plasma Phys. Control. Fusion*, **38**, 1497 (1996).
102. G. SAIBENE et al., *J. Nucl. Mater.*, **241–243**, 476 (1997).
103. J. LINGERTAT et al., *J. Nucl. Mater.*, **241–243**, 402 (1997).
104. J. LINGERTAT et al., *J. Nucl. Mater.*, **220–222**, 198 (1995).
105. J. LINGERTAT, M. LAUX, and R. MONK, *J. Nucl. Mater.*, **290–293**, 896 (2001).
106. I. S. LANDMAN and H. WUERZ, *J. Nucl. Mater.*, **290–293**, 1088 (2001).
107. G. M. McCracken et al., *J. Nucl. Mater.*, **266–269**, 37 (1999).
108. H. GUO et al., *Nucl. Fusion*, **40**, 379 (2000).
109. M. L. WATKINS et al., *Proc. 21st Int. Conf. Fusion Energy*, Chengdu, China, 2006, IAEA (2006).
110. M. GREENWALD et al., *Nucl. Fusion*, **28**, 2199 (1988).
111. S. K. ERENTS et al., *Nucl. Fusion*, **38**, 1637 (1998).
112. S. J. DAVIES et al., JET-P(97)39, JET preprint (1997).
113. S. J. DAVIES et al., *J. Nucl. Mater.*, **266–269**, 1028 (1999).
114. W. FUNDAMENSKI et al., *J. Nucl. Mater.*, **290–293**, 593 (2001).
115. W. FUNDAMENSKI, “Tokamak Edge Plasma Modelling Using an Improved Onion-Skin Method,” PhD Thesis, University of Toronto, Institute of Aerospace Studies (1999).
116. W. FUNDAMENSKI, P. C. STANGEBY, and J. D. ELDER, *J. Nucl. Mater.*, **266–269**, 1054 (1999).
117. S. K. ERENTS et al., *Nucl. Fusion*, **40**, 295 (2000).
118. S. K. ERENTS et al., *Nucl. Fusion*, **40**, 309 (2000).
119. I. GARCIA-CORTES et al., *Plasma Phys. Control. Fusion*, **38**, 2051 (1996).
120. I. GARCIA-CORTES et al., *J. Nucl. Mater.*, **290–293**, 604 (2001).
121. M. A. PEDROSA et al., *Phys. Rev. Lett.*, **82**, 003621 (1999).
122. C. HIDALGO et al., *J. Nucl. Mater.*, **337–339**, 863 (2005).
123. B. GONÇALVES et al., *J. Nucl. Mater.*, **337–339**, 376 (2005).
124. B. GONÇALVES et al., *Rev. Sci. Instrum.*, **74**, 1571 (2003).
125. C. SILVA et al., *Rev. Sci. Instrum.*, **75**, 4314 (2004).
126. C. HIDALGO et al., *Plasma Phys. Control. Fusion*, **44**, 1557 (2002).
127. B. GONÇALVES et al., *Phys. Rev. Lett.*, **96**, 145001 (2006).
128. E. SÁNCHEZ et al., *J. Nucl. Mater.*, **337–339**, 296 (2005).
129. C. SILVA et al., *J. Nucl. Mater.*, **337–339**, 722 (2005).
130. C. HIDALGO et al., *Phys. Rev. Lett.*, **91**, 065001 (2003).
131. B. GONÇALVES et al., *Plasma Phys. Control. Fusion*, **45**, 1627 (2003).
132. C. HIDALGO et al., *J. Nucl. Mater.*, **313–316**, 863 (2003).
133. B. GONÇALVES et al., *Plasma Phys. Control. Fusion*, **42**, 1205 (2002).
134. B. GONÇALVES et al., *Proc. 32nd EPS Conf. Plasma Physics*, Tarragona, Spain, Vol. 29C, P-4.038 (2005).
135. B. GONÇALVES et al., *Proc. 30th EPS Conf. Plasma Physics*, St. Petersburg, Russia, Vol. 27A, P-2.157 (2003).
136. C. HIDALGO et al., *Proc. 30th EPS Conf. Plasma Physics*, St. Petersburg, Russia, Vol. 27A, P-3.200 (2003).
137. C. HIDALGO et al., *Proc. 29th EPS Conf. Plasma Physics*, Montreaux, France, Vol. 26B, O-2.05 (2002).
138. C. HIDALGO et al., *Proc. 29th EPS Conf. Plasma Physics*, Funchal, Portugal, Vol. 25A, 1657 (2001).
139. O. E. GARCIA et al., *Plasma Phys. Control. Fusion*, **48**, L1 (2006).
140. O. E. GARCIA, V. NAULIN, A. H. NIELSEN, and J. J. RASMUSSEN, *Phys. Rev. Lett.*, **92**, 165003 (2004).
141. O. E. GARCIA, V. NAULIN, A. H. NIELSEN, and J. J. RASMUSSEN, *Phys. Plasmas*, **12**, 062309 (2005).
142. W. FUNDAMENSKI et al., *Plasma Phys. Control. Fusion*, **46**, 233 (2004).
143. A. LOARTE et al., *Phys. Plasmas*, **11**, 2668 (2004).
144. W. FUNDAMENSKI et al., *Plasma Phys. Control. Fusion*, **48**, 109 (2006).
145. R. A. PITTS et al., *Nucl. Fusion*, **46**, 82 (2006).
146. W. FUNDAMENSKI et al., *Plasma Phys. Control. Fusion*, **44**, 761 (2002).

147. V. RICCARDO et al., *Plasma Phys. Control. Fusion*, **43**, 881 (2001).
148. W. FUNDAMENSKI et al., *Nucl. Fusion*, **44**, 20 (2004).
149. W. FUNDAMENSKI et al., *J. Nucl. Mater.*, **337–339**, 305 (2005).
150. G. F. MATTHEWS et al., *Nucl. Fusion*, **43**, 999 (2003).
151. S. SIPILÄ et al., *Proc. 32nd EPS Conf. Plasma Physics*, Tarra-gona, Spain, Vol. 29C, P-2.111 (2005).
152. S. SIPILÄ et al., *Proc. 29th EPS Conf. Plasma Physics*, Mon-treux, France, Vol. 26B, P-3.210 (2002).
153. S. SIPILÄ et al., *Proc. 29th EPS Conf. Plasma Physics*, Funchal, Portugal, Vol. 25A, 665 (2001).
154. G. F. MATTHEWS et al., *Plasma Phys. Control. Fusion*, **44**, 689 (2002).
155. A. EKEDAHL et al., *Nucl. Fusion*, **45**, 351 (2005).
156. R. A. PITTS et al., *Plasma Phys. Control. Fusion*, **47**, B303 (2005).
157. G. F. MATTHEWS et al., *J. Nucl. Mater.*, **337–339**, 1 (2005).
158. J. D. STRACHAN et al., *J. Nucl. Mater.*, **337–339**, 25 (2005).
159. J. D. STRACHAN et al., *Nucl. Fusion*, **43**, 922 (2003).
160. J. D. STRACHAN et al., *J. Nucl. Mater.*, **290–293**, 972 (2001).